School of Mathematics, Computer Science and Engineering

Electrical and Electronic Engineering

Modelling and Design of High-Speed, Long-Lifetime and Large-Force Electromagnetic Actuators Based on Magnetic Shape Memory Alloys

Gabdullin Nikita

Thesis is submitted for the fulfilment of the
requirements for the degree of Doctor of Philosophy of the
City, University of London

December 2016

List of Papers

1. Gabdullin N.A., Khan S. H, "Application of change in permeability of magnetic shape memory (MSM) alloys for optimization of magnetic circuit in actuators," *Proc. CEM, 9th IET int. Conf.*, pp. 1-2, 2014.
2. N Gabdullin and S H Khan "Review of properties of magnetic shape memory (MSM) alloys and MSM actuator designs," *J. Phys. Conf. Ser.*, vol. 588, p. 012052, 2015.
3. Gabdullin N.A., Khan S. H, "Effects of Varying Permeability of Magnetic Shape Memory (MSM) Alloys on Design and Performance of Actuators," *Proc. COMPUMAG*, 2015.
4. N. Gabdullin, S. H. Khan, "Electromagnetic and Thermal Analysis of High Performance Magnetic Shape Memory Actuators for Valve Application," *IEEE Trans. Magn.*, vol. 52, no. 9, pp. 8205306, 2016.
5. N Gabdullin and S H Khan "Study of magnetic field distribution in an anisotropic single twin boundary magnetic shape memory element in actuators," *J. Phys. Conf. Ser.* (in press), 2016.
6. N. Gabdullin, S. H. Khan, "Simulation-based Design Methodology for Magnetic Shape Memory Actuators," *Proc. ICFSMA 2016*, pp. 165-166, 2016.
7. N. Gabdullin, S. H. Khan, "Study of Non-Homogeneity of Magnetic Field Distribution in Single-Crystal Ni-Mn-Ga Magnetic Shape Memory Element in Actuators due to its Anisotropic Twinned Microstructure," *IEEE Trans. Magn. (in press)*, 2017.

Table of Contents

List of Figures

List of Tables

Abstract

The main topic of this research is modelling and design of high-speed, large-force and long life-time electromagnetic actuators based on Magnetic Shape Memory (MSM) alloys. These relatively new “smart” alloys that change shape in magnetic fields possess very promising properties such as large strain, considerable output stress and potentially very long fatigue life. However, there is still lack of a consistent design methodology for MSM-based devices which can be implemented using techniques common for engineering design. In order to bridge this gap, a modelling approach for MSM element in actuators is developed in which the complete magnetic circuit of MSM actuator is included into a single finite element (FE) model. This approach also allows accurate representation of MSM permeability change during the shape change capturing its effects on total reluctance of the magnetic circuit. Moreover, this approach allows studying the magnetic field distribution in the MSM element in single, two and multi-variant states in magnetic fields of varying strength. The modelling results show striking non-homogeneity of the magnetic field distribution, providing new insights on the magneto-mechanical behaviour of the MSM element. The modelling approach is verified through comparing the calculated MSM permeability change with previously reported results obtained by measurement.

Using this modelling approach, electromagnetic analysis is conducted for eleven MSM actuators. The actuators are designed and optimised for a particular 0.1mm strain (displacement) and 10N force output for implementation in food-sorting machines. The conducted analysis also ensures robustness of the designs and stable multi-billion cycle operation. The very long lifetime is achieved through careful analysis of the magnetic circuit and the behaviour of the MSM element during operation.

Finally, thermal analysis is conducted for the designed actuators in order to ensure their thermal stability. In order to overcome challenges associated with a very low operating temperature limit of the MSM element in actuators, different available cooling conditions are studied. Moreover, an energy-efficient operation cycle is developed that takes advantage of the shape memory effect of the MSM element also taking into account the pressure change in the pneumatic valve of a sorting machine. The analysis shows multiple regimes which allow thermal stability in a 300Hz pulsed excitation cycle. Implementation of the developed operating cycle also leads to the considerable increase in overall efficiency.

List of Abbreviations

2D – two dimensional
3D – three dimensional
5M – five layer-modulated microstructure
7M – seven layer-modulated microstructure
NM – non-modulated microstructure
CAD – computer-aided design
EM - electromagnetic
MFI – magnetic field-induced
mmf – magnetomotive force
MSM – magnetic shape memory
MSMA – magnetic shape memory alloy
MVP – magnetic vector potential
MSP – magnetic scalar potential
SMA – shape memory alloys (thermally activated)
HTSMA – high temperature shape memory alloys
TB – twin boundary
FE – finite element
FEA – finite element analysis
FEM – finite element method
L-U – Likhachev and Ullakko

Glossary of special terms

"Easy" axis – high permeability/magnetisation axis of a crystal
"Hard" axis – low permeability/magnetisation axis of a crystal
Twin variant – a region of MSM element with the same orientation of crystallographic axes in the lattice
Twin boundary – a boundary separating different twin variants
Band (modelling) – area of a model with predefined geometry used for representing MSM twin variants
Twinning stress – stress required for propagating an existing twin boundary
Nucleation twinning stress – stress required for nucleating a twin boundary

Type I (or II) twin boundary – characteristic of twin boundaries related to its geometry and mobility

Twin I (or II) crystal – a crystal with boundaries of either type I or type II

Variant reorientation – a process related to the growth of one twin variant at expense of another one accompanied by twin boundary motion and overall shape change

Switching field – minimum magnetic field required to initiate variant reorientation

Symbols used in equations

Symbol	Meaning	Unit
B	Magnetic flux density	T
H	Magnetic field intensity	A/m
M	Magnetisation	T
μ_0	Free air permeability	H/m
μ_r	Relative permeability	-
μ	Absolute permeability	H/m
E	Electric field intensity	V/m
J	Current density	A/m^2
D	Electric flux density	C/m^2
ε_0	Free air permittivity	F/m
ε_r	Relative permittivity	-
ρ	Electric charge density	C/m^3
σ	Electric conductivity	$(ohm \cdot m)^{-1}$
A[1]	Magnetic vector potential	Wb/m
ψ	Magnetic scalar potential	A
φ	Electric scalar potential	V
F	mmf	A
Φ	Magnetic flux	Wb

[1]Several parameters may share the same abbreviation

Symbol	Meaning	Unit
R	Reluctance	H^{-1}
L	Inductance	H
U	Voltage	V
I	Electric current	A
R	Resistance	ohm
ρ	Resistivity	ohm·m
P	Power	W
f	Frequency	Hz
δ	Depth of penetration	m
r	Radius-vector	m
η	Efficiency	-
tanδ	Loss tangent	-
F	Force	N
u	Displacement	m
K	Stiffness	N/m
C	Damping	N·s/m
M	Mass	kg
σ	Stress	MPa
T	Temperature	K
q	heat flux	W/m^2
k_c	Thermal conductivity	W/m·K
k_f	Convective film coefficient	$W/m·K^2$
k_{cf}	Coil filling factor	-
N_c	Number of coil turns	-
N_{el}	Number of elements in a FE model	-
a	Width	m
b / h	Height	m
l	Length	m
d	Diameter	m
A	Area	m^2

Symbol	Meaning	Unit
δ	Air gap width	m
t	Time	s
K_u	Lattice anisotropy constant	J/m^3
ε_0	Lattice distortion constant	-
σ_{tw}	Twinning stress	MPa
ε	Current strain of MSM element	%

Chapter 1. Introduction

1.1 Motivation for this study

The current state of technological progress demands all electrical equipment to be efficient, reliable and robust. Electromagnetic actuators are used in a very wide range of applications, from small low/high frequency devices for low force output such as optical mirrors and magnetic printing systems to huge valves and large force actuators such as motors, relays and valves. Electromagnetic solenoid actuators have proved themselves very effective in these applications. Nowadays, this area is very well studied and inherent limitations of the technology are known which cannot be overcome by further research. Therefore, a new technological solution should be found that can fit this diverse area of applications increasing reliability, power savings and lifetime. A very prospective candidate for this role is Magnetic Shape Memory (MSM) technology which is based on the use of MSM alloys. These alloys provide enormous field-controlled strain and considerable output force also possessing very long fatigue life. Moreover, common challenges related to mechanical fatigue life of moving parts in solenoid actuators can be overcome since the motion is a result not of actual movement but of shape change of one element. However, conventional MSM alloys are rather expensive, making MSM actuators economically uncompetitive. This research aims to develop a comprehensive methodology for design and optimisation of MSM actuators in order to show prospective advantages of their application, which is also greatly beneficial for this research area. This will be done for large-force long life-time MSM actuators, which also are fast and robust. Along with decreased manufacturing costs, it will allow bringing the prices to an acceptable level, opening a huge market for MSM actuators.

MSM alloys are still mainly at a research and development stage, which makes this task simultaneously very challenging and interesting. Properties of MSM alloys have been improved significantly even during the last 5 years, and we expect more fascinating results from material researchers in upcoming years. It should be mentioned that actuator design and performance is intertwined with properties of its MSM element. For

that reason it is very important to identify properties which have the most influence on the overall performance of an actuator.

Nowadays, the most part of the research conducted in the scientific society is concentrated on the material itself and not MSM devices and their applications. Models describing MSM behaviour proposed up to this day are mostly inapplicable to MSM actuator design and performance evaluation. To overcome their limitations, finite element (FE) modelling is chosen as the main tool for designing actuators' magnetic circuits. This allows not only to include the complete magnetic circuit into a single model, but also to see the actual field distribution taking saturation into account simultaneously analysing the behaviour of the MSM element. Data obtained from such a solution also allows optimising the magnetic circuit on a modelling step. This approach is much more accurate when materials which are not well studied are dealt with. Moreover, FE modelling is proved to be a very good technique for analysis of electromagnetic devices where equations that describe underlying physics cannot be solved analytically.

The area of application considered in this research regards MSM valves for food sorting machines. These machines distinguish optical properties of the food which is moved at very high speed, products like rice, coffee, beans, etc. The non-contact sensor technology used to identify unwanted product items is based on optical techniques such as light transmittance, surface reflectance, and optical absorption. Most sorting machines of this type rely mainly on colour differences between 'accept' and 'reject' products and other physical properties that are detectable optically (e.g. shape, colour). Depending on the food products and the nature of contaminants they contain, monochromatic, bichromatic and trichromatic optical sub-systems are often used for simultaneous colour and shape discrimination. These are combined with high-sensitive linear detector arrays to obtain high-speed and high-resolution bulk sorting. The ejector valve actuator reacts to the control stimuli activating the pneumatic sub-system which separates the unwanted units from the rest of the product.

Figure 1.1-1 shows the schematic diagram of an optical sorting machine showing the optical and ejector sub-system.

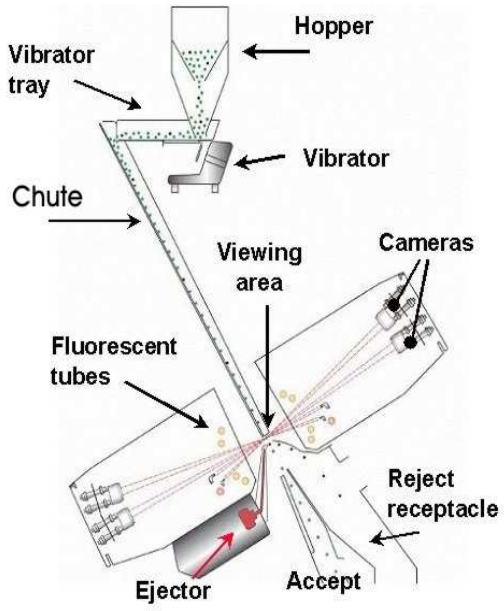

Figure 1.1-1. Schematic diagram of an optical sorting machine

The MSM valve actuator essentially works in on/off regime and has a rather simple construction consisting of a coil wound around a magnetic core which conducts flux to MSM element capable of both elongation and contraction. Such application requires valves to provide a considerable output force of about 10N, being also fast and reliable to guarantee high quality of food sorting. The required actuator output displacement for activating the pneumatic valve is 0.1mm, which is relatively low. Typically, an individual actuator fits into an array of 32, 64, 96 or 128 ejectors. This results in an additional constraint on width of individual actuator which is desired to be as small as possible. In order to address this, this work aims to design actuators which magnetic circuit width does not exceed 10mm. This additional parameter constraint has significant effects on actuator designs discussed in Chapter 5.

1.2 Aim and Objectives

The reasoning above sets academic and industrial context and determines steps to be undertaken to design devices and investigate properties of MSM actuators using mathematical modelling. Objectives of this study are as follows.

(a) To analyse the work done so far in field of material study in order to identify which properties of MSM alloys are the most important for actuators' performance, what they depend on and how their variations can affect the overall output of the device.

(b) To develop a methodology for design and modelling of MSM actuators. On the first step, magnetic circuit of an actuator which includes the MSM element is to be considered. The whole magnetic circuit will be included in a single 3D FE model. Approaches that allow taking varying MSM properties into account will also be developed. The magnetic problem solution will be used for evaluating the overall displacement and force output of a complete actuator.

(c) Electromagnetic transient analysis will also be conducted in order to study the time-dependent processes inside the device. This also will help to determine the most effective energy source and appropriate control parameters for efficient, fast and reliable actuator operating.

(d) Thermal analysis of the designed actuators will be conducted in order to ensure their thermal stability. Properties of existing MSM alloys are known to be very sensitive to temperature change which poses an additional design challenge when coupled with considerable power loss accompanying actuator operating.

Fulfilling objectives (a)-(d) will result in achieving the main aim of this project

To design robust, large-force, long life-time MSM actuators which satisfy current requirements of 0.1mm strain, 10N output force and fatigue life of more than 6 billion cycles at a 300Hz frequency. The designed actuators will also be very compact meeting the 10mm constraint on size typical for food sorting applications.

1.3 Plan of the Thesis

In addition to this Introductory Chapter, this Thesis consists of two overview Chapters, three Chapters presenting the main outcomes of this work and the Conclusions Chapter. Chapter 2 provides an overview of MSM alloys and their properties, and discusses different aspects of their magneto-mechanical behaviour. It also includes a particularly important Section that discusses fatigue behaviour of different MSM crystals, which is followed by the overview of potential applications of MSM alloys in electromagnetic devices. Chapter 3 includes mathematical formulation of the electromagnetic and thermal analyses associated with the MSM actuator design also providing an overview of the FE method with its application to the abovementioned analyses. Chapter 4 discusses FE modelling of MSM actuator magnetic circuit with a particular emphasis on the development of an accurate MSM element modelling approach. It also includes a study on the magnetic field distribution in the MSM element followed by a discussion of its permeability change during the shape change and its effects on the actuator performance evaluation. Chapter 5 discusses the designs of compact large-force MSM actuators including their optimisation on basis of electromagnetic analysis. This leads to eleven final designs for which various output characteristics are calculated. Chapter 5 also introduces an energy-efficient operating cycle that takes advantage of the holding force associated with the MSM element. Chapter 6 summarises the results of the thermal analysis conducted for the designed actuators studying the effects of different cooling conditions and operating regimes using the cycle designed in the previous Chapter. Finally, Chapter 7 concludes the work showing that the aim and objectives discussed in Section 1.2 have been successfully achieved and discusses possible routes for further development.

Chapter 2. Magnetic Shape Memory alloys

2.1 Introduction to MSM alloys and their properties

Magnetic shape memory (MSM) or ferromagnetic shape memory (FSMA) "smart" alloys form a new class of shape memory materials which respond to magnetic fields [1]. MSM alloys can also be controlled mechanically, and both magnetically and mechanically induced stresses are coupled [2]. Ni-Mn-Ga alloys are the most studied MSM alloys which exhibit enormous 6-12% magnetic field induced strain (change in shape) depending on specimen microstructure [3], [4]. Moreover, the theoretical strain limit goes up to 20% for MSM crystals with non-modulated microstructure [5], which is yet to be observed experimentally [6]. These greatly exceed strains produced by piezoelectric and giant magnetosrictive materials (GMM) and are of the same order as strains produced by conventional shape memory alloys (SMA) activated by heat. However, MSM alloys' shape change does not necessarily involve phase transformation, which is essential for long fatigue life of MSM crystals and allows designing long lifetime actuators [7]. MSM alloys are also very promising for use in sensors and other electrical devices in a frequency range up to several kHz. MSM actuators are high-performance, fast, compact, energy efficient and reliable. Nowadays, the most important drawbacks of MSM crystals are low martensite-austenite transformation temperature which determines their upper operating temperature limit, and a considerable magneto-mechanical hysteresis. However, properties of MSM alloys keep constantly improving.

MSM elements used in actuators are commonly produced as single-crystals which have tetragonal lattice in low-temperature martensite phase. The shape change in magnetic fields occurs due to inequality in lattice parameters coupled with magnetic anisotropy of the crystal [8]. A short crystallographic *c* axis which is also "easy" magnetisation axis tends to align with the applied magnetic field. This can lead to local reorientation of the crystal [9]. Since "hard" magnetisation *a* and *b* axes are longer than *c* axis, local reorientation of the crystal results in overall elongation or contraction of the MSM element. Therefore, these crystals possess a "hard" plane and an "easy" axis of magnetisation. However, only the behaviour of *a*-*c* plane is commonly of interest since

reorientation happens in this plane. The maximum change in shape (strain) is related to the ratio of crystallographic parameters as ε_{max}=1-*c*/*a*. However, the overall change in shape is a consequence of local effects. MSM microstructure is formed by multiple areas with different orientation of crystallographic *c* axes called twin variants in any intermediate state when not fully contracted or elongated (see Fig. 2.1-1). Variants which have their "easy" axes aligned with the applied magnetic field are commonly referred to as "easy" variants, whereas "easy" axes are transverse to the bias field in "hard" variants. As intensity of the applied magnetic field increases, "easy" variants grow at expense of "hard" variants until a single variant of one type is present [3]. The magnetic field is usually applied transverse to the longest side of a tetragonal MSM element in order to produce output strain in MSM actuators (see Fig. 2.1-1 (a)). Output strain and stress production is possible as long as "hard" variants exist. However, a magnetic field applied along the length of the element results in its contraction, as shown in Fig. 2.1-1 (b). This phenomenon is a direct consequence of the magnetic anisotropy of MSM twin variants since variants favoured by transversely applied magnetic field are not favourable for longitudinal fields. It should be noted that only the abovementioned macroscopic "hard" and "easy" twin variants are considered in this study. Further characterisation of MSM microstructure up to nano-scale level was a subject of numerous studies e.g. [10]–[13]. However, only macro-twin behaviour is needed to be taken into account when designing electromagnetic actuators.

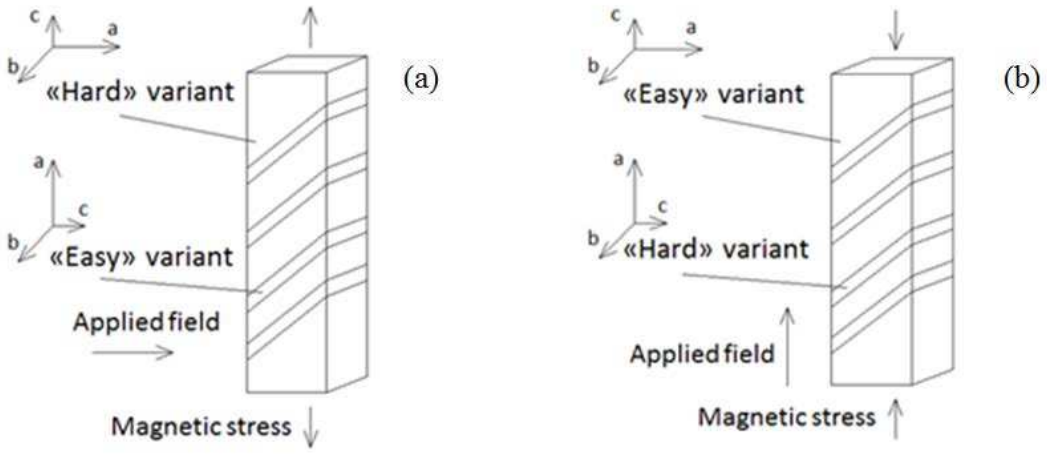

Figure 2.1-1**.** Orientation of crystallographic axes in twin variants of MSM element, (a) transversally and (b) longitudinally applied magnetic fields

MSM behaviour is known to occur only in a few alloys which composition should be carefully monitored. These alloys experience austenite-martensite phase transformation during cooling in manufacturing process. Because the transformation is diffusionless, large stresses have to be accommodated in the martensite phase. In order to minimise this energy, the microstructure organises itself into a number of crystallographic domains called variants, which are separated by twin boundaries [14]. Lattice of MSM alloy gets distorted leading to a different magnetic orientation of different parts of the whole volume of the alloy.

The *c/a* ratio is one of the most important parameters of the MSM alloys since lattice distortion ε_0 determines maximum possible strain. It varies even for Ni-Mn-Ga alloys with different microstructures. For instance, the most studied five-layered modulated (5M) Ni-Mn-Ga alloys have $c/a = 0.94$ leading to 6% maximum theoretical strain [3]. This result has been verified many times by different researchers e.g. [15], [16]. In alloys with seven-layered modulated (7M) microstructure $c<a$ and $c/a=0.9$, while in those with non-modulated (NM or T) microstructure $c>a$ and $c/a=1.2$ [5]. The ability of a twin boundary to move under external force is characterised by twinning stress. For instance, only 12% of theoretical 20% strain has been observed in NM crystals due to very high twinning stress [4]. Only alloys with 5M microstructure have been proposed for application in actuators and sensors due to the lowest twinning stress and high mobility of twin boundaries. Nowadays, alloys with less than 0.1 MPa twinning stress can be manufactured which are very efficient and have very narrow hysteresis loop [17], [18]. Such alloys may seem the best possible choice for EM devices.

Ferromagnetic materials change their shape in magnetic fields due to magnetostriction. Therefore, it seems important to be able to distinguish MSM variant reorientation strain from magnetostriction. However, it has been shown that magnetostriction plays negligible role in straining of MSM alloys and, thus can be neglected [19]. The MSM shape change can be considered a result only of the variant reorientation. As mentioned above, twin variants start to reorient in fields exceeding certain threshold. This threshold is usually characterised by the value of an external stress needed to overcome

the twinning stress of a crystal. Due to magneto-mechanical coupling, twinning stress is also related to the minimum magnetic field required to initiate reorientation, called *switching field*. It has also been shown that twin boundary nucleation twinning stress differs from the twin boundary propagation twinning stress [20]. This is particularly important for MSM alloys used in actuators.

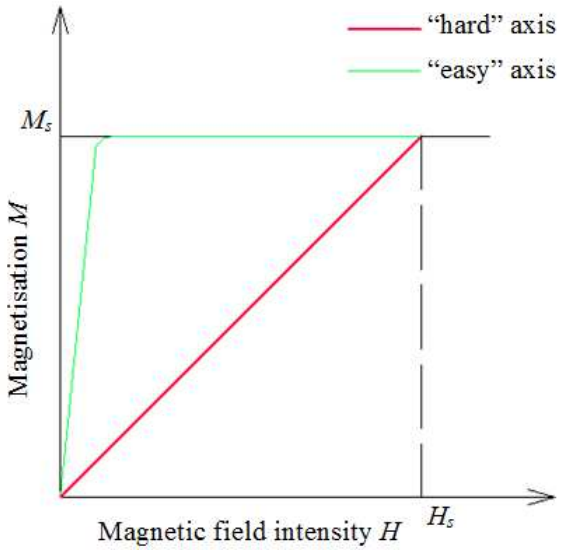

Figure 2.1-2. Typical magnetisation curves of Ni-Mn-Ga alloys

Variant reorientation and growth is always accompanied by magnetisation change in the material, also known as Villari effect [21]. Magnetisation curves are usually included in papers related to the material study, but they are not useful for design and modelling purposes. Figure 2.1-2 shows typical magnetisation curves associated with MSM alloys. M_s and H_s are saturation magnetisation and field intensity, which are roughly 0.7T and 400kA/m for modern crystals. These curves correspond to the two extreme cases: curves for "hard" and "easy" axes measured on single-variant MSM specimen. A "real" curve changes from "hard" to "easy" during elongation[2] [22]. This effect is fundamental for designing MSM sensors and self-sensing actuators. However, magnetisation change during straining is also important for performance evaluation of conventional MSM actuators. Different researchers report different values of "easy" axis relative permeability, unlike "hard" axis relative permeability which is consistently reported

[2] It should be mentioned that this statement is based on a simplistic view of MSM permeability change. A more strict and correct representation of the phenomenon is discussed in Chapter 4.

equal to 2. Reported values for “easy” axis relative permeability varies considerably from 40 [22] to 210 [23]. In this study, it is assumed to be equal to 50 which corresponds to properties of currently available crystals manufactured by ETO Magnetic [24].

However, permeability does not just change from “hard” to “easy” in any obvious or simple way. It has been proposed that a number of so-called effective magnetisation curves can be measured for each strain value of interest and used afterward for modelling the behaviour of the MSM element [22], [25]. These effective curves would lie between magnetisation curves measured for “hard” and “easy” axes. The MSM element can be represented by a single “black box” element in a model. However, such an approach has several important drawbacks. The one having the most significant impact on MSM element representation in actuator magnetic circuit is related to locality of twin reorientation phenomenon being neglected. This translates into inability to capture the saturation of “easy” variants which precedes saturation of “hard” variants resulting in higher MSM permeability predicted by the model. Moreover, this representation predicts a “runaway” change in MSM permeability: the initial shape change leads to increase in magnetic field leading to further shape change, and so on. However, this positive feedback behaviour has not been observed experimentally. Therefore, a more accurate modelling approach that takes MSM permeability change into account is needed.

The significance of MSM permeability change and its influence on actuator magnetic circuit design and optimisation is yet to be fully understood by researchers. A 25 times difference between the initial and final value of MSM relative permeability illustrates the potential for actuator magnetic circuit optimisation for minimising its reluctance. Models proposed for accurate representation of varying MSM properties along with the approach developed and used in this study are discussed further in Chapter 4. This approach is used afterwards for design and optimisation of MSM actuators in Chapter 5.

2.1.1 Twinning stress and twin boundaries

Twinning stress is commonly used for characterising the mobility of twin boundaries in MSM crystals. It is related to the stress required to propagate a twin boundary resulting in shape change [26]. This property is particularly important since it defines the magnetic field needed to activate the MSM element. However, twinning stress also acts as internal friction opposing any external stimuli and dissipating energy in magneto-mechanical cycling. On the other hand, twinning stress is responsible for the shape memory effect in MSM crystals: MSM element maintains its current state until a force overcoming twinning stress is applied. Therefore, MSM crystals exhibit a holding force which can be calculated as

$$F_{hold} = \sigma_{TW} \cdot A_{msm} \tag{2.1-1}$$

where σ_{TW} is twinning stress, MPa, and A_{msm} is MSM element's cross section area, mm^2. Twinning stress is commonly viewed as drawback for actuator applications desired to be as small as possible. It has been continuously decreasing over the years as quality of MSM crystals is improving. 2MPa twinning stress was considered very low in 2001 [26] whereas 0.5MPa was reported in 2009 [27]. This was achieved through increasing purity of manufactured crystals [27], [28] along with application of thermo-mechanical training [29]. Twinning is actually a very complex phenomenon and accurate prediction of twinning stress in new crystals is a very complicated task [30]. Many models describing twin boundary mobility and internal structure of the variants were proposed [31], [32]. However, it is still hard to certainly predict properties of MSM alloys beforehand. Moreover, the same crystal can have different twining stress values associated with different variants.

New crystals with very low twinning stress below 0.1 MPa were reported in 2011 [33]. These crystals were considered very prospective for use in EM devices due to magneto-mechanical conversion with much higher efficiency. Such low twinning stress is a feature of so-called Type II twin boundaries. Whereas, these twin boundaries are indeed very mobile, their effect on microstructure stability currently limits their applicability. This is discussed further in Section 2.2.

In general, two types of twinning stress can be distinguished – initial and conventional twinning stresses [34]. It has been noticed that energy required for nucleating twin boundaries is much higher than the one required for moving pre-existing boundaries [35]. The former is related to initial and the latter to conventional twinning stresses. Initial twinning stress can be up to five times the conventional twinning stress, making applications ineffective if boundaries extinct and nucleate during cycling. However, MSM element can have pre-existing twin boundaries nucleated due to application of mechanical loads. Whereas use of MSM element with pre-existing boundaries slightly decreases maximum possible strain, it otherwise has very positive effects on overall fatigue life. It should be mentioned that only conventional twinning stress is considered in many papers and the word "conventional" is usually omitted. Similarly, the term "twinning stress" is used only for describing the stress required for propagating existing twin boundaries in this study.

MSM element can be in a single- or a multi-variant state with respect to the number of variants. MSM element is considered to be in a *single-variant* state when it is fully compressed or elongated. Thus, its microstructure consists only of one variant and no twin boundaries are present. One can see that it is first necessary to nucleate a twin boundary for initiating elongation and, hence overcome the initial twinning stress. Since this is not efficient, a *multi-variant* state or a state with pre-existing twin boundaries is preferable. Microstructure of MSM element consists of multiple twin variants separated by twin boundaries in a multi-variant state. If the number of variants and, hence the number of twin boundaries is big, such microstructure is called *fine twins*. Conversely, a state with only one twin boundary is called a *two-variant* state with a *single twin boundary*. It was discovered that a single twin boundary needs lower external stress to be moved and, hence propagates in weaker fields comparing to fine twins. Also, twinning stress associated with a single twin boundary is nearly constant, unlike fine twins' twinning stress which tends to increase during elongation [36], [37]. One of the remarkable features of a single twin boundary is its ability to propagate freely after a strong enough stimulus is applied. However, single twin boundary samples tend to tilt in magnetic fields leading to problems in actuation [28]. Fine twins' microstructure does not have this disadvantage which makes it more prospective for actuation. It should be mentioned that one common way to nucleate fine twins is simply by bending an MSM

specimen. Hence, a single specimen can be in a multi- or two-variant state depending on initial conditions.

It is also important to mention that twinning stress can considerably vary from crystal to crystal. This can have a significant effect on performance of designed MSM actuators as has been shown by studying the influence of 20% variation in twinning stress on actuator performance [38]. The results emphasise the importance of finding a way to consistently manufacture crystals with pre-determined characteristics, as otherwise it is hard to predict the actuator performance reliably.

Twin boundary mobility is also different in MSM crystals in multi- or two-variant states. Highly mobile twin boundaries with twinning stress below 0.1 MPa were observed only in two-variant state MSM elements. Further study has led to understanding that these new twin boundaries are different from previously observed twin boundaries with average and high twinning stress. The former are now called Type II and the latter Type I twin boundaries. The reason for very high mobility of Type II twin boundaries is yet to become clear. Nevertheless, multiple experiments are confirming very low twinning stress less than 0.1 MPa e.g. [17], [39]. Moreover, the lowest Type II twin boundary twinning stress of 0.01 MPa and corresponding switching field of 30mT have been reported [18]. Twinning stress of Type II twin boundaries also does not depend on temperature [40], which can significantly simplify actuator control and performance stabilisation. On the contrary, Type I twin boundary twinning stress decreases with temperature. This implies increasing output force produced by a designed actuator as temperature increases. On the other hand, variation of actuator output with temperature is not a desirable quality.

2.1.2 Magneto-mechanical hysteresis

Twinning stress discussed in the previous Section results in considerable magneto-mechanical hysteresis being exhibit by MSM crystals. In general, hysteresis represents a dependence of system's parameters not only on its current state, but also on the history of its previous states. It also results in a memory effect due to nonlinear relation between certain parameters. However, two types of hysteresis can be distinguished in case of MSM alloys: magneto-mechanical and thermal hystereses. Magneto-mechanical

hysteresis leads to a nonlinear dependence of strain on applied stress or magnetic field. Thermal hysteresis appears during phase transformation leading to a small difference between heating and cooling phase transformation temperatures and related values of magnetisation. It plays no significant role in conventional MSM applications unless phase transformation is the main mode of operating.

Magneto-mechanical hysteresis modelling and associated control strategies are subject of an ongoing research [41]–[43]. Researchers suggest different analytical approaches and different control strategies. Usually, Preisach-like hysteresis operators or inverse hysteresis maps are used. Obtained equations are always bulky and hard to deal with. Fortunately, hysteresis is not a problem for on/off actuation systems studied in this Thesis. It is possible to design an actuator with a sufficient accuracy avoiding dealing with the magneto-mechanical hysteresis directly.

Figure 2.1-3 illustrates the relation between the twinning stress and the hysteresis phenomenon in mechanical cycling: width of a hysteresis loop is equal to a doubled twinning stress in a reversible actuation. This figure is courtesy of AdaptaMat [44]. It also means that energy $\approx 2 \cdot \sigma_{TW} \cdot \varepsilon_0$ dissipates in each mechanical cycle [28]. However, the size of hysteresis loop also changes with load. This is discussed further in Chapter 5 (see Fig. 5.1-1).

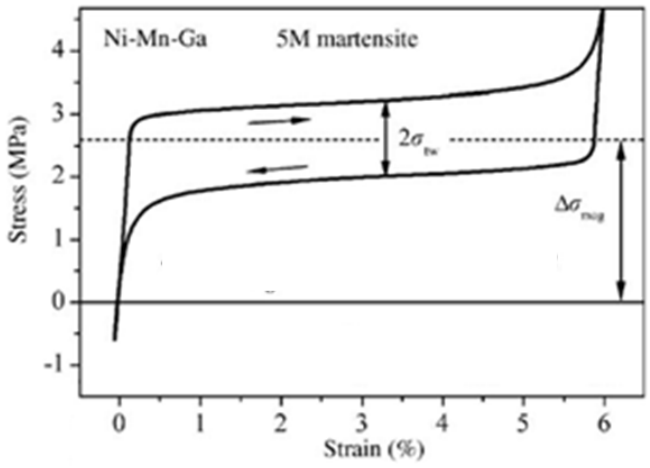

Figure 2.1-3. Magneto-mechanical hysteresis associate with reversible MSM effect

2.1.3 Magnetic field-induced stress

MSM elements can be operated by magnetic fields or mechanical stresses, or a combination of both. The latter is the most common mode of operating in MSM actuators. Likhachev and Ullakko have formulated a universal rule [2] stating that magnetic and mechanical stresses acting on a twin boundary are coupled and act in exactly the same way. Practically, this means that both mechanical and magnetic field-induced stresses may be written in one equation. This is very useful for evaluating operating conditions of MSM actuators. However, a relationship between the magnetic field B and magnetic field-induced (MFI) stress σ_{mag} should be established first.

Different analytical models for calculating MFI stress have been proposed [45]–[48]. While exposed to external magnetic field, magnetic anisotropy between "easy" and "hard" magnetisation axes results in magneto-stress production in the material. Maximum value of MFI stress is called *blocking stress* which depends on lattice crystallographic distortion ε_0 and magnetic anisotropy energy constant K_U

$$\sigma_{Block} = \frac{K_U}{\varepsilon_0} \tag{2.1-2}$$

For conventional Ni-Mn-Ga alloys this value is 3 MPa [49] at ambient temperature. However, 3.5 MPa blocking stress is reported by EtoMagnetic [24] as well as by Aaltio [50]. As the blocking stress depends only on material parameters, high anisotropy energy is essential for a large-force output.

Blocking stress can be calculated as maximum MFI stress [47]

$$\sigma_{\mathrm{mag}} = \varepsilon_0^{-1} \int_0^h (M_a(H) - M_t(H))dH \tag{2.1-3}$$

where $M_a(H)$ and $M_t(H)$ are magnetisation values of axial ("easy") and transverse ("hard") twin variants. This model requires experimental stress-strain data for evaluating overall MSM element behaviour. Whereas it allows qualitative and quantitative evaluation of MSM crystals' behaviour, its applicability to actuator design currently seems questionable, as discussed further in Chapter 4.

In general, MFI stress must exceed two stresses in order to initiate the variant reorientation. The first one is twinning stress. The second one is external compressive stress applied to the MSM element in reversible actuation. The part of the stress "available" for external loading can be calculated as

$$\sigma_{eff}(B) = \sigma_{mag}(B) - (\sigma_{TW} + \sigma_{Comp}) \tag{2.1-4}$$

where σ_{Eff} is effective stress related to output stress [46], $\sigma_{TW}$is twinning stress and σ_{Comp} is compressive stress produced by mechanical spring. Equation (2.1-4) illustrates that effective stress can be considerably lower than MFI stress even in strong magnetic fields. It also shows the effect of twinning stress on actuator performance.

Strain produced by MSM element also depends on applied load. Larger loads complicate twin boundary motion and decrease the strain. Therefore, a combination of required stress and strain should be considered for every application. This is particularly relevant to MSM actuator design since the decrease in available strain can make certain stress-strain combinations unavailable.

A minimum value of magnetic stress required to initiate the shape change can be deduced from Eq. (2.1-4) yielding

$$\sigma_{Mag.min}(B) = \sigma_{Tw} + \sigma_{Comp} \tag{2.1-5}$$

One can see that the minimum stress depends only on twinning stress in absence of the mechanical spring. This clearly illustrates the relation between twinning stress and switching field. Therefore, materials with low twinning stress are preferable providing an opportunity to design small and low power consuming device. This can be also illustrated through considering the efficiency of reversible actuation of an unloaded MSM element as

$$\eta \approx \frac{(\sigma_{mag} - 2 \cdot \sigma_{TW})}{\sigma_{mag}} \tag{2.1-6}$$

Equation (2.1-6) allows getting a rough estimate of the dependence of MSM efficiency on twinning stress. Table 2.1-1 summarises the results calculated using 3 MPa magnetic stress [49].

Table 2.1-1. Efficiency of MSM crystals with different twinning stress

σ_{TW}, MPa	0.05	0.1	0.2	0.5	0.8	1	1.4	≥1.5
η, %	96.7	93.3	86.7	66.7	46.7	33.3	6.7	0

Table 2.1-1 illustrates how rapidly MSM efficiency decreases with twinning stress. For instance, Twin II crystals with 0.1MPa twinning stress convert almost 95% of input energy into mechanical work, whereas almost one third of the energy is dissipated by Twin I crystals with 0.5MPa twinning stress.

Considering the number of different stresses needed to be taken into account for analysing MSM element's and actuator's behaviour, it would be helpful to provide a short summary in order to avoid possible confusion. This is done in Table 2.1-2. It also illustrates advantages and drawbacks of using MSM elements with Type I and Type II twin boundaries.

Table 2.1-2. Summary of different stresses related to MSM element performance

Parameter	Related to	Depends on	Type I	Type II
σ_{Block}, MPa	Maximum stress which acts on a twin boundary	Crystal microstructure	3.5	3.5
σ_{TW}, MPa	Internal friction	Crystal microstructure	~0.5	≤0.1
σ_{comp}, MPa	External compression for reversible actuation	$\geq\sigma_{TW}$	≥0.5	≥0.1
σ_{eff}, MPa	Maximum output stress of an actuator	$\sigma_{MAG} - (\sigma_{comp} + \sigma_{TW})$	2.5	3.3
σ_{load}, MPa	Effective load of an actuator	Up to σ_{eff}	2.5	3.3
$\sigma_{load,tot}$, MPa	Real load of an actuator	$\sigma_{load} + \sigma_{comp}$	3	3.4
Maximum number of operating cycles	Fatigue life	Crystal microstructure	$>2\cdot10^9$	$\sim10^6$

2.1.4 Temperature behaviour of MSM crystals

MSM alloys can operate in a broad temperature range. Research reports include results of experiments conducted at temperatures as low as 20 K [51] going all the way up to 330-350 K [52], [53]. One can see that a major part of this temperature range lies considerably below room temperature. Moreover, the 60-80°C operating temperature limit is rather low comparing to other materials used in EM actuators and sensors. This limit is determined by martensite-austenite transformation temperature of an alloy. Ni-Mn-Ga phase transformation temperature depends strongly on alloy composition [45]. However, capabilities of conventional crystals are not sufficient and further increase in operating temperature is needed in order to implement MSM alloys in various EM applications. Applicability of MSM materials in systems where a substantial amount of heat is generated is currently limited. The ongoing research in the field of MSM material study aims to increase their operating temperatures. The first major advance leading to increase in transformation temperature from 60 to 80°C has been recently reported [53].

It should be noted that two temperatures are to be considered when the maximum possible operating temperature is evaluated. The first one is martensite-austenite transformation temperature above which the material exhibits no MSM effect. The second one is material's Curie point. However, Curie temperature is higher than the phase transformation temperature in available Ni-Mn-Ga alloys.

There are three main parameters that are affected by change in temperature: twin boundary mobility related to twinning stress σ_{TW}, lattice distortion c/a related to the maximum strain ε_0, and anisotropy energy constant K_U related to the MFI stress σ_{mag}.

Twinning stress tends to decrease with temperature. For instance, twinning stress has been shown to decrease from 0.8 MPa at 20K to 0.1 MPa at 300K [51]. An increase in strain under constant load was also observed with increasing temperature illustrating the same phenomenon [25]. Such effect is only possible when twinning stress decreases. The same dependence was also observed in magnetic cycling [54]. Simultaneously, twinning stress change affects the switching field. Therefore, switching field of MSM crystals decreases with temperature. Decrease in twinning stress due to increase in

temperature is particularly relevant to real applications. This can be illustrated by almost 1% shape change due to a 15ºC temperature increase [25].

In general, magnetic stress is a function of both anisotropy constant and lattice distortion. However, it varies just slightly above room temperature. Its behaviour at low temperatures has been studied [51]. An increase in anisotropy constant with decreasing temperature has been reported [55]. The significance of this increase was also illustrated by an enormous 5.7 MPa MFI stress observed at -95ºC [56]. This stress is almost twice the room temperature blocking stress. However, this is not particularly relevant for actuators working above room temperature.

The experimental results reported [57] show how maximum strain decreases with temperature. This suggests bigger possible shape change at lower temperatures. However, simultaneous increase in twinning stress leads to rapid decrease in reversible strain in magnetic cycling limiting applicability of the material. Lattice distortion decreases almost linearly with temperature above 0°C. This explains the decrease in MFI strain and switching field with temperature in [50]. MSM properties are arguably the best when close to phase transformation temperature [58]. However, stable operation of MSM element on a verge of losing its properties is a rather risky endeavour. On the other hand, this implies that MSM element heating in actuator during operation may actually play a positive role.

Temperature of MSM element is determent by ambient temperature, heat flow from other parts of a device and heat generated inside the material. The effects of the latter were studies by several research groups. A small 2°C increase in temperature in 300 Hz mechanical cycling have been reported [7]. This result suggests that electromagnetic sources of heat would play a dominant role in MSM thermal state evaluation in actuators. This can be illustrated by a 6ºC increase in temperature after just 30s in a strong 400 Hz magnetic field [59]. Therefore, thermal state of MSM actuator should be carefully evaluated for preventing MSM element from overheating.

2.1.5 Frequency response of MSM crystals

From a material study point of view, the question of frequency response of MSM element is related to twin boundary mobility. MSM alloys are usually tested in quasi-static fields where frequency-related effects can be neglected. However, research results related to operating at 100-500 Hz and even 1-2kHz can be found.

The most promising of the reported results have shown linear increase in MFI strain with frequency [59]. A one order of magnitude twin boundary velocity increase was observed as frequency increased from 50 to 400 Hz. In addition, a 25% increase in twin boundary mobility by reducing the rise-time of a pulsed field from 10 to 1 ms has been observed [60]. It was also suggested that twin boundaries can overcome defects and travel longer distances at high frequencies.

However, a non-linear dependence of MSM strain on frequency has been reported [61], [62]. It was observed in experiments involving MSM actuators. Obvious peaks on curves are explained by the resonance phenomenon in the device showing that maximum strain can be obtained on natural resonance frequency. In these experiments, strain increases with frequency below resonance and rapidly decreases afterwards. However, an underling reason for such a sharp decrease is not clear. Similar results were reported by researchers studying acoustic-assisted MFI strain [63], [64], where external varying stress was used in order to enhance twin boundary mobility. A remarkable increase in strain was observed at low frequencies below resonance along with simultaneous decrease in switching field. However, almost no effect was reported for frequencies above the resonance frequency. As mentioned above, a complete understanding of frequency behaviour of MSM actuators is not reached yet. Nevertheless, several recent papers consider resonance of an actuator as the best operating point [64], [65]. Doubling of strain and increasing response speed make this phenomenon very promising for use in actuators.

Response time is a very important characteristic of MSM actuators and sensors. Response time of MSM crystals close to 0.2ms was reported in several papers [66], [67]. Such a short response time suggests that the material can be activated by rapidly changing magnetic fields or mechanical stresses. Researchers have shown that the

response time of MSM element is lower than that associated with electric and magnetic processes in MSM actuators [59], [68]. Moreover, mechanical parts of an actuator can be even more inert, contributing poorly to overall response speed. All these effects are not unique for MSM actuators and can be addressed through careful design.

2.1.6 MSM alloys as high temperature SMAs

Utilisation of the MSM effect and shape change due to variant reorientation is the main subject of this study. However, MSM phase transformation can also be used for producing strain and stress output. It this case, MSM shape is controlled by heat rather than magnetic fields. However, the shape change occurs at a particular (phase transformation) temperature unlike gradual straining due to the twinning stress change discussed in Section 2.1.4.

Phase transformation can also be induced mechanically. However, it requires applying a considerable 20-200 MPa stress to the MSM specimen [69]. The main advantage of phase transformation induced shape change is remarkably high output stress. For example, a 0.5% strain was observed under 24MPa load at -60°C [70].

It was suggested that MSM alloys can be used as high-temperature SMAs. Conventional SMA alloys (such as Ni-Ti) work only below 100°C whereas Ni-Mn-Ga crystals can exhibit shape change due to phase transformation up to 400ºC [44]. In this case, MSM alloys are operated as SMA alloys. MSM alloys designed specifically for this type of operation are commonly referred to as high temperature shape memory alloys (HTSMAs). A study on the properties of different alloy compositions optimised for this use was recently reported [71]. Since shape change due to phase transformation becomes the main work regime for these alloys, thermal hysteresis also becomes relevant. For instance, 5ºC thermal hysteresis was observed on a strain-temperature curve in [72].

2.2 Fatigue life of MSM crystals

MSM crystals have potential for very long fatigue life. In spite of the fact that Ni-Mn-Ga crystals were considered brittle, long $200 \cdot 10^6$ cycles actuation without malfunction was reported in 2002 [62]. Nowadays, the most comprehensive work on the study on MSM crystals' crack growth and fatigue life is carried out by Aaltio and summarised in his Thesis [50] and related papers [7], [73]. Among the obtained results, the most prominent one is $2 \cdot 10^9$ cycles without malfunction in 300Hz mechanical cycling. Whereas a slight decrease in specimen performance was observed, the specimen did not crack throughout the experiments. Such long fatigue life illustrates the potential for designing very long-life MSM-based devices.

One of potential advantages of using MSM alloys in actuators is related to output displacement being produced by shape change rather than bulk movement of a particular element. However, fatigue properties of MSM crystals significantly depend on specimen microstructure. Twinning phenomena in MSM single-crystals can result in twin boundary arrangements which lead to crack growth. This is particularly relevant for high purity crystals with very low twinning stress Type II twin boundaries. Their microstructure tends to be unstable resulting in nucleation of twin boundaries with orientation different (up to 90°) from the main straining axis. Very low nucleation twinning stress also leads to very high probability of such twin boundaries to occur. These boundaries act as obstacles for the main reorientation twin boundary and initiate crack growth.

300Hz mechanical cycling experiments summarised in [7] show several interesting aspects of MSM fatigue behaviour. First, a remarkable increase in twinning stress from 0.1MPa to 1.5MPa is reported for one of the specimen which is related to obstacle growth mentioned above. Moreover, that sample cracked after as little as 10^7 cycles. It was discovered that operating an MSM element with pre-existing twin boundaries leads to avoiding this phenomenon. This result can be used when organising actuator's operating cycle, as discussed in Chapter 5.

This can be supported further through analysing the experimental setup in [7]. The most promising result ($2 \cdot 10^9$ cycles) was obtained using a Twin I MSM element with 0.6MPa

twinning stress. The maximum peak-to peak strain was only 2%, varying specimen strain between 3 and 5%. This illustrates how partial operating cycle can be used for preventing MSM element from turning into a single variant, as discussed in the previous Section.

Different experiments were conducted by Lawrence *et al.* [74]. A rotating magnetic field was applied to the MSM specimen resulting in its elongation and contraction. However, a rapid crack growth was observed which led to malfunction of the specimen. The cracks were originating from twin boundaries nucleated during field rotation. Several important results were obtained which can be generalised. First, it is important that MSM element is connected to a mechanical holder by a side with no twin boundaries. Otherwise, magnetic field-induced stresses may result in specimen fracture since twin boundary motion is supressed in that region. Whereas the rotating magnetic field excitation mode is not common for conventional MSM actuators, several designs that utilise it were proposed [75].

Unfortunately, the results obtained in MSM actuators fatigue experiments are much less promising: just 425 million [37] and 23 million cycles [76] are reported. The study in [37] also shows a rapid decrease in output force of an actuator. However, as authors admit, it was not clear whether properties of MSM element or actuator design resulted in such short fatigue life. It is indeed harder to analyse results of experiments conducted on MSM actuators. Nevertheless, an important observation was made in [77]. Actuator air-gaps are usually rather small since they contribute significantly to overall reluctance. However, MSM element can tilt slightly during operating which may result in mechanical friction between it and actuator poles. This leads to crack nucleation and subsequent malfunction. It was also pointed out that application of incorrect control can significantly decrease fatigue life of MSM actuator. Another result related to this phenomenon is reported in [78] where MSM element bends due to considerable Maxwell stresses originating from air gap asymmetry.

Summarising the discussion above, several rules for ensuring a long fatigue life can be formulated:

- Twin I MSM crystals with average twinning stress should be used in long-lifetime applications especially when operating frequency is high.
- MSM element should be prevented from turning into a single-variant state. This can be done by operating it in a partial strain cycle using MSM element with pre-existing twin boundaries.
- MSM element should be connected to the holder by its side with no twin boundaries. The magnetic field should be lower in the area of the connection for decreasing magnetic field-induced stresses.
- MSM element should not have any mechanical contact with actuator's core. This can be ensured using MSM elements with fine twins rather than a single twin boundary. Use of a symmetric air gap is also needed for minimising Maxwell stresses.

2.3 Potential application in actuators and other EM devices

MSM alloys are very promising to be used in EM devices. Actuation is one of the most prospective applications of MSM alloys. Depending on a particular design and technical task, MSM actuators can be high-performance, fast, compact and efficient. Enormous fatigue life of MSM crystals provides an opportunity to designing actuators with very long lifetime. Nowadays, the most common mode of operating is linear elongation/contraction. Nevertheless, research publications on the use of bending and torsion can be found which is particularly prospective for microactuators [54], [79].

The most common linear MSM actuator magnetic circuit design is shown in Fig. 2.3-1. A transversal (horizontal in the picture) magnetic field produced by a coil is applied to the MSM element for producing displacement in longitudinal (vertical in the picture) direction. Magnetic circuit of an actuator consists of a flux guide made of magnetic steel with high permeability, excitation coils and/or permanent magnets (PM), and MSM elements between core poles. A source of compressive force should also be included in this design for reversible actuation. Most commonly, a mechanical spring is used in MSM actuators for this purpose.

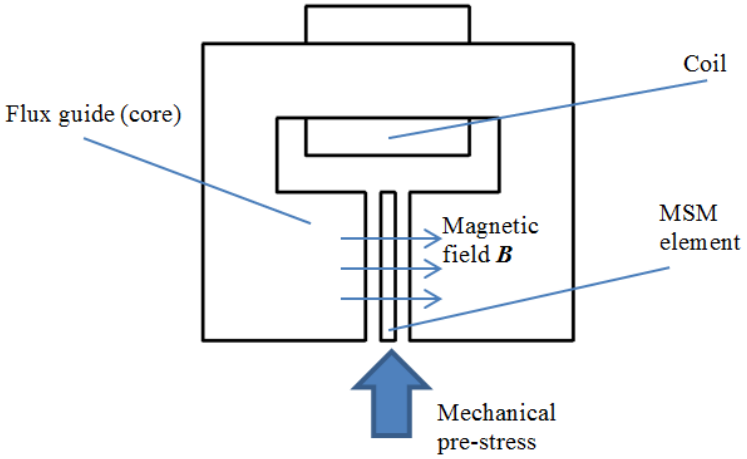

Figure 2.3-1. MSM actuator operating principle

As mentioned above, two forces are required for operating MSM element in reversible cycling: one for elongating the material and another one for contracting it. None of these two forces should necessarily be of electromagnetic nature or, conversely, both of them can be induced by magnetic fields. Five possible combinations (called operating modes) were discussed by Holz *et al.* in [80], [81] providing a very useful framework for analysing possible actuator designs.

Operating modes represent possible combinations of magnetic and/or mechanical stimuli which allow utilising the MSM shape change. Operating mode 1 corresponds to two mechanical forces used for both elongation and contraction. MSM element acts as a passive element in this operating mode. This mode can be used in active dumpers due to mechanical energy dissipation associated with the MSM shape change. Operating mode 2 corresponds to magnetic elongation and mechanical contraction. This operating mode is related to the most common MSM actuator arrangement, as one in Fig. 2.3-1. The main disadvantage of this mode is a decrease in output force due to pre-stress. A possibility to disable pre-stress during elongation can be a possible solution. However, this is not possible with a mechanical spring since it acts throughout a complete cycle.

Operating mode 3 corresponds to a transversal mechanical force and longitudinal magnetic field. This operating mode is rather exotic since it utilises the idea that mechanical contraction of MSM element in one dimension leads to its elongation in another one. However, this is the first operating mode where a magnetic force is used

for contracting the MSM element. Application of the magnetic field along the motion direction can also simplify the design since a coil can be wound directly around the MSM element. However, application of a transversal mechanical force can be a complicated task from perspective of mechanical analysis.

Tensile mechanical stress and magnetic field are applied along the MSM element strain axis in operating mode 4. Similar to the previous operating mode, a problem of providing this tensile stress complicates possible actuator designs. Moreover, the application of tensile stress instead of compressive one can result in a significant decrease in fatigue life and stability.

Finally, both forces are generated by magnetic fields in operating mode 5. This mode seems to be the most interesting for EM actuation as both elongation and contraction can be controlled magnetically. Moreover, it is possible to activate these forces one at a time. This allows avoiding magnetic stress decreasing which occurs in operating mode 2. This operating mode also allows controlling MSM element shape during contraction which is not possible with mechanical spring [81]. It was suggested that two magnetic circuits are needed for this operation mode [82]. However, a design with a single magnetic circuit is discussed below. A particularly unconventional design utilising operating mode 5 including two coils and no flux guide (magnetic flux conducted through air) was also presented [68]. However, that design was used mainly for measuring the response speed of the MSM element.

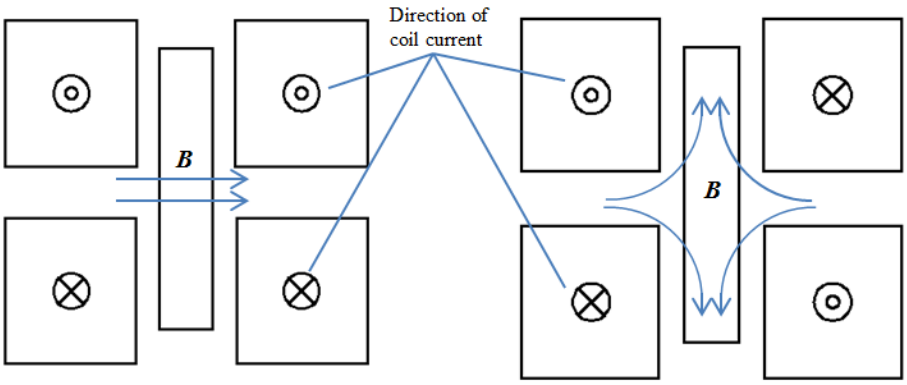

Figure 2.3-2. Rotating magnetic field with a pair of coils in operation mode 5

An interesting implementation of operating mode 5 is through creating a rotating magnetic field using two coils or a coil and permanent magnets. Figure 2.3-2 shows how a rotating magnetic field can be created with two coils: the magnetic field is horizontal when coils' currents are co-directional leading to MSM element elongation, whereas opposite direction of currents leads to a 90° rotation of magnetic field axis resulting in MSM element's contraction. Therefore, an additional magnetic circuit is not needed. However, designing magnetic core in such an actuator can be very challenging. One can see that magnetic flux density is concentrated in the middle of the MSM element during elongation, whereas this part lacks magnetic energy during contraction. Moreover, core steel can get locally saturated since width of MSM element is much smaller than its length. Another notable disadvantage of this approach is increased power consumption and electric losses since the actuator is always operated by current. In actuators implementing the operating mode 2, half of a cycle is operated only by mechanical forces. In this new design, both contraction and elongation are controlled using electromagnetic energy leading to bigger energy loss.

An idea to use two MSM elements for improving the position control accuracy has led to a "push-push" actuator design, which nowadays is receiving more and more attention [83]. In this case, a movable part is allocated between two MSM elements linking them together. Excitation of one MSM element leads to its elongation along with simultaneous contraction of another one, whereas mechanical link moves in a direction of elongation of the first MSM element. When excitation signal is removed, actuator maintains its position due to internal holding forces of MSM elements. Therefore, excitation current can be applied as short impulses in windings corresponding to different MSM elements. Whereas this design allows efficient and accurate positioning, its size is much bigger comparing to conventional MSM actuator designs due to two MSM elements and two coils. Also, twinning stresses in each MSM element decreases the actuator output force. Nevertheless, this design does not require an additional restoring force and its position can be controlled throughout the cycle. A concept of a "push-push" actuator was also the underlying idea for designing a MSM-based clamping device, where two MSM elements are used for opening and closing a single clamping jaw [84].

MSM actuator designs using permanent magnets and a coil were presented in [81], [82]. A “push-push” actuator using a magnetic field produced by permanent magnets for elongating an MSM element was designed and manufactured in [80]. Moreover, a magnetic field produced by coils was used for rotating the total field leading to MSM element contraction in that design. The net magnetic field was rotated by almost 90º by controlling coil current. However, strong permanent magnets (NdFeBr in that particular design) and large current were needed. Nevertheless, this prototype illustrates an interesting design solution which was also successfully tested and used to control a valve.

A design which is yet to be studied includes excitation coils for elongating and permanent magnets for contracting an MSM element. This design allows substituting a mechanical spring by permanent magnets allowing contracting MSM element magnetically. This design has the same disadvantage as operating mode 2 does, which leads to decreasing the output force. However, the option of designing an actuator without a mechanical spring can be beneficial for actuator lifetime. A magnetic circuit design of such actuator will definitely require analysing 3D magnetic field distribution due to mutual influence of coil and PM fields.

Utilisation of MSM shape change in a micro-fluid pump for bio-medical application was proposed in [9]. This application differs from all others by its use of locality of MSM shape change. A traveling wave of electromagnetic excitation is produced by a rotating permanent magnet leading to local reorientation of MSM twin variants. An area corresponding to “easy” variant forms a cavity between twin boundaries which carries a drop of liquid along the length of MSM element. This application illustrates explicitly that MSM effect is local and shape change of particular variants can be utilised as source of motion. The pump also does not require a power source for generating the magnetic field due to the use of a permanent magnet. However, it still requires power for rotating the magnet.

Permanent magnets can also be used for providing constant magnetic field in order to decrease current required for producing required magnetic flux. This may also lead to decrease in the number of coil turns also decreasing electrical losses and supply power demands. However, an MSM element would require a larger compressive pre-stress due

to constant magnetic stress induced by permanent magnets. This means further decrease in output force in comparison with actuators designed without permanent magnets. Therefore, this design requires a trade-off between output force, size, and efficiency.

Different actuator designs based on operating mode 2 are discussed in [23], including a rare linear actuator with MSM element of cylindrical shape. Actuators of this type can be fast and compact, providing a considerable output force. Unfortunately, coils of these actuators are still rather big requiring extra space for allocating them and limiting the opportunity to design very small devises. This also holds for actuators designed in Chapter 5 of this Thesis. As Twin II alloys have very low twinning stress, actuators based on these alloys can be much smaller due to reduced coil dimensions. However, this applies to large-strain rather than large-force actuators since MSM element behaviour depends on total load. On the other hand, considerable twinning stress of Twin I MSM crystals complicates the control of intermediate strains due to magneto-mechanical hysteresis [85]. However, the "push-push" design illustrates a way to overcoming this unfavourable property and even turning it into advantage.

Magnetically controlled shape change is only one of several interesting properties of MSM crystals. It was suggested by several research groups that MSM actuators can utilise their full potential only when multiple aspects of MSM phenomenon are used in the same device [58], [86]. For instance, resistance and permeability of MSM crystals vary with shape change. This allows designing actuators capable of sensing their position. This can be done by adding a circuitry that measures either resistance [87] or inductance [88] for real-time displacement evaluation. Such self-sensing actuators possess closed-loop control circuitry significantly improving their positioning accuracy. Self-sensing actuator designs were also studied in [89], [90]. However, size of a self-sensing actuator increases due to the necessity to accommodate a sensing element e.g. an extra coil for measurements.

Nowadays, main applications of MSM alloys include actuators for valves, linear motors, and pumps. A design of a rotating actuator was presented in [75], where movement of a linking rod connecting two MSM elements in differential actuator was converted into rotation of a rotor. Moreover, application of inverse characteristics was proposed for use in sensors, energy harvesters and dampers.

Several papers were published comparing MSM and EM solenoid actuator designs [23], [58]. Different designs and design strategies are also discussed in [91], [92]. These papers show that the same magnetic circuit design methodology can be applied for MSM actuator design as for more studied EM solenoid actuators. Core size is usually chosen with regard to possible saturation, also avoiding using excessive amounts of steel which may lead to unnecessary increase in cost and weight. Air gaps between parts of magnetic circuit should be minimised due to low permeability of air. Coil design is related to choosing the best combination of current and number of turns for providing the required magnetomotive force (mmf). The number of turns affects inductance of the coil which affects the response speed, whereas large electric current can lead to overheating. Therefore, a careful design of the magnetic circuit is essential for efficient and reliable actuator performance.

It was discussed in Section 2.1.5 that resonance phenomenon can be used for enhancing actuator performance. Effects of different design parameters on resonance frequency were studied in [61]. It was discovered that natural resonance frequency is strongly affected by spring constant, MSM element stiffness, and flux guide dimensions. This result suggests the possibility of optimising a design for operating at a specific frequency. However, stiffness of MSM element varies with MSM strain and, hence depends on the applied field. A significant 800MPa to 20MPa decrease in MSM Young Modulus was reported in [93]. This problem was studied further in [65]. Both papers show evidence of a considerable increase in output strain at resonance frequency.

Inverse characteristics of MSM alloys can also be used in wide range of electrical devices. For instance, application of mechanical stress changes MSM magnetisation leading to fluctuations in magnetic flux. This varying magnetic flux can be converted into electric current by a pick-up coil [94]. The converted energy can be used for supplying a low-power consumer. This example illustrates the applicability of MSM alloys for energy harvesting.

Harvesting mechanical energy that otherwise dissipates in a form of acoustic vibrations was suggested in [95], [96]. Efficiency of MSM energy harvesting can be increased by operating MSM element in a bias magnetic field. A study conducted in [97] shows that induced voltage is proportional to the applied field. It is also proportional to the

magnitude and frequency of the external mechanical force. Permanent magnets were suggested as a source of bias magnetic field, avoiding the necessity to accommodate an additional energy source and a second winding. Output power of few milliwatts for MSM energy harvesting was predicted in 2007 [98]. However, 20 mW at 43 Hz were reported in 2014 [44]. A comparison of MSM alloys with magnetostrictive and piezoelectric materials has shown their advantage over other “smart” materials for energy harvesting in [99].

Low twinning stress is desirable for MSM alloys application in energy harvesting. However, energy dissipating properties associated with it can be used for designing dampers. MSM vibration damping devices have been studied by several research groups [100]–[103]. The main parameter that characterizes damping properties of MSM alloys is internal friction or loss tangent ($tan\delta$). It is related to the amount of energy that is dissipated in cycling. 20% internal friction at low strains was reported in 2006 [100] whereas this value increased to 50% at 2-3% strain reported in 2012 for a Ni-Mn-Ga composite [101]. The latter is remarkably high. It is also worth noting that this result corresponds to a hybrid material which costs less than pure MSM crystals being relatively simple in manufacturing. $Tan\delta$ tends to increase with temperature (maximum at transformation temperature) and/or strain, and can also be adjusted by changing hysteresis loop of MSM alloy. However, the available data provides different information on frequency dependence of loss tangent. A slight decrease in $tan\delta$ with frequency was observed in [100] whereas the opposite dependence was reported in [101].

Chapter 3. Mathematical modelling of physical processes in MSM actuators

3.1 Multi-field nature of the problem

MSM actuators produce motion by converting electromagnetic energy into mechanical one. This makes solution of an electromagnetic problem most important for accurate design and performance evaluation. However, MSM electromagnetic phenomenon also affects thermal fields, as a considerable amount of heat can be generated due to electromagnetic and mechanical losses. This leads to change in temperature of different actuator parts affecting its operating regime. This is particularly relevant to the MSM element due to high sensitivity of its properties to temperature. Therefore, knowing temperature distribution in MSM actuator is as important as evaluating its electromagnetic state. Moreover, thermal and electromagnetic fields are actually coupled since thermal phenomena also affect electric and magnetic properties of actuator elements. Ultimately, a complete electromagnetic-thermal- mechanical coupled problem should be considered for evaluating MSM actuator dynamics including the behaviour of its moving parts. However, such analysis becomes too complicated and decoupled (single-field) problems should be discussed first.

All electromagnetic processes on a macroscopic level are described by a system of partial differential equations called Maxwell's equations. Four Maxwell's equations are

$$\nabla \times \boldsymbol{B} = \mu_0 (\boldsymbol{J} + \varepsilon_0 \frac{\partial \boldsymbol{E}}{\partial t}) \tag{3.1-1}$$

$$\nabla \times \boldsymbol{E} = -\frac{\partial \boldsymbol{B}}{\partial t} \tag{3.1-2}$$

$$\nabla \cdot \boldsymbol{E} = \frac{\rho}{\varepsilon_0} \tag{3.1-3}$$

$$\nabla \cdot \boldsymbol{B} = 0 \tag{3.1-4}$$

where $\boldsymbol{E}$ is the electric field intensity, V/m, $\boldsymbol{B}$ is magnetic flux density, T, $\boldsymbol{J}$ is current density, A/m^2, ρ is the electric charge density, C/m^3. The universal constants are free

space permittivity ε_0 and free space permeability μ_0. $\nabla\cdot$ can also be written as divergence operator and $\nabla\times$ as curl operator. First equation is also known as Ampere's Law with Maxwell's addition, second equation – as Faraday's Law. Last two equations represent Gauss' Law in electrical and magnetic forms, respectively. A continuity equation for electromagnetic problem representing the law of conservation of charge is

$$\nabla\cdot\boldsymbol{J}=-\frac{\partial\rho}{\partial t} \tag{3.1-5}$$

Constitutive equations are

$$\boldsymbol{D}=\varepsilon_r\varepsilon_0\boldsymbol{E} \tag{3.1-6}$$

$$\boldsymbol{B}=\mu_r\mu_0\boldsymbol{H} \tag{3.1-7}$$

$$\boldsymbol{J}=\sigma\boldsymbol{E} \tag{3.1-8}$$

where D is electric flux density, C/m^2, and σ is the electric conductivity, 1/Ohm·m. Equation (3.1-7) is especially important when ferromagnetic materials are considered. In this case, relative permeability $\mu_r>1$ and depends on the applied field. This requires knowing material B-H curves for actuator magnetic circuit elements, including the MSM element.

A typical B-H curve of ferromagnetic material is characterised by sections with large and low relative permeability μ_r due to saturation. Saturation is related to a state where all ferromagnetic domains are aligned with bias field so further increase in field intensity produces only slight increase in flux density. Saturation flux density is an important parameter which allows evaluating capabilities of different flux guide materials. In general, materials with higher saturation flux density allow designing more compact and efficient EM actuators. Another type of permeability called incremental permeability should also be mentioned. It characterises how change in field intensity

leads to change in flux density. For instance, incremental permeability of saturated material is free space permeability μ_0. However, relative permeability of such material can still be high since it is calculated using magnitudes of magnetic field intensity and flux density. It is important to distinguish the two since FE software used in this study always calculates relative permeability rather than incremental permeability. This explains how saturated steel or MSM "easy" variants discussed in Chapter 4 can have permeability exceeding free space permeability.

Frequency-dependent processes should also be considered when AC power supply is used. Varying magnetic and electric fields are sources of skin effect in electric wires, hysteresis and eddy-current losses in flux guide. Eddy-currents are induced in conducting regions by varying magnetic fields in accordance with Eq. (3.1-2) and (3.1-8), decreasing the efficiency and leading to extra heat dissipation. Lamination of magnetic core is commonly used for decreasing these losses through increasing electrical resistance. Eddy-currents also produce their own magnetic field which locally decreases the total magnetic field. This leads to variation of flux density throughout the flux guide. The parameter used to characterise this effect (skin effect) is called depth of penetration

$$\delta = \frac{1}{\sqrt{\pi f \mu \sigma}} \tag{3.1-9}$$

where f is excitation frequency, Hz. Equation (3.1-9) shows that the higher the frequency, permeability and conductivity are, the lower the depth of penetration is, meaning that a smaller part of the whole material is conducting magnetic fields. Therefore, highly permeable steel is subjected significantly to this phenomenon. Calculation of eddy-current losses is a complicated task. For particular geometry of the magnetic circuit studied in [104], associated losses per unit mass are

$$P_{edd} = \frac{(\pi B d f)^2}{6 k \rho D} \tag{3.1-10}$$

where B is a magnitude of magnetic flux density, T, d is thickness of the steel sheet, m, k is a constant equal 1 for steel and 2 for wires, ρ is resistivity of the material, ohm·m, D is density of the material, kg/m^3. However, accurate estimation of eddy-current loss is a subject of electromagnetic transient analysis. Hysteresis losses are another source of energy dissipation in actuator flux guide. Magnetic losses produced are proportional to hysteresis loop size. Therefore, materials with a thin hysteresis loop are preferable. These losses per unit mass are

$$P_{hys} = \frac{\oint HdB}{D} \tag{3.1-11}$$

Total magnetic losses per unit mass can be calculated as a sum of these two components

$$P_{mag} = P_{hys} + P_{edd} \tag{3.1-12}$$

It should be mentioned that flux density variations during transient processes (for instance, switching impulse current) also induce eddy-currents that result in power losses. This is particularly relevant for operating cycles discussed in Chapter 5. However, Eq. (3.1-9) and (3.1-10) are only applicable for harmonic excitation. This complicates evaluating magnetic losses in cycles involving pulsed excitation.

Electrical (Joule) losses can be calculated using a well-known formula

$$P_{el} = I^2 R \tag{3.1-13}$$

where I is magnitude of electric current, A, R is resistance, ohm. Coil wires can also be affected by skin effect leading to non-uniform current distribution and increase in electric resistance. However, skin effect is negligible for 0.5 mm wires at frequencies up to 300Hz used in this study (approximately 3mm skin depth).

Joule losses can considerably increase actuator temperature. The main ways of heat transfer are conduction, convection and radiation. Heat is mainly transferred through conduction between solid bodies, i.e. different parts of an actuator. Heat flow due to conduction can be described by Fourier's law

$$\boldsymbol{q} = -k_c \nabla T \tag{3.1-14}$$

where q is heat flux, W/m^2; k_c is thermal conductivity, W/m·K; T is temperature, K. Operator ∇ can also be written as gradient. Losses generated in actuator should be conducted into the environment for avoiding unacceptable increase in temperature. External cooling may be required when losses are too high and cooling conditions are too poor. Heat exchange between the MSM element and the environment is defined by convection. This is the second type of heat transfer in which fluid (such as air or water) is used as heat mediator. It is described by Newton's law of cooling

$$Q_n = k_f A_c (T_s - T_{amb}) \tag{3.1-15}$$

where Q_n is normal component of heat flux at a convective surface, W, k_f is convective film coefficient, W/K·m^2, A_c is total area of convection surfaces, m^2, T_s is temperature of MSM actuator surface, K, T_{amb} is ambient temperature, K. Heat can also be transferred through radiation. This is the last heat transfer mechanism related to energy emitted by a very hot object in a form of electromagnetic radiation. However, radiation is negligible at temperatures MSM element is capable of working on.

Motion of a push-rod in MSM actuator is described by a complete form of Newton's Law of Motion [105]

$$M\frac{d^2u}{dt^2} + C\frac{du}{dt} + Ku = F_{net} \tag{3.1-16}$$

where u is displacement, m, M is mass, kg, C is damping, N·s/m, K is stiffness, N/m, F_{net} is net force acting on a push-rod, N. However, this equation is not particularly useful since MSM variant reorientation phenomenon is very complicated. For instance, parameters C and K are non-linear functions of displacement. For this reason velocity and acceleration of MSM twin boundaries are usually studied only experimentally. Moreover, this study does not include calculations related to MSM motion dynamics.

3.2 Two approaches to analysing actuator magnetic circuit

3.2.1 Equivalent electric circuit approach

Field theory of electromagnetism provides the most comprehensive picture of the phenomenon. However, Maxwell's equations have no general solution which complicates their applicability in actuator design. On the other hand, much simpler models can be used for preliminary design or even rather accurate solution of electromagnetic problem in relatively simple cases. One of the most popular approaches relies on finding a solution for equivalent electric circuit of actuator magnetic circuit. It should be mentioned that circuit models are simplified representations of more complete and complicated field problems. However, they are somewhat easier to understand and require much less sophisticated mathematics to work with. The idea of considering flux lines as 1D tubes for which equation can be written goes as far back as to the original works of Maxwell [106].

Electric circuits are well-studied and even complicated arrangements of circuit elements can be solved using Kirchhoff's laws [107]. Magnetic flux, mmf and reluctance are equivalent to current, voltage and resistance by analogy. However, the assumptions a circuit model is built on should be carefully considered. Each element of an equivalent electric circuit assumes all related properties being uniform and homogeneous. Therefore, regions with different geometry and/or magnetic properties are represented by different elements in a circuit. Magnetic flux and mmf are related as

$$\Phi = \frac{F}{R} \tag{3.2-1}$$

where Φ is magnetic flux, Wb, F is mmf, A, R is reluctance, 1/H. Equation (3.2-1) is also called Hopkinson's law. Mmf produced by a coil can be calculated as

$$F_c = \oint Hdl = N_c \cdot I_c \tag{3.2-2}$$

where N_c is number of coil turns, and I_c is coil current, A. Reluctance of a circuit element is

$$R = \frac{l}{\mu_r \mu_0 A} \tag{3.2-3}$$

where l is length, m, A is a cross-section area, m^2, $\mu_r\mu_0$ is permeability, H/m. Equation (3.2-3) shows that reluctance depends only on geometry and material properties of an element. Mmf produced by a coil depends on the number of turns and applied current. Figure 3.2-1 shows an equivalent electric circuit of magnetic circuit of MSM actuator.

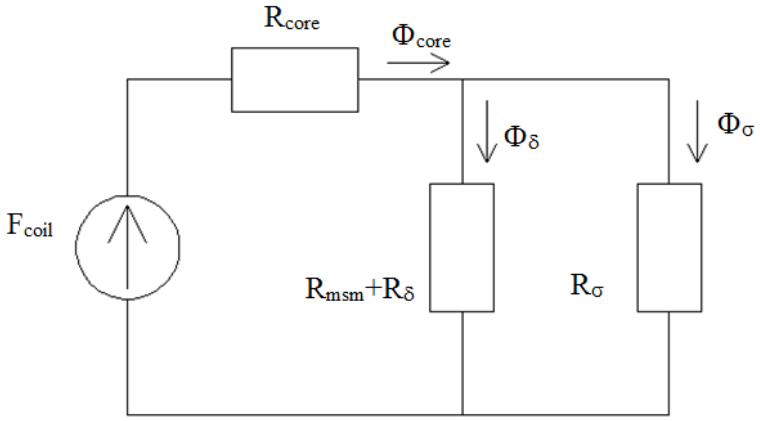

Figure 3.2-1. Equivalent electric circuit of MSM actuator magnetic circuit

Kirchhoff's circuit laws have an analogy in magnetic circuit leading to zero total flux in each node and equal mmf drop on parallel branches. It can be illustrated for the circuit Fig. 3.2-1 as

$$\begin{cases} \Phi_{core} = \Phi_\delta + \Phi_\sigma \\ F_{coil} - F_{core} = F_\delta = F_\sigma \end{cases} \tag{3.2-4}$$

Magnetic flux is not very useful for MSM actuator analysis since it depends on geometry of a particular region. Magnetic flux density B is commonly used instead

$$B = \frac{\Phi}{A} \tag{3.2-5}$$

This approach is rather simple and allows changing parameters easily in order to see how they affect the overall solution. The main disadvantages of this approach are

associated with its assumptions: as uniform flux distribution is assumed, it is hard to represent a complex geometry correctly; linear parameters do not allow taking saturation into account. This limits the accuracy of the solution and overall capability of the approach. For this particular research, where alloys which properties vary locally are studied, implementation of this approach is generally both complicated and unreliable. It has indeed been used for analysing special states. However, a more flexible approach should be considered which can be applied in all cases.

3.2.2 Finite element analysis

Finite element method (FEM) is a numerical technique that can be used for finding an approximate solution for a system of differential equations for given boundary conditions. This is done by dividing a complex domain into a net of simple subdomains (mesh) called elements, equations for which can be written in a more simple form. This is a powerful technique when complex geometry and non-linear material properties are involved. However, accuracy of this approach depends on the number of elements and their size leading to a very fine mesh needed for accurate representation of complex objects. This leads to considerable computational challenges. An error associated with mesh quality (called discretisation error) cannot ever be fully eliminated. Quality of the mesh and, hence number of elements is directly responsible for accuracy of the solution, as well as computational time. However, mesh can be refined for areas of high interest and kept relatively rough elsewhere. This allows decreasing computational time significantly. Local refinement is particularly relevant to meshing EM actuator magnetic circuit geometry where fields tend to vary considerably in particular areas due to saturation of ferromagnetic regions. Moreover, domains with different material properties can be included in a single model. This allows modelling a compete magnetic circuit of MSM actuator keeping track of mutual influence of different actuator parameters.

Nowadays, FE models are usually built based on real solid body geometry through meshing and assigning relevant material properties to domains. The geometry can be created either in a design module of a FE package or by using a different computer-aided design (CAD) software. Many meshing techniques have been studied this far [108]. Some researchers are using available open source data for creating their own FE

algorithms. However, a commercially available ANSYS Multiphysics software package is used in this study. It uses a particular type of mesh with elements of triangular shape for handling electromagnetic analysis. Triangular elements allow more efficient geometry meshing also handling well refining at particularly difficult regions such as magnetic circuit corners. It should be mentioned that all calculations related to meshing the model and obtaining the numerical solution are done by the software and only a few parameters are controlled externally.

FEM allows writing field equations for every node of the mesh. However, those still need to be converted to a simpler form in order to apply numerical methods. For steady-state problems, partial differential equations are reduced to algebraic equations which are solved using methods of numerical linear algebra such as Newton-Raphson's method [109]. For transient problems, a system of ordinary differential equations is solved. The most common numerical methods used for solving those equations are Euler's and Runge-Kutta's methods [108]. To find a solution means finding spatial (and time, if transient) distribution of a function of interest which satisfies boundary conditions under applied loads. The solution is found through continues iterative procedure which minimises out-of-balance part of equations to a value less than a specified tolerance. It is said that a problem converges to a certain solution if this criterion is satisfied. Change in solution between two consequent iterations is also monitored for ensuring smooth change in field vectors. Convergence criteria are very important due to their influence on accuracy of the solution. On one hand, high tolerance can lead to rapid convergence to a poor or non-physical solution due to discontinuity in the field. On the other hand, low tolerance can lead to enormous computational time or even inability of the solver to reach convergence (non-converged solution). Therefore, convergence criteria should be carefully considered for every problem being solved. It should also be kept in mind that the function minimised by FE solver is free energy and other field parameters of interest are derived from it. Thus, some field parameters have potential to accumulate bigger error than others.

Sources of excitation are represented by loads applied on solid bodies or elements. For electromagnetic problems, these include current, current density, electric potential difference (voltage drop) and coercive force (for permanent magnets). Fixed values of magnetic potential at boundaries can also be used to model external fields. For thermal problems, loads are represented by generated heat and temperature constraints.

Maxwell's equations should be written using magnetic potential formulation in order to be solved using FEM. Two possible formulations for magnetic fields include magnetic scalar potential ψ and magnetic vector potential A formulations. For electric fields, electric scalar potential ϕ is used. This allows writing magnetic field equations as

$$\boldsymbol{B} = \nabla \times \boldsymbol{A} \tag{3.2-6}$$

$$\boldsymbol{H} = -\nabla \psi \tag{3.2-7}$$

$$\boldsymbol{E} = -\nabla \phi - \frac{\partial \boldsymbol{A}}{\partial t} \tag{3.2-8}$$

A, ψ and ϕ are the degrees of freedom (DOF) used by the solver. In case of scalar magnetic potential (MSP) formulation, equations that are solved are

$$\boldsymbol{H} = \boldsymbol{H_g} - \nabla \phi_g \tag{3.2-9}$$

$$\nabla \cdot \mu \nabla \phi_g - \nabla \cdot \mu \boldsymbol{H_g} - \nabla \cdot \mu_0 \boldsymbol{M_0} = 0 \tag{3.2-10}$$

$$\boldsymbol{H_g} = \frac{1}{4\pi} \int \frac{\boldsymbol{J} \times \boldsymbol{r}}{r^3} dV \tag{3.2-11}$$

where H_g is preliminary magnetic field obtained using Biot-Savart law Eq. (3.2-11), A/m, ϕ_g is generalised potential, A, μ is absolute permeability, H/m, M_0 is magnetisation of permanent magnets, A/m, r is a radius-vector. This formulation is primarily used for models developed in this research. However, magnetic vector potential (MVP) formulation is used for solving 2D problems. In this case, Poisson equation is solved for out-of-plane z component

$$\nabla^2 \boldsymbol{A_z} = -\mu \cdot \boldsymbol{J_z} \tag{3.2-12}$$

An unconstrained field problem can have infinite number of solutions. Therefore, FE analysis requires boundary conditions specified for outer boundaries of the modelled region. Boundary conditions also represent interaction of the model with the surrounding environment which is not included explicitly. Two most common types of boundary conditions are Dirichlet and Neumann boundary conditions. The former constrains potential at the boundary, whereas the latter constrains its normal derivative. For scalar magnetic potential, this yields

$$\begin{cases} \psi = 0 \\ \dfrac{d\psi}{dn} = 0 \end{cases} \tag{3.2-13}$$

where the former is Dirichlet and latter is Neumann zero boundary conditions. Similar equations can be written for magnetic vector potential, or any potential used for describing a specific boundary-value problem.

3.2.2.1 Discretisation error and convergence

Magnetic fields are continuous. However, a field solution obtained via FEA is not necessarily continuous. It only approximates the real continuous solution with a net of interconnected elements. Moreover, derivatives of DOFs can be even more discontinuous than the potentials they are derived from. Discretisation error is related to the discontinuity in question, also allowing assigning a value to it.

Discretisation error can be estimated by comparing flux density vector (in magnetic analysis) for a particular point with average flux density vector at this point [108]. Each point has a number of flux density values associated with it equal to the number of elements that share this point. Therefore, the discretisation error can be written as

$$\Delta \boldsymbol{B}_n^i = \boldsymbol{B}_n^a - \boldsymbol{B}_n^i \tag{3.2-14}$$

where $\boldsymbol{B}_n^i$ is flux density vector for point *n* of element *i* and $\boldsymbol{B}_n^a$ is the average flux density vector. One can see that flux continuity between neighbouring elements would be perfect given zero discretisation error. However, this does not happen in reality. Discretisation error should be carefully monitored for ensuring reliable accuracy of the solution. Software packages like ANSYS provide useful tools allowing automatic meshing and Smart Sizing. The study in [110] shows that implementation of Smart Size tool allows decreasing errors and achieving convergence in fewer iterations.

Convergence is also related to the stability of the solution. Low discretisation error does not necessarily indicate that the solution is correct. For instance, the same study shows that quality of the mesh can significantly affects the results which otherwise seem correct. Variation in solution with mesh quality is a subject of mesh study. A satisfactory number of elements is one that ensures both low error and negligible change in solution with further increase in the number of elements.

Chapter 4. FE analysis of MSM actuators

4.1 Application of FEM to MSM actuator modelling

FEM possesses distinctive advantages over other methods when non-homogeneous and anisotropic regions of complex geometry are analysed. It is used as the main tool for modelling the electromagnetic and thermal fields in MSM actuators in the following Chapters. This Chapter discusses how the MSM actuator can be modelled using FEA software. Whereas modelling of every element of the magnetic circuit is discussed, it should be mentioned that MSM element is the only non-conventional part in comparison with traditional EM solenoid actuators. Hence, the question of its representation in the model plays a significant role in the overall analysis. It is also very important to be able to relate the magnetic field solution in the magnetic circuit with the overall actuator output. This Chapter presents a detailed discussion of the development of such modelling approach with a consequent analysis of the magnetic field distribution in the MSM element and a study of its permeability change during the shape change. The latter is than applied to the actuator design in Chapter 5.

Two software packages were used for EM actuator modelling: ANSYS Multiphysics and FEMM. FEMM is free open-source software for 2D analysis which was used at early stages of the research. However, Fig. 4.3-11 is the only result obtained using FEMM which is included in the final version of this Thesis. This is primarily due to inability of FEMM to handle non-linear anisotropic properties of MSM elements. Nevertheless, it allows much better visualisation of the results. Where possible, both FEMM and ANSYS were used for solving 2D problems in order to compare the results. Some aspects of field distribution are much easier to comprehend in FEMM due to much more gradual scale of change (which translated into colours in pictures). ANSYS Multiphysics modules use only 10 different colours for visualising the solution. This is a great disadvantage when non-homogeneous magnetic fields are to be analysed. However, ANSYS allows modelling anisotropic non-linear properties of MSM element. Thus, all final results are calculated using ANSYS. Furthermore, all actuator designs are developed in ANSYS since 3D magnetic field distribution plays a crucial role in their magnetic circuit analysis and optimisation.

4.1.1 Magnetic circuit model composition

An MSM actuator magnetic circuit model consists of flux guide (ferromagnetic core), a coil, an MSM element and interior/exterior air regions. Magnetic properties are assigned to all elements in form of constant relative permeability (air, coil, MSM "hard" axis) or non-linear B-H curves (core, MSM "easy" axis). Loads are applied to coil elements. Dirichlet boundary conditions are assigned to exterior boundaries of the model.

Figure 4.1-1 shows a typical 2D model of MSM actuator in ANSYS. It should be mentioned that loads are applied differently depending on whether a model is 2D or 3D. In 2D, loads are applied as total coil current density. It is related to the real coil current as

$$J_{model} = \frac{I_c \cdot N_c}{a_c \cdot b_c} \tag{4.1-1}$$

where I_c is input current, A, N_c is number of coil turns, a_c and b_c are width and height of the coil, mm. "Plane53" element is used in 2D electromagnetic analysis in ANSYS. This element consists of 6 nodes when triangular mesh is used. Both ANSYS and FEMM use MVP formulation for handling 2D electromagnetic analysis.

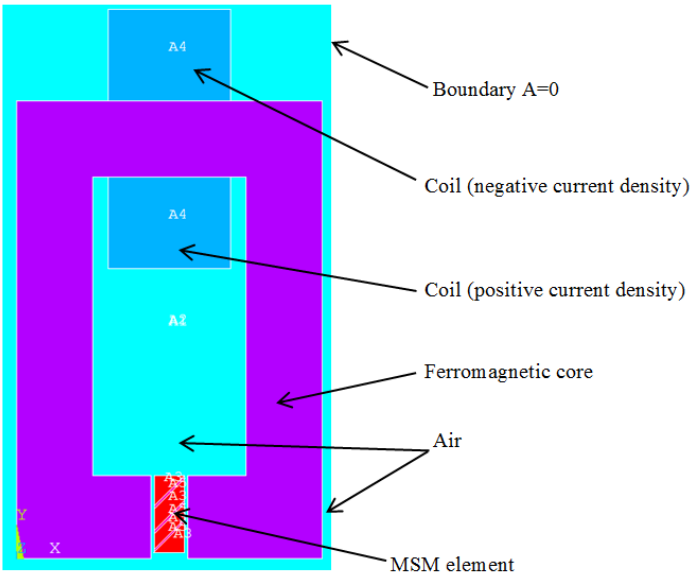

Figure 4.1-1. Typical 2D MSM actuator model in ANSYS (surrounding air is partly hidden)

Figure 4.1-2 illustrates mesh quality in studied 2D models. The number of elements lies between 30 and 150 thousands depending on the level of mesh refinement and model size, about 30% of which are in the air gap region. Bigger numbers usually lead to negligible increase in accuracy while computational time increases significantly.

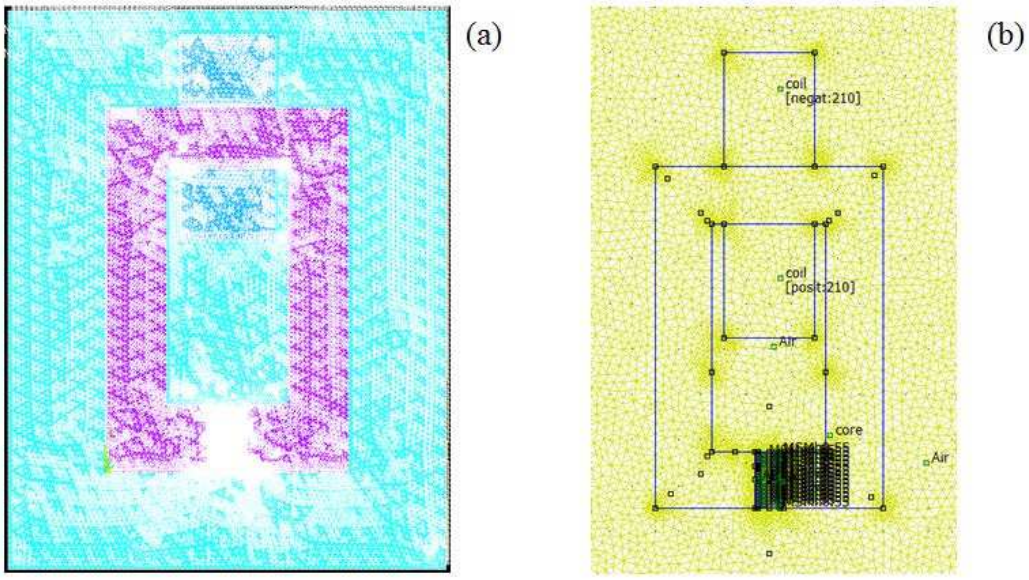

Figure 4.1-2. Mesh quality in (a) ANSYS and (b) FEMM models

ANSYS 3D models are built using “solid96” element. This is a tetrahedral element which implements MSP formulation. It has 8 nodes per element. Coil here is created not by meshing solid body geometry but by using a “racetrack coil” macro. This macro uses coil geometry and mmf as its input. It creates coil directly as “sourc36” elements. Setting up a 3D model is similar to setting up a 2D one in other aspects. Number of elements used in 3D ANSYS models varied from $250 \cdot 10^3$ for actuators with simplistic geometry to $3.5 \cdot 10^6$ for HU actuator design (see Chapter 5). The latter is related to poor convergence in models which use Hypermco 50 steel.

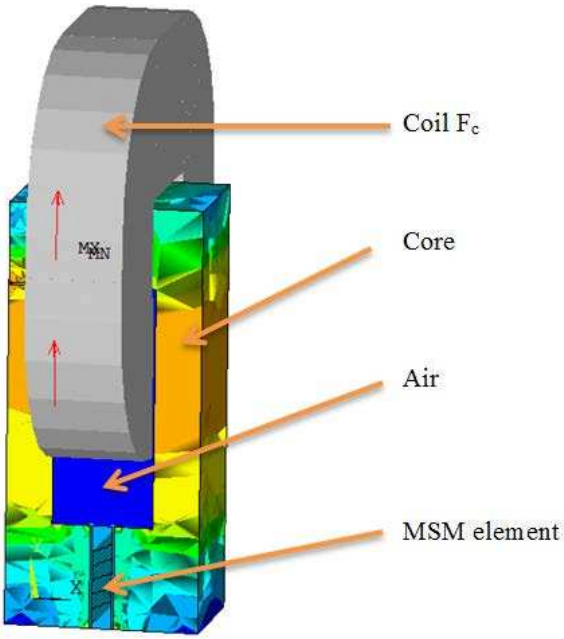

Figure 4.1-3. 3D MSM actuator model in ANSYS (surrounding air is hidden)

The surrounding air is included in all models in order to take leakage fluxes into account. These tend to increase with core saturation, whereas the difference between models with and without the surrounding air is essentially negligible in weak fields. Flux leakage also increases considerably in 3D. This illustrates the importance of solving a complete 3D actuator model for accurate evaluation of its performance.

Size of the air cube (surrounding air) also affects the accuracy of the obtained solution. Since zero boundary conditions are “enforced” on its exterior, magnetic field distribution in the MSM actuator magnetic circuit should be consistent with this constraint. This may result in change in MSM magnetic flux when outside boundary is too close. On the other hand, big air cube can significantly and unnecessarily increase computational time. Thus, an optimal size should be found. The analysis has shown that the effect of outer boundary proximity becomes negligible when it is at least 50mm away from the magnetic circuit. However, this value was as small as 10mm for some models with low core saturation levels. These results were used for setting up actuator models in the most optimal way.

4.1.2 Convergence study and numerical errors

Almost all models developed as part of this study did converge using default mesh settings, apart from several Hypermco-based designs. Therefore, this Section mostly discusses the influence of mesh size on accuracy of the obtained solution. Yet, it should be mentioned that convergence in ANSYS is estimated using magnetic flux as reference (SMP formulation). The convergence criterion tolerance is 0.001 yielding 0.1% difference between the subsequent solutions.

Meshing of the models was performed using ANSYS built-in MeshTool. It uses Smart Size algorithm for varying element size non-uniformly throughout the mesh being smaller in narrow regions or near the corners and, on the opposite, being bigger in less special regions. Overall quality of the mesh can be adjusted using Smart Size parameter which varies from 10 (most coarse) to 1 (finest). Mesh quality can be improved further through local (or complete) refining. Model refinement can be performed using a 1 to 5 scale with latter corresponding to the highest depth of refinement. However, it is also possible to perform multiple consequent refinements for achieving better results. Refinement level 2 is also not equivalent to two consequent refinements level 1, leading to high flexibility of mesh quality adjustment.

Different aspects of the analysis were important in different models. For instance, 2D models were used for analysing magnetic field distribution in actuator magnetic circuit and particularly MSM twin variants in Chapter 4. 2D models have much less elements comparing to 3D models allowing getting results rather quickly which is an advantage when general trends of field distribution are analysed. However, a deep refinement of MSM element region was necessary for conducting calculations summarised in Section 4.3.2. This is the case since slight discontinuity in the field does not affect the overall solution much. However, even relatively small local error was unacceptable for proving the argument in that particular experiment. Increasing the number of elements to 185000 allowed decreasing the error to the negligible 10^{-6}. Nevertheless, such accuracy was not needed in other 2D models making this the case only for models studying continuity in the field at a twin boundary. However, since 3D models were actually used for MSM actuator design and performance evaluation, it is more relevant to discuss their convergence and accuracy.

The detailed analysis of MSM actuator designs is summarised in Chapter 5. However, it should be mentioned for purposes of this Section that air gap flux density is the main parameter of intersect in 3D. Maximum flux density in the core was also carefully monitored for analysing saturation conditions. Therefore, variation of these parameters with mesh quality is worth studying. However, an additional tool can be used for estimating discretisation error associated with a particular model using EMAGERR macro for calculating error norms for regions corresponding to a particular material. Error norm is calculated as a ratio between the relative error and the maximum value of magnetic flux density. This does not assign a single number to the error associated with the whole model. On the contrary, errors for particular regions (e.g. MSM element, core) can be calculated. This approach makes possible to estimate errors for particular regions of interest.

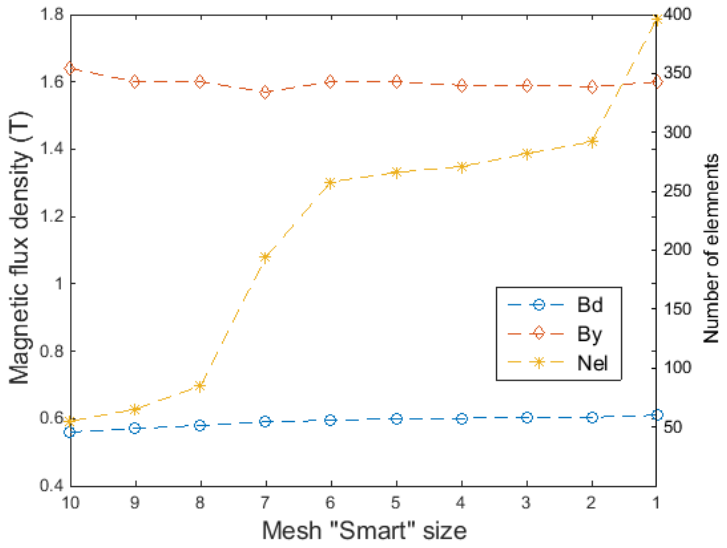

Figure 4.1-4. Change in flux density and elements' number with "Smart Size" parameter

Figures 4.1-4 and 4.1-5 show results of the convergence study. Figure 4.1-4 shows the slightly increasing trend of air gap flux density B_d and decreasing yet fluctuating trend of yoke flux density B_y. This suggests that the number of elements N_{el} still affects the solution. However, further increase in mesh quality achieved by refining Size 1 mesh has led only to 0.002 T change in air gap flux density. On the other hand, refining the model has increased the number of elements to 2.5mil causing expected effects on

computational time. This fact along with the data Fig. 4.1-5 suggests that Size 2 mesh is the most suitable for MSM actuator modelling. B_{me} and B_{mh} correspond to MSM "easy" and "hard" variants' errors in Fig. 4.1-5.

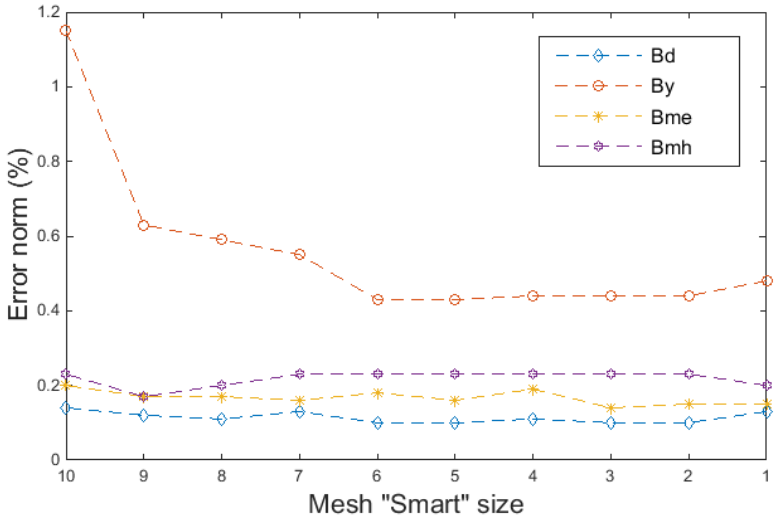

Figure 4.1-5. Change in error norm with "Smart Size" parameter

This analysis is conducted using R actuator model. General trend of mesh quality influence on accuracy of the results holds for other models, too. However, models built using Hypermco 50 (see Section 5.1.2) caused several additional troubles not observed for other materials used. Its B-H curve was causing unexpected numerical errors leading to inability of the model to converge. Whereas its smoothness was checked numerous times and even adjusted with a rational function constructed using an approach proposed in [111], convergence of several models was not reached. Increase in curve's smoothness allowed a number of models to converge. However, the reason for non-converged solution in other models was not identified. Figure 4.1-6 shows fluctuation of error norm in HU actuator model. In some cases, refining the core up to level 2 (approximately 3.5mil elements) allowed to reach a converged solution. Unfortunately, convergence of several models was not reached regardless of the mesh quality. Moreover, a slight change in input parameters as, for instance, number of coil turns from 120 to 115, could also lead to non-converged solution. This illustrates how some models can be sensitive to combination of input parameters' values which lead to considerable numerical errors.

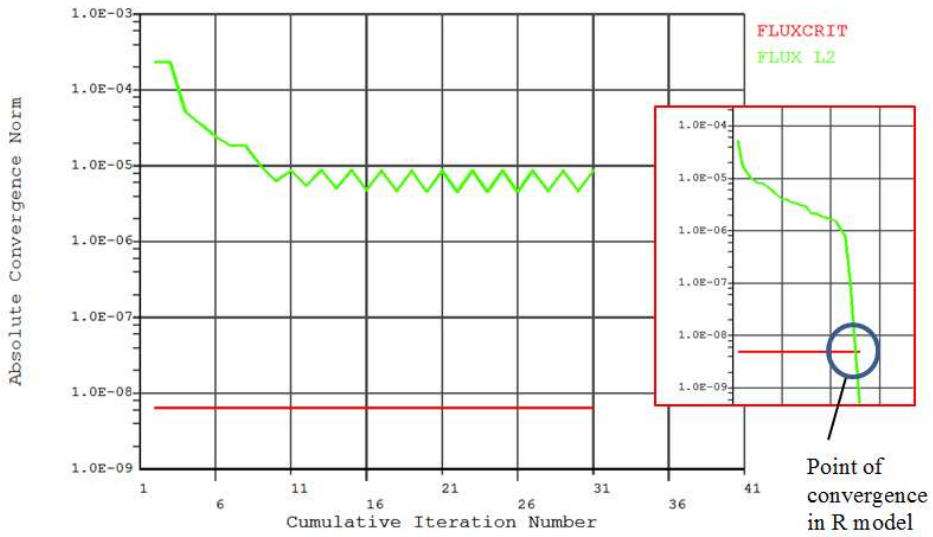

Figure 4.1-6. Un-converged solution in one of HU models (insertion shows the expected behaviour of the convergence curve)

Actuator design and optimisation procedure is discussed in Chapter 5. However, it is worth mentioning that this process essentially consists of the "first guess" step and further variation of the initial design. This requires re-running the analysis a considerable number of times. Moreover, many more runs are needed for optimisation and calculation of output characteristics. This procedure is atomised though organising an algorithm which automatically sets up the model, finds the solution and stores the results. Outline of this algorithm implemented in ANSYS can be found in Appendix 3. Parameters B_δ and B_y are the most important for actuator design. These data are stored alongside with varying input data allowing efficient monitoring of the effects different design parameters have on overall performance. These data were used for finding optimal geometry and coil parameters for every designed actuator.

4.2 Magnetic field-induced variant reorientation and varying MSM permeability

Whereas the magnetic field-induced variant reorientation plays a crucial role in MSM shape change and force production and, thus has been studied rather well, the phenomenon of permeability change has been just barely acknowledged this far. This is partly due to a quite common assumption made by material study researchers that demagnetisation effects can be neglected and the bias field does not change with MSM shape change. However, such an assumption is unacceptable when MSM-based devices are studied. For instance, it is easy to show how MSM element reluctance change affects total reluctance of actuator's magnetic circuit in extreme (fully "easy" or "hard") cases. Moreover, intermediate strain implies mixed state of MSM element being formed by both "hard" and "easy" variants. This case is much more complex requiring taking non-homogeneity into account and, ultimately FE analysis for explaining the permeability behaviour. The next Section gives a brief illustration of the permeability change effects based on a simplistic reluctance model, whereas further Sections present in-depth study of this phenomenon.

4.2.1 Effects of varying MSM permeability on actuator magnetic circuit reluctance

Equivalent electric circuit of actuator magnetic circuit includes one mmf source (a coil) and reluctances corresponding to the core, MSM element, air gaps and flux leakage (see Section 3.2.1). In general, all of these reluctances depend on the applied field in either linear or non-linear manner. However, effects related to core saturation and flux leakage are common for electromagnetic actuators and have already been studied extensively. For illustrating the MSM permeability change effects in the clearest way, only the air gap region including MSM and air reluctances is studied. It is shown in Fig. 4.2-1.

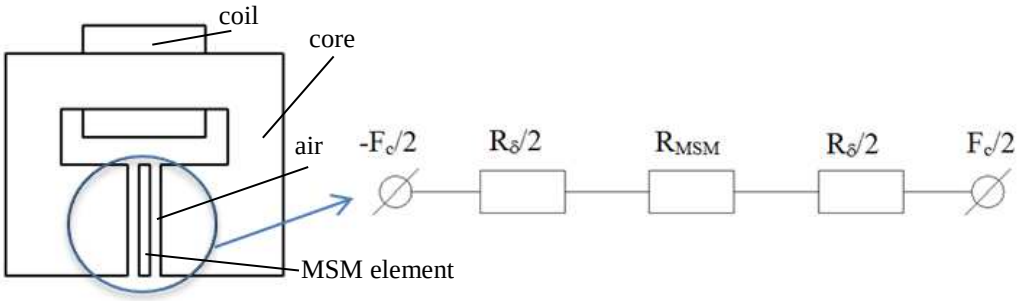

Figure 4.2-1. Equivalent electric circuit of MSM actuator air gap assuming zero mmf drop along the core

In this case, the total magnetic flux can be written as

$$\Phi_t = \frac{F_c}{R_\delta + R_{msm}} \tag{4.2-1}$$

where F_c is coil mmf, A, R_δ is total reluctance of air regions and R_{MSM} is reluctance of the MSM element, 1/H. Air gap reluctance can be written as

$$R_\delta = \frac{\delta + a_m \cdot \varepsilon}{\mu_0 \cdot A_m \cdot (1 + \varepsilon)} \tag{4.2-2}$$

where δ is a total width of the air regions, m, a_m is MSM element width, m, ε is current strain of the MSM element (for 5M Ni-Mn-Ga alloys $0 \le \varepsilon \le 0.06$), A_m is air gap cross-section area transversal to bias field, m^2. The air gap reluctance slightly increases with strain due to decreasing MSM element's width. In the most general form, MSM reluctance can be expressed as

$$R_{msm} = \frac{a_m \cdot (1 - \varepsilon)}{\mu_0 \cdot \mu_m \cdot A_m \cdot (1 + \varepsilon)} \tag{4.2-3}$$

where μ_m is relative permeability of MSM element. Whereas the permeability change is discussed in further Sections, it is possible to do simple yet very informative calculations for either fully contracted or elongated MSM element. In addition, a case of heavily saturated fully elongated MSM element with μ_m=6 is considered. Table 4.2-1 illustrates the results calculated using Eq. (4.2-3) for F_c=200 A, δ=0.2 mm, a_m=1 mm,

A_m=33.5 mm^2. MSM permeability is 2 for fully "hard" and 50 for fully "easy" MSM elements, respectively. The last column shows MSM contribution to the total reluctance.

Table 4.2-1. Change in MSM reluctance and total flux with MSM element strain

MSM element conditions	ε, %	μ_m	R_m, 10^6/H	R_d, 10^6/H	R_t, 10^6/H	Φ_t, 10^{-6}·Wb	R_m/ R_t, %
Fully contracted	0	2	11.9	4.7	16.6	12	71.4
Fully elongated	6	50	0.4	5.8	6.2	32	6.7
Fully elongated, saturated	6	6	3.5	5.8	9.3	21	37.6

A considerable difference in reluctances as well as total flux produced by constant coil mmf in different conditions is clear. In fully contracted state, MSM reluctance accounts for more than 70% of total circuit reluctance, whereas it barely matters when the MSM element if fully elongated. However, this result can still be misleading since it holds only for very weak fields where "easy" variant saturation can be neglected. The last row is much more realistic, still showing a dramatic decrease in MSM reluctance due to the shape change. It is also important that the magnetic flux produced by the coil changes accordingly. This illustrates the importance of taking MSM permeability into account for achieving optimal performance of MSM actuators. However, it is not feasible to use simplistic reluctance modes for actuator design.

4.2.2 Analytical models

Most of available models are based on energy considerations. They are primarily developed for modelling MSM element physics neglecting its influence on the applied field and demagnetisation effects. It is shown further in this Chapter that such an approach fundamentally limits the number of aspects of the MSM shape change phenomenon that can be predicted by the model. Moreover, these models are usually not applicable to actuator design. The only possible advantage is that a solution does not require application of numerical techniques and influence of different parameters can be evaluated relatively easily.

One of the first models for explaining the MSM shape change and evaluating magnetic field-induced stresses was proposed by Likhachev and Ullakko (L-U) at early stages of MSM research [112]. This model had several modifications over the years which have already been mentioned in Chapter 2. This model is still one of the most cited due to fundamental nature of the analysis, which yet is not completely general. This is essentially a 1D model which deals with conversion of MSM magnetic anisotropy energy into mechanical work. Whereas anisotropy lies in heart of this model, MSM element is essentially a "black box" element represented by average magnetisation. Demagnetisation effects are also neglected resulting in inconsistency between magnetic fields inside and outside the MSM element. Nevertheless, this model allows predicting MSM strain-field characteristics when required experimental data for model implementation is available. Fundamental nature of the model also allows evaluating blocking stress very accurately. However, it is not applicable to partial straining or varying load cases, as discussed further in Section 4.4.

One of the advantages of L-U model is its simplicity. Models which advance the number of energy components as well as aspects of MSM shape change become very complicated e.g. [113]–[116]. Effects on accuracy comparing to L-U model are also not exactly clear. However, these models do allow taking more aspects of MSM shape change into account. Therefore, it is possible to conclude that complexity of a model increases with its generality. Unfortunately, these models are not compatible with MSM actuator design and optimisation approaches. The complete approach for MSM actuator design based on analytical representation of MSM shape change phenomenon is yet to be developed. However, such an approach would possess inherent disadvantages common for analytical models treating non-linear properties of ferromagnetic regions as well as inability to capture local saturation accurately. Therefore, whereas these models may be very accurate in representing internal processes in MSM element, they are not practically relevant to design of MSM applications.

A different approach was developed by Gauthier *et al.* in [117]. Their model implements Hamiltonian mechanics for evaluating dynamics of a complete actuator. MSM element is represented using L-U model. An obvious advantage of this model is its applicability to actuator design and the ability to compute various output parameters.

Those not only include strain and force output, but also power loss, efficiency and response speed. However, a number of aspects of MSM behaviour are neglected due to the nature of employed model. This leads to rather pessimistic results computed in [117] which differ significantly from findings obtained in this study. This illustrates the importance of using an accurate model for representing the behaviour of a "smart" material in order to predict actuator performance correctly.

Finally, a number of phenomenological models was proposed, e.g. [118], [119]. Those include models allowing evaluating output of MSM actuator or sensor. However, those models rely on a number of parameters which have no physical meaning and should be known from the experiment for particular MSM crystals or applications. Whereas these models very accurately predict MSM performance in particular cases, they are not necessarily applicable elsewhere. Therefore, their use for design and optimisation of novel MSM actuators is not reliable.

4.2.3 Simulation approaches

Another way of dealing with the problem is by solving the magnetic field equations numerically using FEM. However, there is currently no commercial software for simulating MSM physics. Most of the approaches proposed up to this day are only applicable to modelling the MSM element and its interaction with actuator's magnetic circuit is not considered. Such approaches are clearly not applicable to actuator design and performance evaluation. Moreover, most of them still consider MSM element as a "black-box" with average properties neglecting a number of important phenomena related to non-homogeneity and magnetic anisotropy.

However, FE analysis was used for studying non-uniform magnetic field distribution along with its translation into stress distribution in [120]. This study was advanced even further through analysing stability of MSM microstructure in [121]. Unfortunately, this approach is still based on solving equations not available in general-purpose EM modelling software. Therefore, those are again not applicable to actuator magnetic circuit modelling. Nevertheless, this work illustrates how the understanding of MSM phenomenon can be deepen through applying FE analysis taking into account non-homogeneity and anisotropy of MSM crystals.

A new approach was proposed recently by Schiepp *et al.* in [78]. Capabilities of commercially available software FEMM [122] were used for capturing MSM element's magnetic properties allowing modelling it as part of actuator's magnetic circuit. Whereas certain aspects of the original approach were questionable and additional post-processing was required for magneto-mechanical performance evaluation, this simulation approach finally allowed modelling a complete magnetic circuit of MSM actuator, which is crucial for actuator design and optimisation.

Three MSM modelling approaches were developed by Schiepp in his Thesis [77]: the Stress Based Simulation (SBS), the Dynamic Magnetisation Curve (DMC) and Stress Dependent Magnetisation Curve (SDM) methods. They differ in MSM behaviour representation and its effects on actuator performance, computational time and accuracy. Most importantly, DMC and SDM methods require an enormous amount of experimental data such as magnetisation and stress-field curves at different pre-strain levels. Therefore, these approaches are applicable only to particular cases for which experimental data are available. However, generality is essential for developing novel applications. On the other hand, the SBS method aims to capture macroscopic MSM behaviour as accurately as possible. Its publication along with the data required for its implementation has played a crucial role in making actuator designs and accurate MSM behaviour modelling possible.

The most important advantage of Schiepp's approach is its ability to capture both MSM non-homogeneity and variant anisotropy. This is done by dividing the MSM region into areas corresponding to particular variants. Magnetic properties are assigned to these areas depending on current variant composition. One can see that such an approach requires rebuilding a model for every particular strain, which is time consuming. Nevertheless, it is very accurate also providing an important insight on magnetic field distribution in the MSM region, as discussed in the next Section.

It should be mentioned that whereas non-homogeneity is represented almost identically in this study as in SBS method, the anisotropy is modelled in a completely different way. Moreover, the most fundamental difference is stress evaluation and consideration of switching behaviour. A common notion of magnetic stress is used in [78] for evaluating stresses acting on a twin boundary. A twin boundary propagation check and

associated model rebuilding is interconnected with a stress balance equation solved for the twin boundary. This approach, however reasonable this reasoning seems, may not hold since its implementation involves application of L-U model. A modelling approach developed in this study relies on experimental stress-strain-magnetic field curves, so stress calculation can be omitted allowing assessing MSM element's state and actuator performance by analysing the magnetic field solution.

4.3 Application of FEM to modelling non-homogeneous and anisotropic MSM element in actuators

As previously discussed, an approach allowing the modelling of a complete actuator magnetic circuit including the MSM element is needed. This is important since magnetic properties of the MSM element play a significant role in total reluctance of the magnetic circuit. Moreover, MSM permeability changes during the shape change non-linearly which cannot be captured in simplistic models. Use of FEM allows using well-known techniques for representing actuator geometry and material properties including non-linear B-H curves. The MSM element properties which require capturing in order to represent its magnetic behaviour correctly are:

- Change in shape corresponding to a particular strain
- Non-homogeneous multi-variant composition in intermediate states
- Geometry of twin variants, e.g. variant size and twin boundary tilt
- Magnetic anisotropy of twin variants

A modelling approach allowing capturing all of the above effects would be the most accurate and desirable. Such an approach has been developed as part of this study, which is discussed in detail in the next Section. It should be mentioned that other approaches were also considered. However, it is hard to show their limitations unless the most accurate approach is used as a reference. Therefore, the final approach is discussed first along with its application to MSM actuator modelling. Other approaches (being simplified special cases) are discussed afterwards, considering their effects on MSM magnetic field distribution and accuracy of actuator performance evaluation.

4.3.1 MSM element modelling approach

The main features of the developed modelling approach are:

- Real geometry of an MSM element is modelled. MSM element's length increases during elongation along with simultaneous decrease in its width. The opposite is true for contraction.
- Change in shape occurs due to reorientation of twin variants and propagation of twin boundaries. This is reflected in the model by presenting more and more "easy" variants during elongation, or "hard" variants during contraction.
- Variants have particular geometrical features. The smallest width a variant can have is related to "hard" band (a variant between two twin boundaries) width of 0.1mm [37]. "Easy" band width is $1+\varepsilon=1.06$ times bigger yielding 0.106mm width. This implies discretisation of MSM element's length. Sizes of multiple bands with the same magnetic properties are added up and modelled together when not separated by other variant's bands. The distribution of new variants is modelled through allocating "easy" variants equally far from one another, as well as from MSM element's sides. Further elongation leads to reorientation of "hard" variants using similar reasoning.
- Twin boundaries are tilted by 45° with respect to MSM element's sides.
- Due to magnetic anisotropy of **every** variant, **both** "hard" and "easy" B-H curves are assigned to **each** variant: "easy" curve is assigned to an axis coinciding with *c*-axis whereas "hard" curve is assigned to the axis coinciding with *a*-axis of a crystal (as well as to *b*-axis in 3D). Current orientation of axes defines whether a variant is "easy" or "hard".

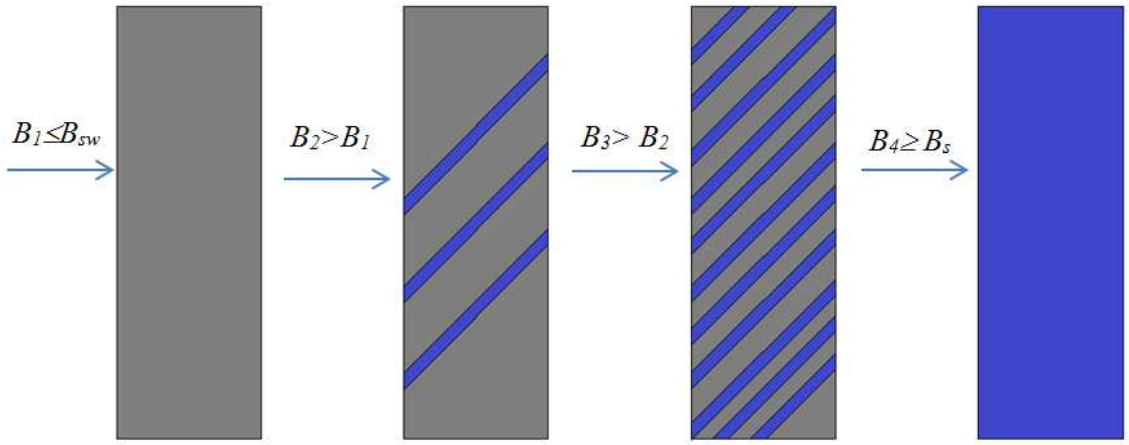

Figure 4.3-1. Change in MSM element's variant composition from fully "hard" (grey) to fully "easy" (blue) with increasing magnetic field

It should be mentioned that distribution of MSM variants' bands is modelled only approximately. However, there is no general rule for determining which twin boundary moves and the process is a rather random one. What is most important, it represents twin distribution in multi-variant MSM crystals with Type I twin boundaries in a most accurate way [20], simultaneously allowing taking into account non-homogeneous nature of a multi-variant state.

Modelling twin boundary tilt is a surprisingly important detail. As shown below, it has one of the most significant effects on magnetic field distribution. Showing this emphasises the necessity of modelling the correct variant geometry. The need to model numerous tilted twin boundaries increases the time required for setting up a model, especially if twin boundaries reach corner regions. One can see that 0.1mm height of a "hard" band implies a maximum of 99 twin boundaries existing simultaneously in the most common 10mm MSM element. However, it is possible to avoid modelling all the boundaries allowing reasonable "clustering" of bands with the same magnetic properties.

The way anisotropy is modelled is one of the most distinct features of the developed approach. As discussed before, other approaches usually consider MSM element anisotropic whereas twin variants are assumed isotropic. However, this point of view produces inconsistencies. Whereas presence of a second axis does not play any

significant role in a single-variant MSM element (see Fig. 4.3-2), it affects the magnetic field distribution for multi-variant MSM elements.

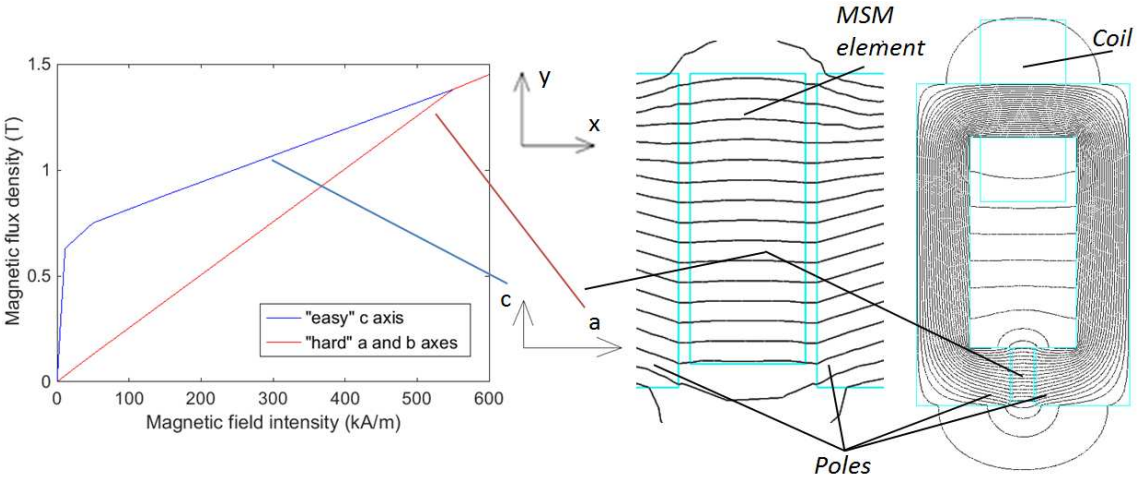

Figure 4.3-2. B-H curves for “hard” and “easy” magnetisation axes in anisotropic single-variant MSM element in 2D model of actuator magnetic circuit

4.3.2 Magnetic field distribution in a multi-variant MSM element

The most obvious effect of choosing a particular way of modelling an MSM element in actuators can be seen by analysing the magnetic field distribution in the MSM element and related demagnetisation effects. A short 2.5mm MSM element is used in all models in this Chapter for clarity of the pictures. Nevertheless, the results obtained hold for any MSM element as long as core poles exceed its length in any state.

Figure 4.3-3 (a) shows the magnetic field lines and (b) flux density distribution in MSM element in actuator’s magnetic circuit. This model includes 1A current / 280 turns coil resulting in considerable mmf sufficient for producing a relatively strong magnetic field. First, it illustrates how the magnetic flux density varies in the MSM element. This non-homogeneity is a consequence of MSM element’s multi-variant state. Whereas plotting flux density vector sum does not provide the most useful information about the magnetic field in anisotropic twin variants, it illustrates the difference in flux density magnitude in “easy” (orange) and “hard” (blue/green) variants. Second, magnetic field lines bend on twin boundaries due to the difference in orientation of magnetic axes in “easy” and “hard” twin variants. This initially may not seem as something important. However, this phenomenon has a significant effect on MSM permeability analysis.

Moreover, bending of field lines implies that a force is acting on the boundary [123]. This is consistent with basic theory since forces produced by twin variants do act on twin boundaries, which eventually are translated into overall force output. Third, the magnetic field is not homogeneous not only in the MSM element, but also in the air gap. Figure 4.3-3 (c) shows an overall decreasing trend of air gap magnetic flux density along the length of the MSM element (measured top to bottom). Moreover, local peaks on the figure correspond to proximity of "easy" variants. Therefore, current composition of MSM element affects the magnetic field distribution in the air gap. One can see that this also implies certain measurement difficulties since experimental results depend on spatial position of the sensor in the air gap. In addition, this effect varies as shape of the MSM element changes, due to the increasing number of "easy" variants. It should be stressed that all these effects occur naturally due to non-homogeneity and magnetic anisotropy of the MSM element. These effects also cannot be modelled if the MSM element is assumed a "black-box" with average magnetic properties.

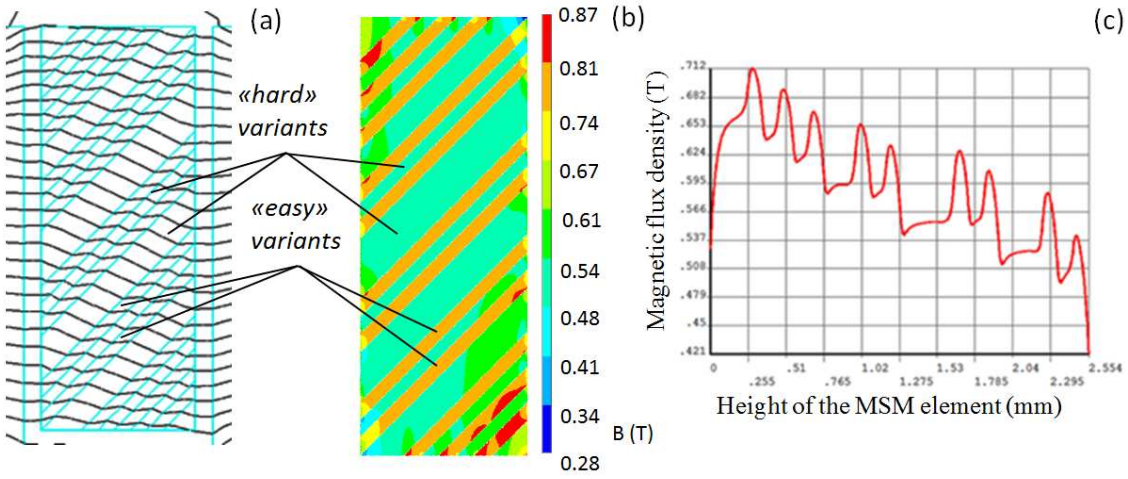

Figure 4.3-3. (a) Magnetic field lines and (b) flux density distribution in the MSM element with fine twins, (c) *x*- component of magnetic flux density in the air gap near the left surface of the MSM element

The modelling results in Fig. 4.3-3 can explain effects that have been reported by researchers conducting experiments involving MSM alloys. It was mentioned before that demagnetisation effects related to MSM element's shape make understanding the magnetic field distribution in the MSM region based on measurement results challenging [121]. Figure 4.3-3 explains this providing evidence for a considerable

difference between the magnetic field in the MSM element and the magnetic field that is measured in the air gap. The significance of demagnetisation and challenges associated with capturing related effects in analytical models have been mentioned numerously e.g. [124], [125]. However, one can see from analysing Fig. 4.3-3 that all these effects can now be studied trough application of an appropriate modelling approach. An important advantage of FEM in application to studying demagnetisation is that no additional assumptions and parameters are required since all effects occur naturally from solving electromagnetic field equations.

However, a much deeper understanding of MSM element's magnetic behaviour arises from analysing a very weak applied magnetic field. For average and strong bias fields, "easy" variants begin saturating which affects the magnetic field distribution. Understanding this is particularly important since MSM actuators currently work in fields sufficiently strong for saturation of "easy" variants to begin. However, it is interesting to see what happens when operating magnetic fields lie in the linear region of "easy" axis' B-H curve.

Figure 4.3-4 illustrates the magnetic field lines in the MSM element in a very weak applied field. The bias field is produced by a 0.1 A current / 280 turns winding yielding one tenth of the mmf used in the previous experiment. This picture explicitly shows that magnetic field lines tend to align with "easy" axis in **each** variant. This is one of the most basic ideas related to MSM theory (see Chapter 2). However, magnetic field distribution pictures obtained before did not clearly show this. In Fig. 4.3-4 field components associated with "hard" axis are so small that almost all flux in a variant aligns with its "easy" axis. On the contrary, field distribution in Fig. 4.3-3 implies that both "easy" and "hard" axes related components affect orientation of magnetic field vectors. This again is due to saturation of "easy" axis. Since saturation does not occur in weak fields, the tendency of alignment of field lines with "easy" axis becomes obvious.

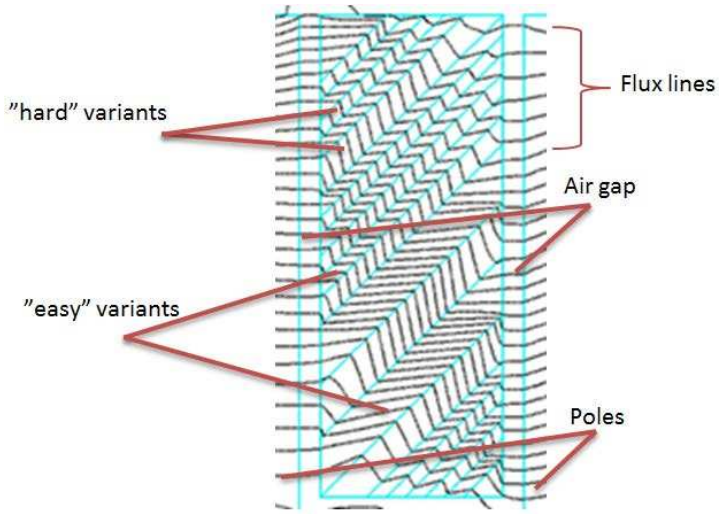

Figure 4.3-4. Magnetic field lines in a multi-variant MSM element in a weak bias magnetic field

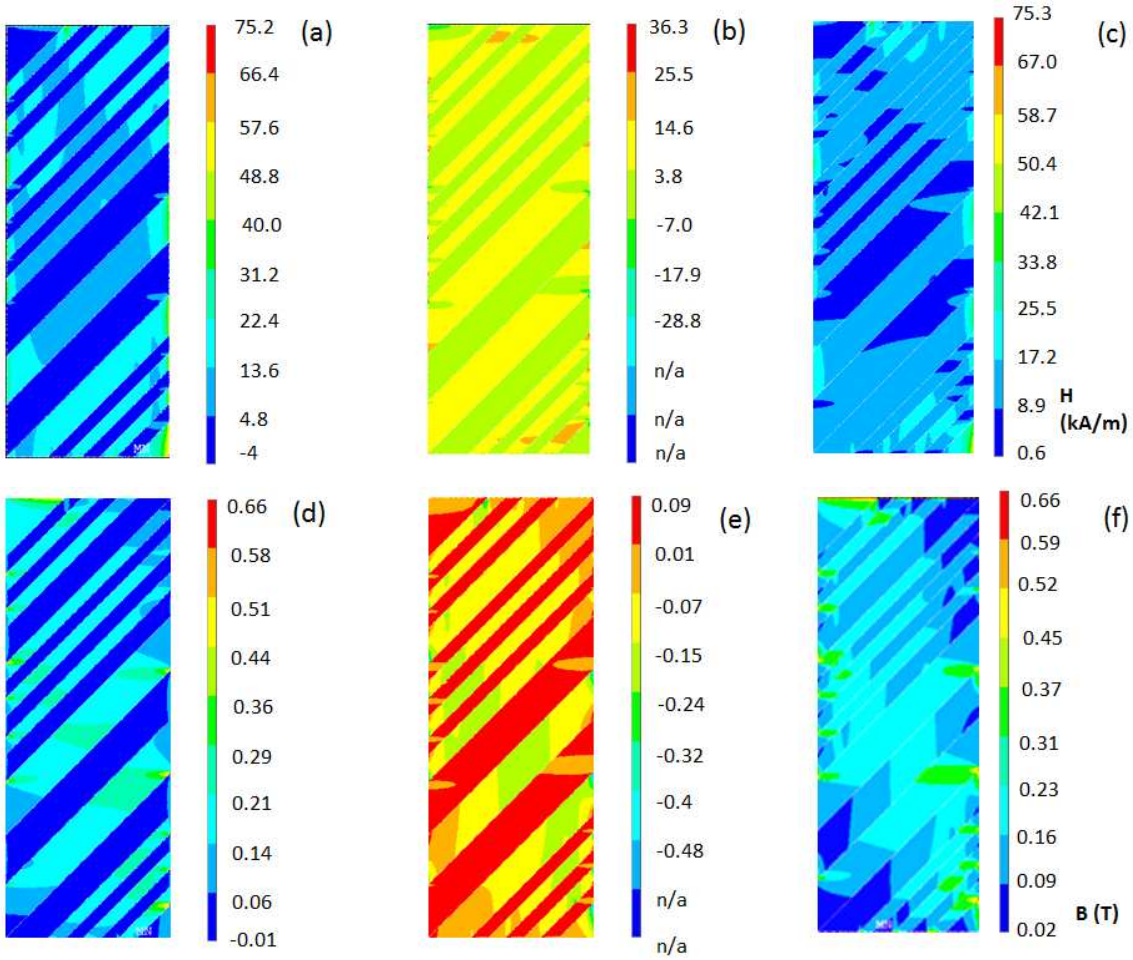

Figure 4.3-5**.** Field solution for a multi-variant MSM element in a weak bias magnetic field, (a) *x*- (b) *y*-components and (c) magnetic field intensity vector sum, (d) *x*- and (e) *y*-components and (f) magnetic flux density vector sum

This result illustrates that magnetic field in MSM element has both *x*- and *y*- spatial components. Figure 4.3-5 shows that *y*-component of the MSM magnetic field can be as big as *x*- component, whereas the applied (air-gap) magnetic field in Fig. 4.3-4 seems to have only *x*- component. Therefore, a reasonable question arises: where does this *y*-component of the magnetic field come from? This question holds regardless of intensity of the applied magnetic field. In order to answer this question, continuity equations should be considered first. These describe the behaviour of magnetic field at any boundary separating areas with different magnetic properties [109], [123]

$$B_{n(1)} = B_{n(2)} \tag{4.3-1}$$

$$H_{\tau(1)} = H_{\tau(2)} \tag{4.3-2}$$

where subscripts *n* and τ stand for normal and tangential components of magnetic field vectors in relation to the boundary separating areas *(1)* and *(2)*. In application to Fig. 4.3-6, this implies that normal component of flux density and tangential component of magnetic field intensity do not change when magnetic field enters the MSM element. Therefore, the following relationship can be written:

$$B_{\delta x} = B_{mx} \tag{4.3-3}$$

$$B_{\delta y} \cdot \mu_m = B_{my} \tag{4.3-4}$$

where B_δ is magnetic flux density in air-gap, T; B_m is magnetic flux density in relevant variant of MSM element, T; μ_m is relative permeability of that twin variant. In order for the flux line to be bent i.e. for field vectors to have both components, both equations should give non-zero solutions. However, $B_{\delta y}$ is zero if the applied field has only *x*-component. This is a very common assumption for MSM magnetic field analysis. However, one can see that such an assumption produces inconsistency since only straight flux lines and, hence homogeneous magnetic field distribution is allowed.

Therefore, the air-gap magnetic field should have both *x*- and *y*- spatial components. When magnetic field is computed using FEM and Maxwell's equations are satisfied, a very small *y*- component of air-gap magnetic field occurs naturally. Table 4.3-1 summarises the results obtained for a point at air-"hard" variant boundary Fig. 4.3-3 equivalent to a problem Fig. 4.3-6. It shows how a very small *y*- component of air-gap magnetic field gives rise to a considerable B_{hy} due to a very large "easy" axis permeability associated with *y*- axis in "hard" variant.

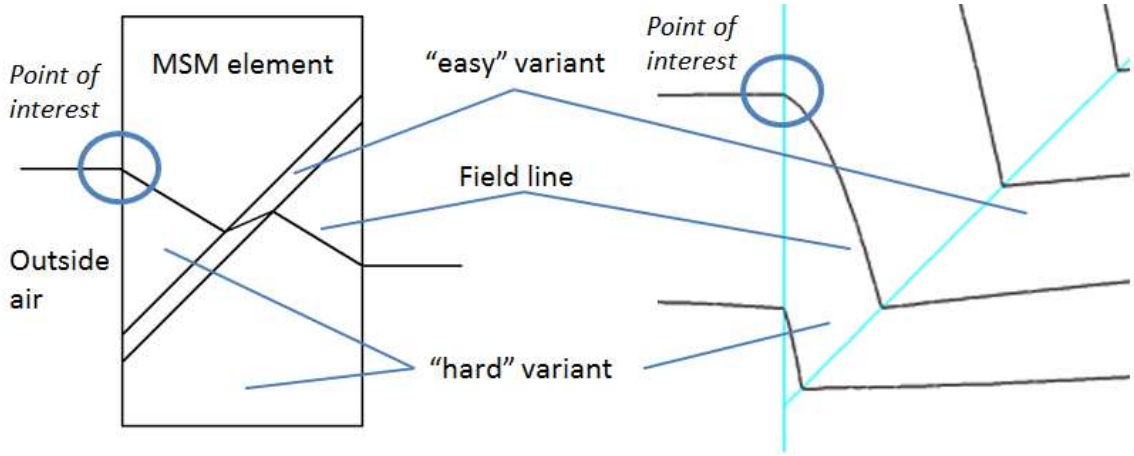

Figure 4.3-6. Behaviour of magnetic field lines entering the MSM element; (a) schematic and (b) FEM representation

Table 4.3-1. Components of magnetic field vectors at air-"hard" variant boundary

Region	B, T	B_x, T	B_y, T	H, kA/m	H_x, kA/m	H_y, kA/m	μ_r	μ_{rx}	μ_{ry}
"hard"	0.3112	0.1003	-0.2946	40.196	39.919	-4.713	6.16	2	50
air-gap	0.1007	0.1006	-0.0059	80.071	80.033	-4.704	1	1	1
		Cont.				*Cont.*			

It is also interesting to apply the same reasoning to the analysis of field lines' bending at MSM twin boundaries. However, n and τ axes do not coincide with *x*- and *y*- axes in this case. In general, a relation between a magnitude of a magnetic field vector, e.g. flux density, and its orthogonal components is

$$B_{tot} = \sqrt{B_x^2 + B_y^2} = \sqrt{B_n^2 + B_\tau^2} \quad (4.3\text{-}5)$$

Therefore, results for *x* and *y* axes obtained from FE solution should be recalculated into n-τ coordinates. This can be done applying simple trigonometry to the problem Fig. 4.3-7. However, the obtained equations (see Appendix 1) depend on mutual orientation of flux lines in "easy" and "hard" variants. Therefore, there is no system of equations which can be applied to any problem regardless of flux lines' orientation. This once again emphasises the importance of FEM application.

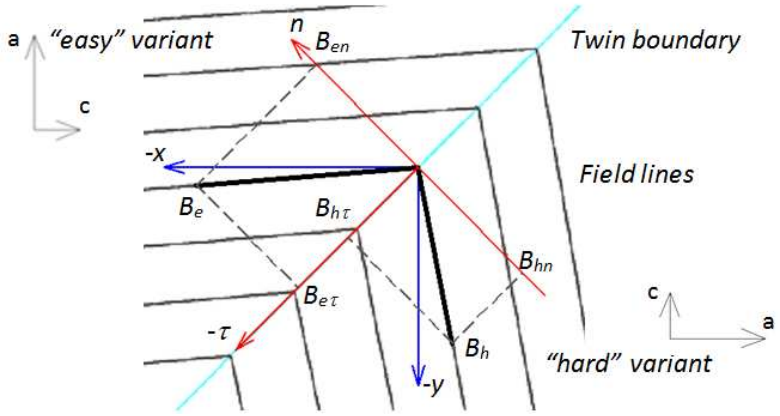

Figure 4.3-7**.** Projections of magnetic flux density vector components in "easy" and "hard" variants on different axes associated with the twin boundary

Table 4.3-2. Components of magnetic field vectors at twin boundary

Region	*B*, T	B_x, T	B_y, T	*H*, kA/m	H_x, kA/m	H_y, kA/m	μ_r	μ_{rx}	μ_{ry}	B_n, T	H_τ, kA/m
"hard"	0.1619	0.0356	-0.1585	13.593	13.355	-2.535	9.5	2	50	0.1358	7.651
"easy"	0.2116	0.2107	0.0187	8.175	3.372	7.447	20.6	50	2	0.1358	7.651
										Cont.	*Cont.*

Table 4.3-2 illustrates how magnetic field vectors change on a twin boundary. Several important aspects of those are worth discussing further. First, magnetic flux density and field intensity vary throughout "easy" and "hard" variants. In is not surprising that flux density vector sum values in "easy" and "hard" variants are close and "easy" variant's flux density is slightly bigger. However, this is actually due to contribution of different

components of field vectors in different variants. For instance, *x*-component contributes mostly to the vector sum in "easy" variants whereas *y*-component is predominant in "hard" variants. This correlates with the orientation of "easy" axes in particular variants. The same reasoning can be used to explain the magnetic field intensity behaviour noting that its value is bigger in "hard" variants. This result is particularly important since it illustrates inapplicability of 1D models which assume a uniform magnetic field distribution in a multi-variant MSM element (e.g. L-U model).

Finally, MSM permeability calculated using total flux density and field intensity differ from "easy" and "hard" axes permeability values. This permeability value is the one that should be used in calculations similar to those discussed in Section 4.2.1. It is important to emphasise that "hard" and "easy" variant relative permeability values in Table 4.3-2 are correct only for this particular problem and are not a simple combination of μ_{rx} and μ_{ry}. It is possible to write an equation for relative MSM permeability in a particular variant, which however becomes extremely hard to work with (see Appendix 1). Magnetic anisotropy of twin variants requires working with magnetic field vector components rather than the vector sum. Hence, a field solution can be used for finding MSM permeability and using it in an equivalent magnetic circuit model, but not vice versa. Due to anisotropic and non-linear properties of MSM twin variants, permeability of an MSM element is unknown even when properties of its axes are known. This is true for MSM elements in multi-variant states. However, there are special cases for which permeability can be evaluated easily. Nevertheless, these results illustrate how complicated MSM magnetic field distribution is, and yet it can be obtained using a relatively small amount of experimental data applying a correct modelling approach.

4.3.2.1 Effects of twin variants' size and distribution

Size and distribution of MSM twin variants is modelled according to experimental data in [37]. However, it is interesting to see how these two parameters affect the magnetic field problem. Table 4.3-3 summarises the results of an experiment conducted using a model with 0.72% strained MSM element. Normally, this corresponds to three 0.106mm "easy" variants. Size of "easy" variants was altered in the experiment resulting in bigger number of smaller variants contributing to the same total volume. The parameter of interest is air-gap flux density.

Table 4.3-3. Change in air gap flux density with number and size of “easy” bands

Number/size of twin variants	3/1	6/0.5	12/0.25	18/0.17
B_δ	0.538	0.538	0.538	0.537

One can see that these results are identical. However, smaller size of variants leads to meshing complications since very fine elements are needed. Therefore, it is reasonable to use 0.106mm size for “easy” variants from both modelling and experimental points of view.

Next, an effect of distribution is studied. An MSM element at 1.44% strain is used in this experiment. This implies 24% of its volume being accommodated by “easy” variants normally resulting in 6 “easy” bands. The experiment studies several possible arrangements: keeping all 6 variants close resulting in very non-uniform distribution throughout the MSM element; placing variants in two sets of 3 variants, and three sets of 2. 3’ corresponds to two variants being close, whereas the third one is placed further away from those. Finally, a usual model with 6 variants evenly distributed throughout the MSM element is used as a reference.

Table 4.3-4. Change in air gap flux density with distribution of “easy” bands

Distribution	1	2	3	3’	6
B_δ	0.563	0.564	0.566	0.567	0.569

Table 4.3-4 summarises the results. Again, no significant variation is found. The increasing trend is too small to be worth considering. Therefore, variant distribution can be chosen so its effect on mesh complexity is minimised. Also, geometry of MSM twin variants can become more complicated if twin bands are very close to corners of MSM element. Therefore, these arrangements can safely be avoided.

The results show that size and distribution of twin variants do not affect average air-gap flux density. This implies that for actuator design purposes these parameters can be chosen considering FE mesh and effects on time required to set up a model using particular software, rather than physics of the MSM shape change. Therefore, this

presents an opportunity to simplify the modelling approach. However, there is an obvious effect on the magnetic field distribution inside the MSM element. Therefore, a complete modelling approach should be used in order to capture MSM magnetic field distribution accurately. It should be mentioned that the development of simplified models was not part of this study and, hence a complete model that includes distributing fine twins of appropriate size throughout the MSM element was used.

4.3.2.2 Single- and two-variant states of MSM element

Whereas multi-variant state is attributed to MSM elements which are currently experiencing shape change, single-variant state occurs when MSM element is fully contracted or elongated. These extreme cases are actually much simpler from perspective of modelling and magnetic field distribution evaluation. It is obvious that in a single-variant state no twin boundaries are present and, hence the magnetic field distribution is rather homogeneous. It also depends on properties of only one twin variant. Finally, variant anisotropy does not have such a significant effect on the field distribution here. A single-variant MSM element can essentially be modelled as a single element in magnetic circuit, which is not true for multi-variant states.

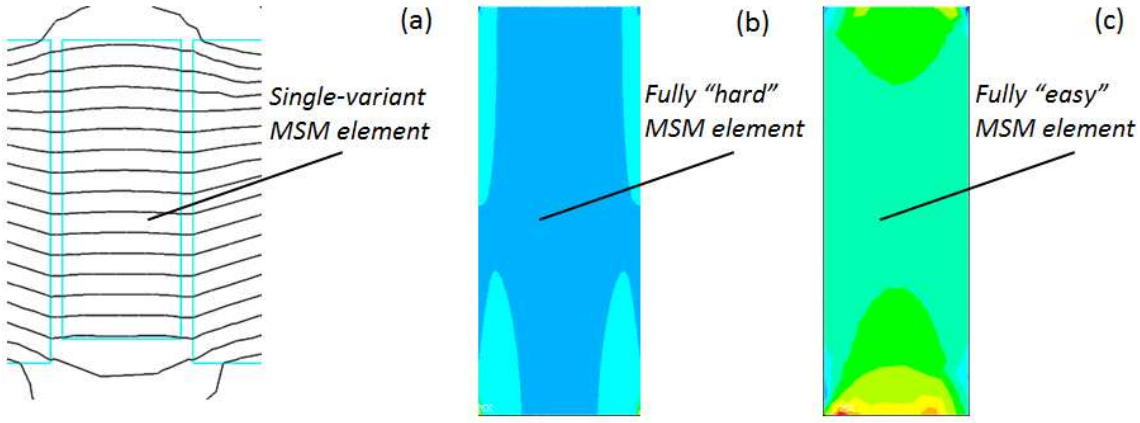

Figure 4.3-8. (a) Magnetic field lines in a single-variant MSM element, (b) "hard" and (c) "easy" variants' flux density distribution

Figure 4.3-8 illustrates magnetic field lines and flux density distribution in a single-variant MSM element. Results in Fig. 4.3-8 (b) and (c) are obviously obtained from different models. As one can expect, magnetic field lines are almost parallel and do not

bend. Nevertheless, slight non-homogeneity is still present due to anisotropy of MSM twin variants. Difference in patterns Fig. 4.3-8 (b) and (c) is due to different orientation of crystallographic axes in “hard” and “easy” variants. Therefore, it is important to take anisotropy into account when it is critical to model MSM magnetic field distribution accurately. However, effects of variant anisotropy on air-gap magnetic field distribution are negligible in a single-variant MSM element. This allows simplifying a model when air-gap magnetic field is used to evaluate MSM actuator performance.

Modelling both multi- and single-variant states of MSM element leads to covering the whole range of possible shapes. However, another possible state has also been reported. It is often attributed to Twin II rather than Twin I MSM crystals since the latter tend to have multiple twin boundaries in intermediate states. In case of Twin II crystals, a single highly mobile Type II twin boundary tend to occur at one side of the specimen which travels along its length causing variants to reorient resulting in overall shape change. Whereas this topic was discussed previously in Chapter 2, interesting effects on magnetic field distribution occur when only a single twin boundary is present.

Figure 4.3-9 shows the magnetic field distribution in a two-variant MSM element in a rather strong bias field. This picture is remarkably different from those observed for multi-variant states. The difference in magnetic flux density becomes much more apparent varying from 0.4T in “hard” (blue in Fig. 4.3-9 (a)) to 0.8T (orange) in “easy” variants. Moreover, the magnetic field of each variant becomes much more non-homogeneous. Whereas overall non-homogeneity was observed in a multi-variant state, the magnetic field was relatively homogeneous for each particular variant. However, both overall and local magnetic field distribution patterns are very non-homogeneous for an MSM element in a two-variant state.

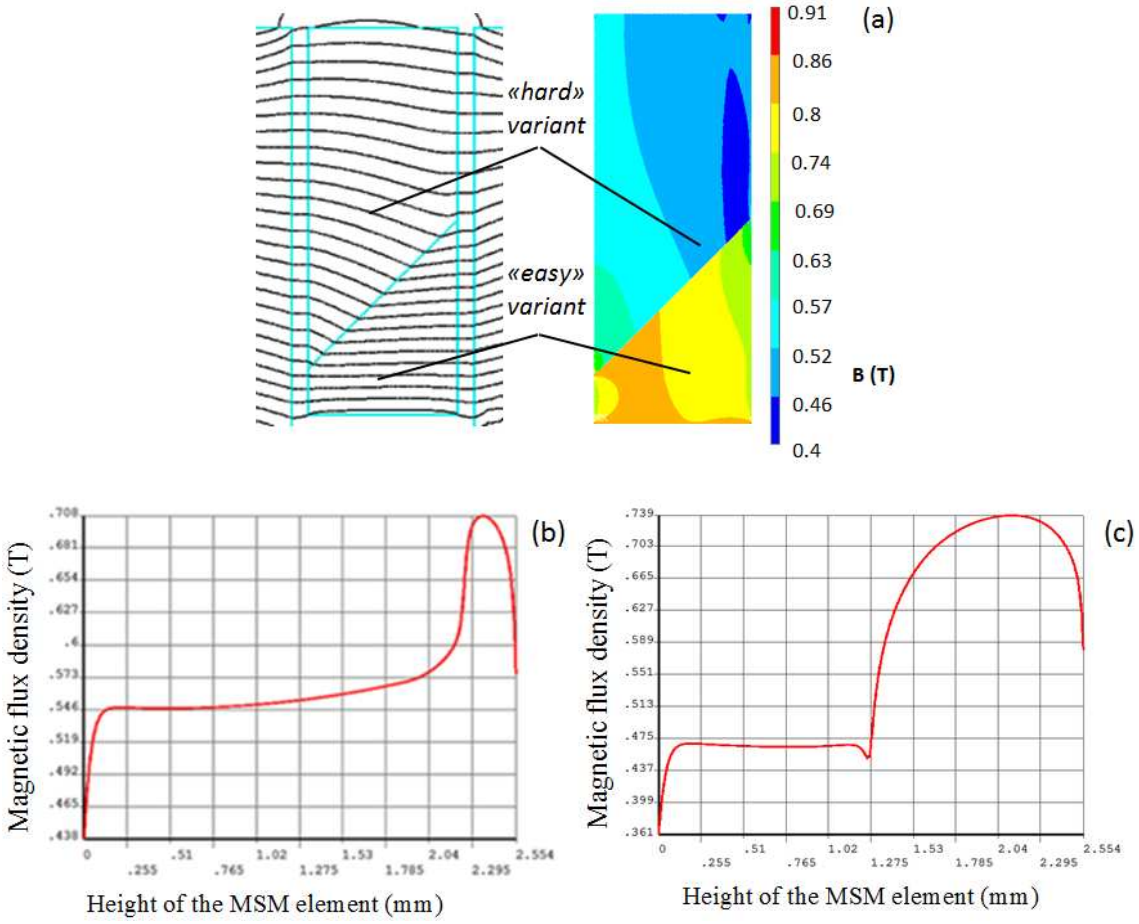

Figure 4.3-9. (a) Magnetic field lines and flux density distribution in the MSM element with a single twin boundary, and *x*- component of magnetic flux density calculated in the air gap near (b) left and (c) right surface of the MSM element

This also implies that the force acting on a twin boundary varies along twin boundary's length. In addition, the effects of MSM varying permeability on the bias field become even more obvious. Here, the magnetic flux density in air gap calculated near left side of the MSM element (see Fig. 4.3-9 (b)) changes rapidly from 0.55 to 0.7T. This once again illustrates how position of a Hall sensor can affect the measurement results. One can also see that results differ depending on which side of MSM element is chosen for measurement. However, average values of flux density are essentially the same: 0.572T for (b) and 0.579T for (c). This result suggests that average air-gap flux density is the most suitable parameter for analysing mutual interaction between the MSM element and actuator magnetic circuit. On the other hand, local effects related to MSM magnetic field distribution can only be analysed considering variation of magnetic field vectors throughout the volume of MSM element.

The results summarised in this Section show how this modelling approach can be used as an additional tool for studying Type II TB mobility. The difference in mobility of Type I and Type II TBs is commonly attributed to the difference in twinning stress. However, the difference in magnetic field distribution can affect magnetic field-induced stress when Twin II MSM elements are operated by magnetic fields.

4.3.2.3 Limitations of equivalent electric circuit approach

Previous Sections show very non-uniform magnetic field distribution in the MSM element. Moreover, it has been shown that permeability of MSM element cannot be easily evaluated analytically. Therefore, the applicability of the simplistic equivalent electric circuit approach becomes questionable. First, equivalent electric circuit representation requires fluxes to be homogeneous in every element of the circuit. This implies either a very large number of elements (reluctances) required for representing the problem correctly or neglecting particular aspects of the magnetic field distribution. The former can require enormous amount work to be done considering non-linear magnetic properties of MSM twin variants, which nullifies the main advantage of the approach – its simplicity. Therefore, it is important to see how different is a picture one can get using equivalent magnetic circuit approach comparing to the accurate FEM magnetic field solution.

Two types of connection between reluctances are possible: series and parallel. Both types allow representing MSM element with a single reluctance with average permeability using known rules. However, it is not clear which one can represent the real connection of MSM twin variants accurately. This question was studied in [22] where average MSM permeability based on series and parallel connection of variants were deduced as

$$\mu_{m.series} = \frac{\mu_h \cdot \mu_e}{\mu_e + \varepsilon \cdot (\mu_h - \mu_e)} \tag{4.3-6}$$

$$\mu_{m.parallel} = \mu_h + \varepsilon \cdot (\mu_e - \mu_h) \tag{4.3-7}$$

It is worth noting that Eq. (4.3-7) is equivalent to MSM permeability averaged along the length of MSM element. However, no agreement with the experiment was found in [22]. It is possible to explain this now by using magnetic field distribution pictures obtained in this study. Whereas actual magnetic field is very non-homogeneous, the parallel connection of elements corresponds to magnetic field lines passing through either “hard” or “easy” variants. This also yields that magnetic field intensity H is the same in both types of variants. However, the previously discussed results show that these conditions are not satisfied. On the contrary, each field line is passing through both “easy” and “hard” variants suggesting that variants are connected in series. However, results in [22] show that series connection of elements does not represent the real phenomenon correctly either. The reason for this is that the magnetic field lines bend at twin boundaries due to anisotropy of MSM twin variants. Hence, neither parallel nor series connection of variants can represent the real magnetic field distribution correctly.

It is remarkable that the 45° tilt of twin boundaries is the main reason for the inapplicability of equivalent electric circuit models to multi-variant MSM regions. The magnetic field distribution in an imaginary MSM element with horizontal twin boundaries Fig. 4.3-10 (a) can be approximated by parallel connection of elements since field lines are passing through either “hard” or “easy” variants. This illustrates the significant effect of the twin boundary tilt on the magnetic field distribution. However, it is still possible to represent a single-variant MSM element as a single reluctance with very high accuracy. Similarly, a sufficiently strong magnetic field can saturate “easy” variants in a blocked MSM element resulting in field lines aligning with the bias field, as shown in Fig. 4.3-10 (b). However, it is still necessary to take “easy” variants’ saturation into account in order to find the equivalent MSM permeability accurately.

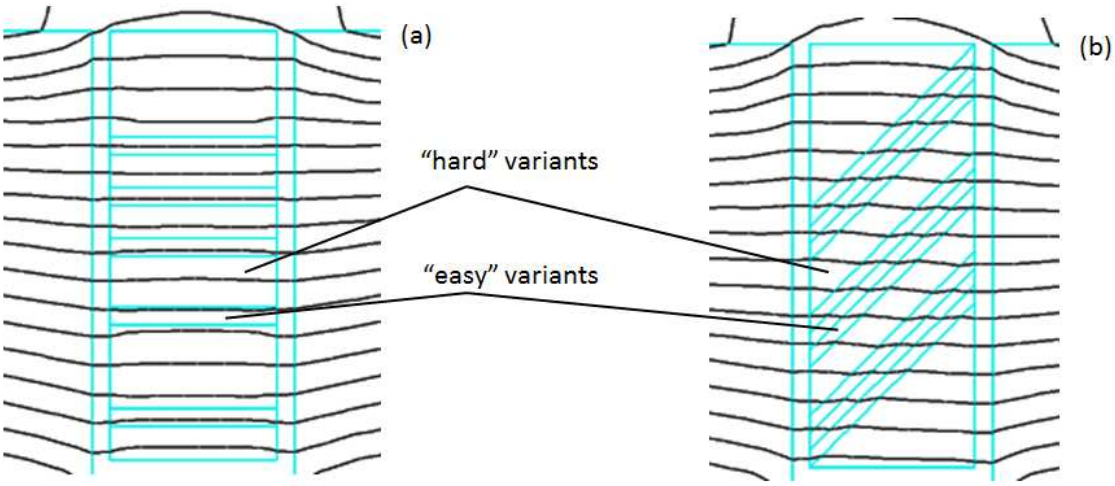

Figure 4.3-10. Magnetic field lines in MSM elements with (a) horizontal twin boundaries in a weak magnetic field and (b) tilted twin boundaries in a strong magnetic field

However, the magnetic field distribution in Fig. 4.3-10 (a) is still very non-homogeneous. The air-gap magnetic flux density varies along the length of MSM element increasing in vicinity of "easy" variants due to their larger magnetisation. Figure 4.3-11 shows this clearer. This result has an interesting effect on equivalent magnetic circuit representation.

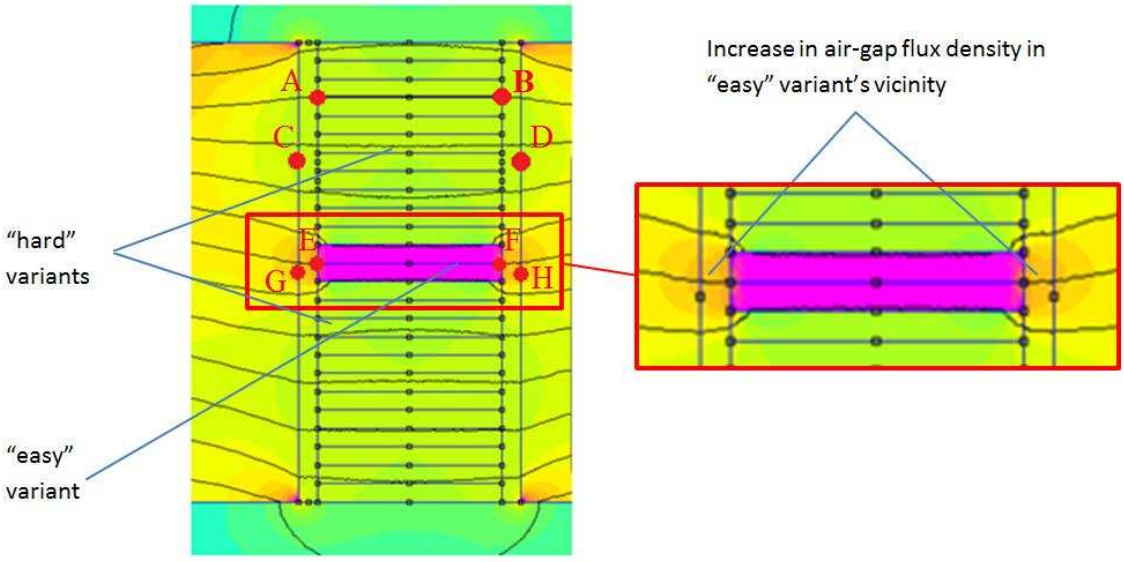

Figure 4.3-11. Magnetic flux density distribution in imaginary MSM element with horizontal twin boundaries

Magnetic field intensity varies in “easy” and “hard” variants due to demagnetisation effects. This implies different mmf drop along different variants. For instance, $F_{AB} \neq F_{EF}$ in Fig. 4.3-11. Therefore, those cannot be represented by parallel connection of reluctances since 2nd Kirchhoff’s law does not apply. However, it holds for the complete air-gap that includes MSM and air regions, $F_{CD} = F_{GH}$. Therefore, the correct equivalent magnetic circuit representation of MSM actuator’s air-gap is shown in Fig. 4.3-12.

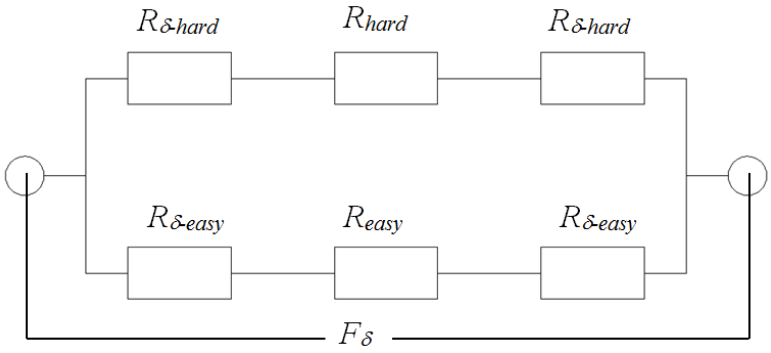

Figure 4.3-12. Equivalent electric circuit representation of actuator’s air gap with parallel connection of “easy” and “hard” branches, where air gap reluctances depend on size of adjacent MSM variants

This discussion may seem irrelevant since MSM twin boundaries are not horizontal in reality. However, the result that mmf drop should be calculated along the whole air-gap has a very important application in the next Section.

4.3.3 Validation of the proposed approach

The inductance measurement results published by Suorsa *et al.* in [22] are used in order to validate the proposed approach. Those results show that neither parallel nor series connection of twin variants can predict the behaviour of varying MSM permeability, which translates into inductance measured experimentally. The reason for such behaviour has not been discovered. However, this result correlates with the discussion in Section 4.3.2, since the measured inductance also depends on permeability of the MSM element. In this Section we use FEM for modelling the same measurement setup in order to determine whether the reported change in inductance can be explained using the approach proposed in this study.

A FE model of the magnetic circuit is used for calculating the magnetic field distribution in air-gap and MSM regions. However, it does not allow evaluating relative permeability of the MSM element directly. FE analysis provides results for particular MSM variants, whereas actual measurement treats MSM element as a single object. Therefore, an equivalent electric circuit model of the measurement setup is also used for evaluating average MSM permeability based on additional data obtained from FE analysis. MSM element is represented by a single reluctance in a circuit model and its properties are represented by an equivalent relative permeability as if it is a single object neglecting the twinned microstructure. Due to simplicity of the obtained magnetic circuit Fig. 4.3-13 (a), it is possible to find a reluctance that allows obtaining the same solution in both FE and equivalent circuit models. An equivalent MSM permeability can be then derived from it. This allows comparing experimental data with modelling results. It should be stressed that whereas application of the circuit model requires MSM element to be in a single-variant state, its twinned microstructure is modelled explicitly in the FE model using the discussed approach.

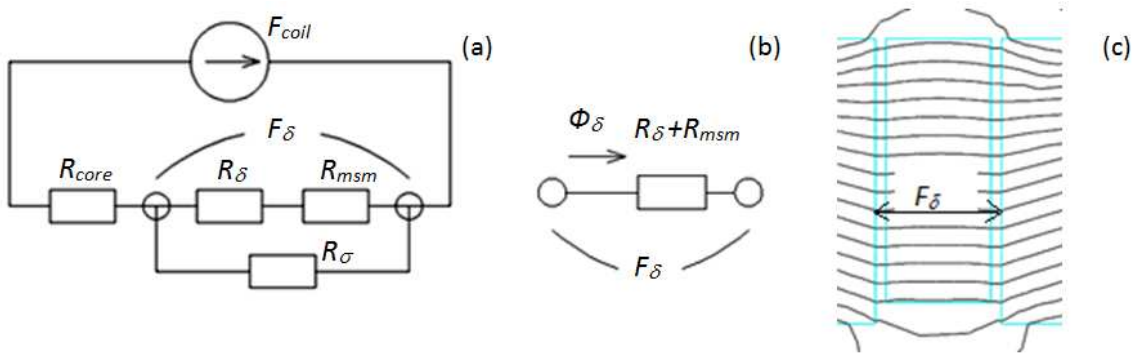

Figure 4.3-13**.** An equivalent electric circuit of magnetic circuit used in the experimental setup [22]. (a) Representation of the complete circuit, (b) its air gap region with the MSM element and (c) corresponding air gap region in a FE model

Equations for an equivalent electric circuit Fig. 4.3-13 (b) can be written as

$$F_\delta = \sum_{\delta} H_\delta \cdot \delta + \sum_{a_m} H_{msm} \cdot a_m \tag{4.3-8}$$

$$\Phi_\delta = \frac{F_\delta}{R_\delta + R_{msm}} \tag{4.3-9}$$

$$R_\delta = \frac{\delta + a_m \cdot \varepsilon}{\mu_0 \cdot A_\delta} \tag{4.3-10}$$

$$R_{msm} = \frac{a_m \cdot (1 - \varepsilon)}{\mu_0 \cdot \mu_m \cdot A_{mt}} \tag{4.3-11}$$

where F_δ is mmf drop along the air gap length, A, H_δ and H_{msm} are magnetic field intensities in air-gap and MSM regions, A/m, δ is total width of air gaps between the MSM element and the poles, m, a_m is width of the MSM element, m, R_δ is air gap reluctance, 1/H; R_{msm} is reluctance of the MSM element, 1/H, μ_m is equivalent relative permeability of the MSM element, A_δ and A_{mt} are air gap and MSM element cross section areas normal to the magnetic flux, m^2. Through rearranging Eq. (4.3-8 – 11) with respect to strain dependent MSM permeability, the final equation is

$$\mu_m = \frac{B_\delta \cdot a_m \cdot (1 - \varepsilon)}{F_\delta \cdot \mu_0 - B_\delta \cdot (\delta + a_m \cdot \varepsilon)} \tag{4.3-12}$$

where B_δ is average magnetic flux density in the air gap near the surface of the MSM element, T. The air gap width at zero strain is 0.2mm in the studied magnetic circuit. It should be stressed that this approach requires no assumptions about the magnetic connection of variants made beforehand. Whereas H_δ and H_{msm} actually vary depending on particular MSM element composition, the overall air gap mmf drop always stays the same, as shown in the previous Section.

In order to replicate the experiment conducted in [22], the input current was kept constant whereas strain (i.e. shape and variant composition) of the MSM element was changing. B_δ and F_δ calculated using FE solution were used as input data for Eq. (4.3-12) along with geometric parameters of the air gap and MSM element (see Appendix 2).

Figure 4.3-14 shows how calculated equivalent relative MSM permeability varies with strain of the MSM element. The changes in MSM permeability predicted by series and parallel connection of twin variants calculated using Eq. (4.3-6 – 7) are also plotted for reference. The curve corresponding to equivalent MSM permeability lies between the curves corresponding so series and parallel connection of twin variants exhibiting strong non-linear behaviour. It should be stressed that this result holds for weak fields where "easy" variants are not saturated. Since "easy" axis permeability decreases in stronger fields, all three curves will tend to get closer to horizontal axis. Nevertheless, the general trend of the curves Fig. 4.3-14 is the same even in strong magnetic fields.

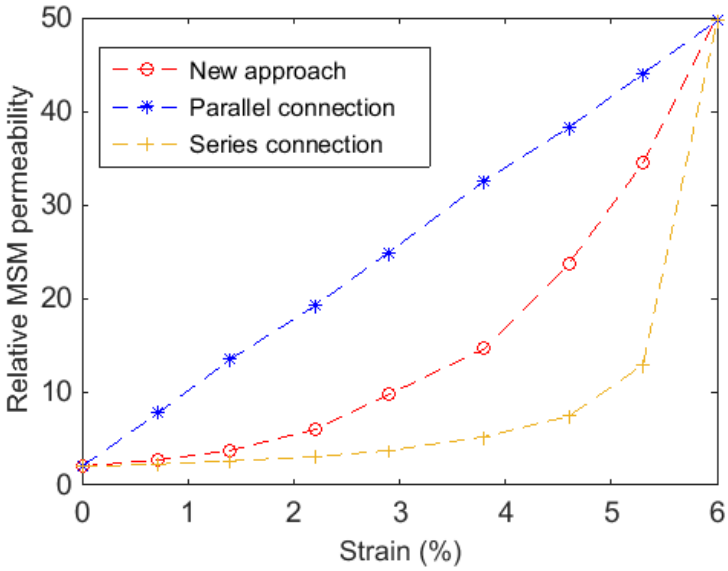

Figure 4.3-14**.** Change in equivalent relative permeability of the MSM element

Finally, the inductance of the coil calculated using modelling results is compared with the measurement results in [22]. Equation (4.3-13) allows calculating the coil inductance as function of strain of the MSM element as

$$L = L_\sigma + {N_c}^2 \cdot \mu_0 \cdot A_m \frac{\mu_m}{a_m + \mu_m \cdot \delta + (\mu_m - 1) a_m \cdot \varepsilon} \qquad (4.3\text{-}13)$$

where L_σ is leakage inductance, H. In order to verify the approach, Eq. (4.3-13) is solved using the data listed in external Table 1 in [22] and relative MSM permeability obtained in this study. The results are shown in Fig. 4.3-15 (a). Curves calculated in

assumption of parallel and series connection of MSM twin variants are also plotted for reference. It should be noted that the leakage inductance L_σ is used only for calibrating zero point of these curves. The behaviour of the curve obtained using the proposed modelling approach is very similar to the behaviour of the experimental curve measured in [22] and shown in Fig. 4.3-15 (b). It should be mentioned that "linear" and "non-linear" models in Fig. 4.3-15 (b) respectively correspond to parallel and series connections of elements in Fig. 4.3-15 (a), and the slight difference between the curves is due to the difference in chosen values of "easy" axis relative permeability. The overall similarity proves that the proposed approach can be used for predicting the reported change in inductance and, hence correctly models varying MSM permeability allowing its quantitative estimation essential for actuator and sensor design.

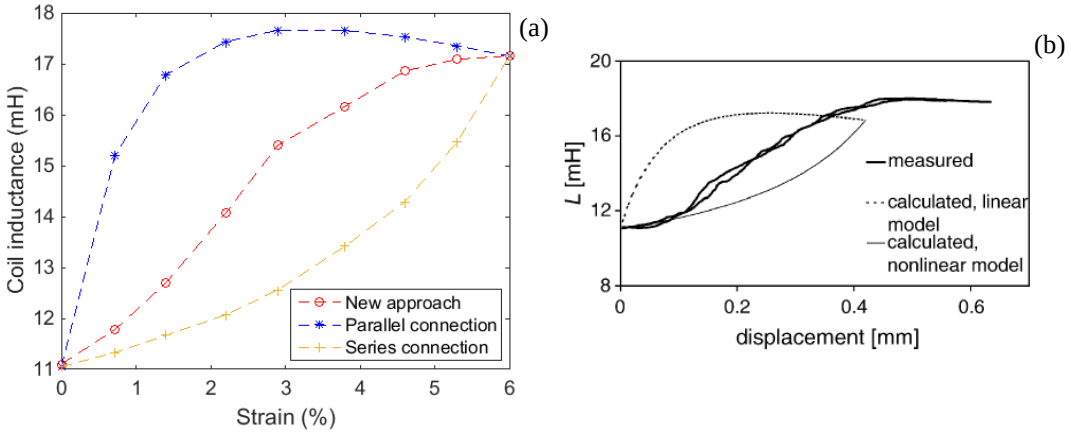

Figure 4.3-15**.** Change in coil inductance due to change in strain of the MSM element (a) calculated using FEA and (b) measured in [22] (reprinted with permission)

Whereas 2D models were used in this study primarily due to the opportunity to plot flux lines, the proposed modelling approach is perfectly applicable in 3D. Since *b* axis is essentially another "hard" magnetisation axis, it can be treated the same way as *a* axis in the model. However, no difference in the behaviour of the MSM permeability in 3D can be expected as long as the magnetic field is applied either transversally or longitudinally to the MSM element. This allows using the proposed approach for MSM actuator design discussed in Chapter 5.

4.3.4 Difference in permeability change in weak and strong fields

The discussion in the previous Section is the most accurate and general representation of MSM permeability change. It is fundamental for the proposed approach which can be applied to modelling any macroscopic MSM behaviour. However, many MSM applications involve use of magnetic fields strong enough to lead to "easy" variants' saturation, which obviously affects its permeability. This is particularly important for large-force actuators. Therefore, it is interesting to see how big the permeability change is in these cases.

Figure 4.3-16 illustrates the equivalent MSM permeability change in extremely strong magnetic field. Saturation of "easy" variants is evident considering that the maximum relative MSM permeability has decreased from 50 to 4.4. Therefore, the effects of permeability change are much less apparent in stronger fields and do not have as much impact on actuator performance. However, the general trend of curves Fig. 4.3-16 is the same as in Fig. 4.3-14. The permeability change is still a non-linear function of strain and its accurate calculation requires FEM modelling, particularly due to the necessity to take into account non-linearity of "easy" axis' magnetic properties.

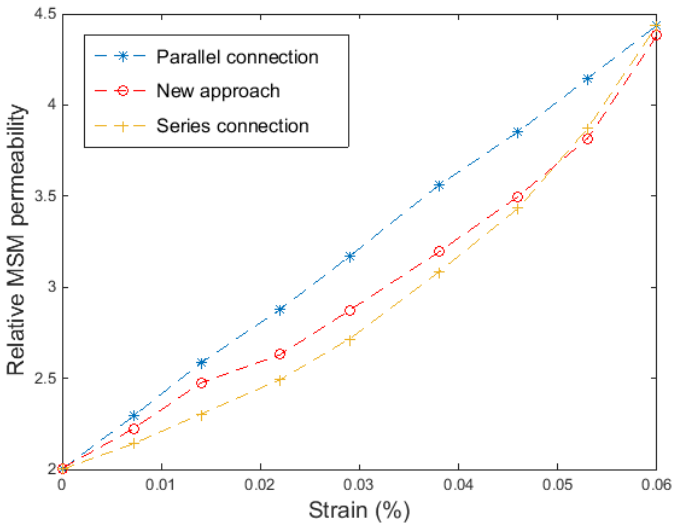

Figure 4.3-16. MSM permeability change in a strong magnetic field

Whereas a very rough estimation of effects of varying MSM permeability on magnetic field in actuators is shown in Section 4.2.1, it is now possible to quantify these effects

much more accurately using this modelling approach. Figure 4.3-17 shows change in flux density in MSM actuator air-gap given constant input current and varying strain of the MSM element. A ratio of flux density at current strain B_d to flux density at zero strain B_{dsw} is chosen for comparison of the effects in weak and strong magnetic fields. This is done by using 0.1 and 1 A input current in the same 280 turns coil.

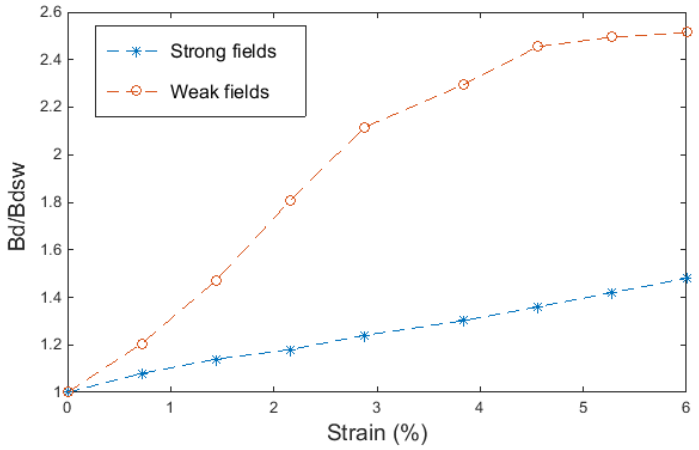

Figure 4.3-17. Relative change in air-gap flux density due to MSM shape change

Figure 4.3-17 shows a significant change in air-gap flux density. The ratio exceeds 2.5 for weak fields. However, it still reaches 1.5 for strong fields. As discussed before, this difference is due to saturation of "easy" variants. Nevertheless, this result shows how important it is to take varying MSM permeability into account in order to predict MSM actuator performance in the most accurate way.

However, the effects of permeability change on actuator design can be illustrated most effectively by comparing modelling approaches that do and do not take permeably change into account. Figure 4.3-18 and 4.3-19 show output of two actuators designed for working on 0.5MPa and 2.5MPa load curves (see Chapter 5 for details). The former corresponds to average magnetic fields, whereas the latter corresponds to the strongest magnetic fields MSM element can work in. These characteristics illustrate the difference in required mmf calculated assuming either constant (minimum) or varying MSM permeability. The significant effect is seen in Fig. 4.3-18 due to a considerable change in MSM permeability. This illustrates the importance of taking MSM permeability change into account – failure to do so results in much larger required mmf

predicted by the model. However, this difference becomes much less important for 2.5MPa load. Here, the mmf calculated using the most accurate approach is slightly smaller than the one calculated using the most simplistic one. This may imply that permeability change can be neglected for large-force actuators. However, the actuators designed as part of this study work on 2MPa load curves for which the permeability change is much bigger than in case Fig. 4.3-19. Hence, it is still crucial to take permeability change into account since actual saturation conditions are not known beforehand.

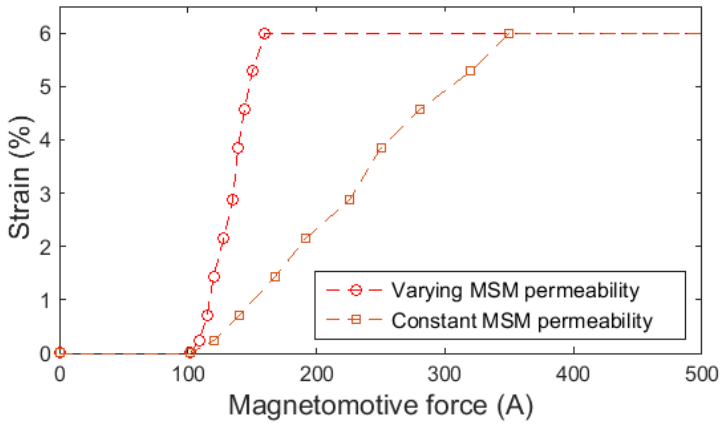

Figure 4.3-18. Actuator output (elongation) calculated using constant and varying MSM permeability for 0.5 MPa load

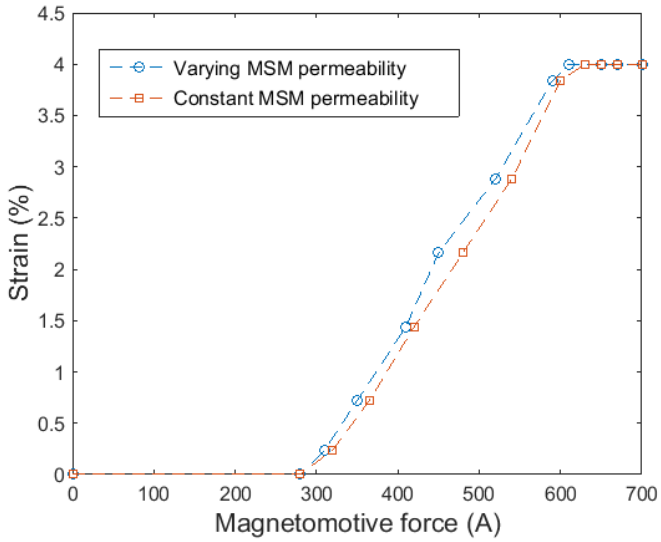

Figure 4.3-19. Actuator output (elongation) calculated using constant and varying MSM permeability for 2.5 MPa load

4.3.5 Permeability change due to mechanical contraction

Permeability of MSM element is related to its variant composition and, hence to its shape. Since shape change can also be induced mechanically, MSM permeability does indeed change during the shape restoring phase initiated by the mechanical spring. This effect is actually related to Villari effect discussed in Chapter 2. Therefore, the proposed approach can also be used for modelling behaviour of MSM sensors and energy harvesters. Its effect on sensor performance evaluation is even more important since magnetisation change phenomenon is in heart of these applications.

However, permeability change during contraction also has an effect on actuator magnetic circuit. MSM permeability increases during elongation leading to increase in total flux for a given coil current. On the contrary, MSM permeability decreases during contraction leading to lower magnetic flux and lower magnetic-field induced stress produced by the current. Therefore, input current should be adjusted for maintaining hold and stand-by positions (see Section 5.3). Thus, accurate modelling of MSM permeability change during contraction is still important for computing the complete actuator strain-current curves and designing the control circuitry correctly.

4.4 Magnetic field-induced stress calculation

It was mentioned on several occasions in previous Chapters that no complete model for actuator output force evaluation is currently available. The most known model used for calculating magnetic stress is L-U model discussed in Section 4.2.1. The L-U model attributes the magnetic stress produced by the MSM element to the magnetic energy difference between “easy” and “hard” variants due to magnetic anisotropy. This can be conveniently illustrated by the area between their magnetisation curves Fig. 4.4-1 (a). This energy is converted into mechanical work (elongation) when “hard” variants reorient into “easy” ones. Equation (2.1-3) showed mathematical representation of this assumption. However, one can see that Eq. (2.1-3) is applicable only when magnetic field intensity H is the same in “easy” and “hard” variants. This is the case since L-U model does not consider magnetic field distribution inside the MSM element. Moreover, the magnetic field intensity outside and inside the MSM element is also the same. Hence, the demagnetisation effects are neglected. However, the field analysis results

discussed in this Chapter show that these assumptions produce a very rough representation of real phenomena. It is easy to see that magnetic field intensity outside the MSM element is at least twice the maximum "hard" variant field intensity. Fig. 4.4-1 (b) shows that B_e and B_h do not necessarily correlate as L-U model expects them to. Moreover, those points do not even lie on B-H curves which guide only their *a*-*c* (hence, *x*-*y*) components. This result is another illustration of a more general discussion presented in Section 4.3.2. Therefore, it is impossible to rely on a simplistic 1D model when stresses in intermediate states of MSM element are calculated.

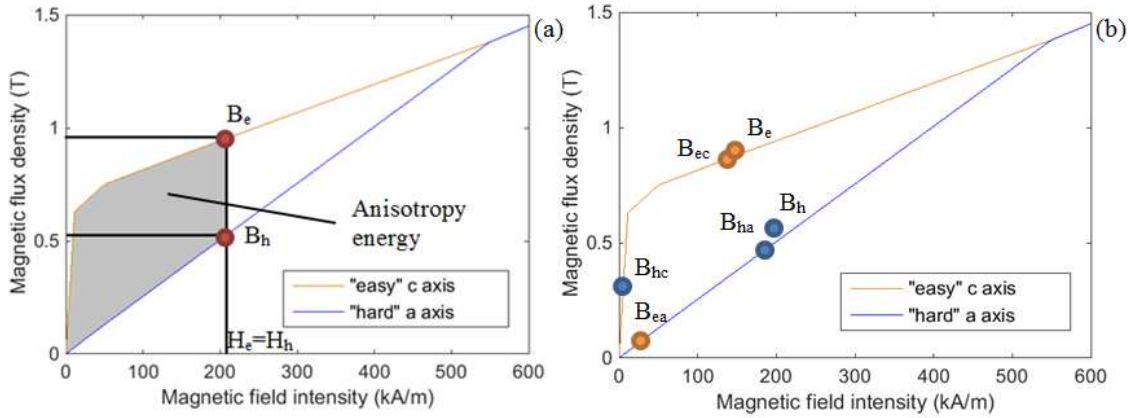

Figure 4.4-1. Projection of magnetic flux density components onto MSM element's B-H curves in (a) L-U and (b) current models

Moreover, application of L-U model can lead to significant miscalculations when MSM actuator output force is calculated. For instance, this is illustrated in [23] where output force produced by fully "easy" MSM element exceeds that of a fully "hard" one. This is fundamentally incorrect since "easy" variants have no further reorientation potential and, hence produce no force [126]. Neglecting MSM permeability change also leads to misleading results obtained in the same work, as well as in [84]. Therefore, there is still a need for a new model for calculating magnetic field-induced stresses which translates into MSM output force crucial for MSM actuator design and performance evaluation.

Such model is yet to be developed. The results discussed in this Chapter and particularly those in Section 4.3.2 provide an important insight on how magnetic forces are induced in the MSM element in actuators. First, modelling variant anisotropy explicitly allows showing that different variants have different potential for reorientation in transversal

and longitudinal fields. Other models lack this property and prohibit consideration of longitudinal fields. However, it has been shown that even a homogeneous transversely applied magnetic field results in a complicated non-homogeneous magnetic field distribution inside the MSM element due to anisotropy of its variants. This implies that magnetic field vectors B and H have both x and y spatial components, which is mathematically identical to the presence of both transversal and longitudinal fields. Hence, additional compressive stresses will be induced in a multi-variant MSM element even by a transversely applied bias field. This statement can be mathematically expressed as

$$\sigma_{mag}(B) = \sigma_{mt}(B) - \sigma_{mc}(B) \tag{4.4-1}$$

$$\begin{cases} \sigma_{mt}(B) = \dfrac{1}{\varepsilon_0}\displaystyle\int (B_{ec}(H_{ec}) - \big(B_{ha}(H_{ha})\big)dH, B \le B_s \\ \sigma_{mt}(B) = 0, B \ge B_s \end{cases} \tag{4.4-2}$$

$$\begin{cases} \sigma_{mc}(B) = \dfrac{1}{\varepsilon_0}\displaystyle\int (B_{hc}(H_{hc}) - \big(B_{ea}(H_{ea})\big)dH, B \le B_s \\ \sigma_{mc}(B) = 0, B \ge B_s \end{cases} \tag{4.4-3}$$

where σ_{mt} and σ_{mc} are tensile and compressive components of magnetic field-induced stress, MPa, subscripts *ec* and *ea* correspond to “easy” *c* and “hard” *a* axes in an “easy” variant (with respect to transversal field), subscripts *hc* and *ha* correspond to “easy” *c* and “hard” *a* axes in a “hard” variant . One can see that Eq. (4.4-3) and Eq. (2.1-3) are identical when the compressive stress term is zero. However, the idea of MSM saturation flux density becomes less explicit. Saturation of “easy” and “hard” variants should be considered independently in this model. Moreover, forces are essentially produced due to the potential of a variant to reorient from one state into another. Therefore, forces should actually be calculated using the results for the same variant in the two consequent states. An assumption that reorientation of a single variant has negligible effects on the magnetic field distribution would allow using data calculated in a single model. However, the validity of such assumption is not obvious and additional study on this topic is required.

Chapter 5. Electromagnetic analysis of MSM actuators

5.1 MSM actuator design and optimisation approach

Geometry and electromagnetic parameters of an actuator essentially determine its performance. The end users usually assess electromagnetic devices based on multiple criteria such as size, efficiency, response speed, output displacement, force and required power supply. However, each of those can be represented as a combined effect of more basic design parameters. This Chapter discusses these parameters in case of MSM actuators, along with their effects on overall actuator performance.

Actuators presented in this study are designed for a 10N/0.1mm output. Having such a specific target in mind would have made designing a usual EM solenoid actuator a rather straightforward task. Unfortunately, this is not the case for MSM actuators. The complication arises from the lack of a mathematical model allowing connecting electromagnetic field solution in actuator's magnetic circuit with forces produced by the MSM element. However, it is possible to relate the overall actuator output to the MSM element performance using available experimental data. Applicability of such an approach is somewhat limited by the availability of measurement results. Nevertheless, it allows designing MSM actuators in the following way.

The curves in Fig. 5.1-1 are provided by ETO Magnetic and show simultaneous strain and magnetic field measurements under different pre-stress levels [24]. These curves are also published in [126]. As discussed in the previous Chapter, the magnetic field is measured in the air gap very close to the surface of the MSM element. Therefore, air-gap flux density should be calculated in a FE model, too. Moreover, average flux density is used since position of Hall sensor in the experiment is not known.

Each point on curves Fig. 5.1-1 relates air-gap flux density to a corresponding combination of stress and strain. A FE model can be set up for every particular shape of the MSM element which explicitly determines output strain (displacement) of an actuator. Hence, actuator output force depends on the curve used for conducting the analysis, whereas output strain is determined by particular points on that curve corresponding to the applied field. This allows calculating current required for a

particular stress-strain combination. However, FE models need to be rebuilt for every particular strain level. This is very important since change in strain affects the fraction of “easy” variants which changes total reluctance of magnetic circuit.

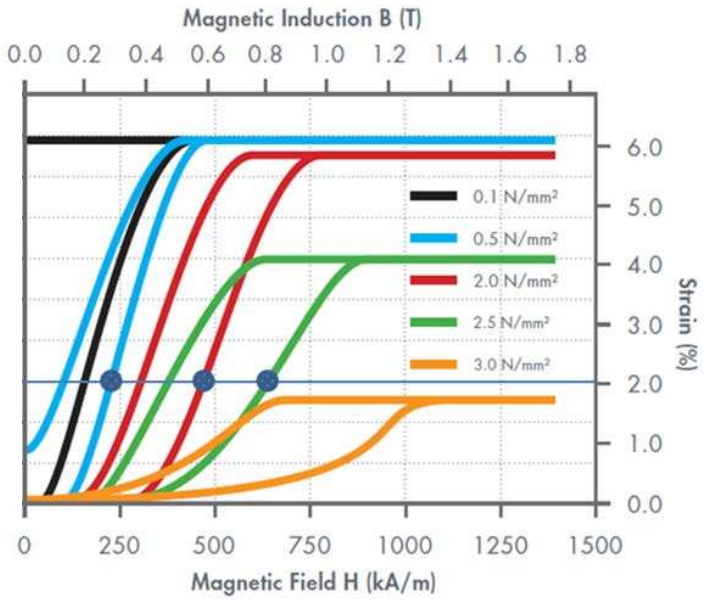

Figure 5.1-1. Strain-magnetic field relation of ETO Magnetic MSM crystals at different pre-stress (load) levels (courtesy of [24])

The smallest possible change in shape is related to turning (switching) one “hard” band into an “easy” one. This quantises the $I(\varepsilon)$ relationship. Nevertheless, a one-band change in shape may provide redundant accuracy in the analysis. On the other hand, the output force curves cannot be obtained as easily. Curves Fig. 5.1-1 do not allow calculating how force changes due to change in input current for a given strain. However, it is possible to estimate this change by moving the operating point from one curve to another. For instance, 3 such points are available for actuators working above 2% strain, whereas 4 points are available otherwise. It should be noted that only elongation part of strain-stress curves is considered. 0.1MPa load curve is not used since it does not allow reversible actuation.

It should be mentioned that stress levels in Fig. 5.1-1 are related to stress output produced by MSM element. However, the MSM element is also loaded by a compressive spring in actuator. Therefore, output stress of an actuator is related to the load curve stress as

$$\sigma_{Eff}(B) = \sigma_{curve}(B) - \sigma_{Comp} \tag{5.1-1}$$

This equation is similar to Eq. (2.1-4) with exception of twinning stress being included into σ_{curve} (see $\sigma_{load.tot}$ in Table 2.1-2). Essentially, stress levels in Fig. 5.1-1 are related to the difference between magnetic and twinning stresses for a particular applied field. This also explains why 0.1MPa stress provides only irreversible actuation. Compressive stress used in this study is 0.5MPa corresponding to twinning stress of chosen crystals.

Figure 5.1-1 allows finding a polynomial approximation for the force-flux density relationship. For the points marked on a 2.1% strain blue line, this polynomial is

$$F_{out} = \left(-6.7633 \cdot {B_\delta}^2 + 11.9807 \cdot B_\delta - 3.2916\right) \cdot A_{msm} \tag{5.1-2}$$

Therefore, it is possible to obtain force-current curves which can give an important insight on the MSM actuator's behaviour. This equation is essentially representing a phenomenological relationship. Whereas it requires unitless input data, B_δ corresponds to air-gap flux density (T) and A_{msm}corresponds to MSM force-producing cross section area (mm^2). This way Eq. (5.1-1) allows calculating actuator output force in (N). Figure 5.1-2 shows force-magnetic flux density relation at 2.1% MSM element strain. Its general trend has a remarkable resemblance with blocking force curve reported in [127].

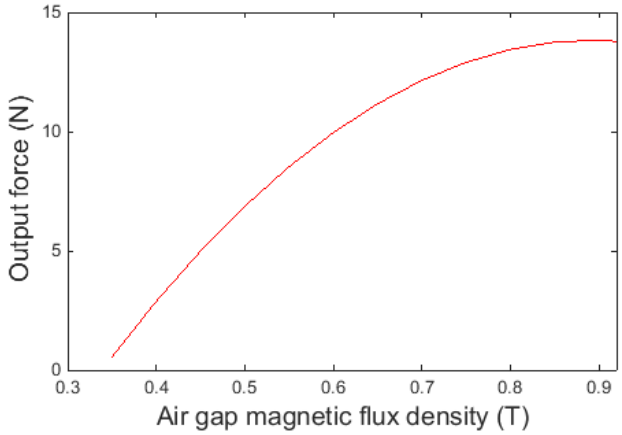

Figure 5.1-2. Phenomenological approximation of actuator output force dependence on air gap flux density at 2.1% strain

However, one should keep in mind that Eq. (5.1-2) has strict applicability limits. For instance, it gives non-physical results for flux density below 0.34T corresponding to 0.5MPa load curve intersection point in Fig. 5.1-1. Figure 5.1-2 also illustrates that output force start decreasing over 0.9T which may not necessarily be the case. Therefore, Eq. (5.1-2) allows reliable MSM force prediction only between 0.34 and 0.9 T. However, this is still relevant for actuators designed in this study which nominal air gap flux density is 0.61T.

Figure 5.1-1 shows that the available output strain decreases as MSM element load increases. This is another feature not captured by existing models which is nevertheless very important for actuator performance evaluation. It should be mentioned that for actuators working in on/off regimes the most important point on a curve is its nominal performance under maximum current. Therefore, the bulk of the analysis is done using final MSM element shape in a cycle, applying 3A current. This allows optimising other important actuator magnetic circuit parameters such as coil and core geometry.

The design and optimisation procedure is illustrated the best by the diagram Fig. 5.1-3. The most important optimisation parameter not directly related to the electromagnetic performance of MSM actuators is total width of magnetic circuit a_f. A task of the actuator width minimisation is related to minimising this one parameter. MSM actuators designed in this study are large-force actuators for use in electro-valves [128], [129]. Actuators used in these specific applications require very compact arrangement of a large number of such valves within a given narrow space. Hence, width of each actuator should be minimised for maximising their number.

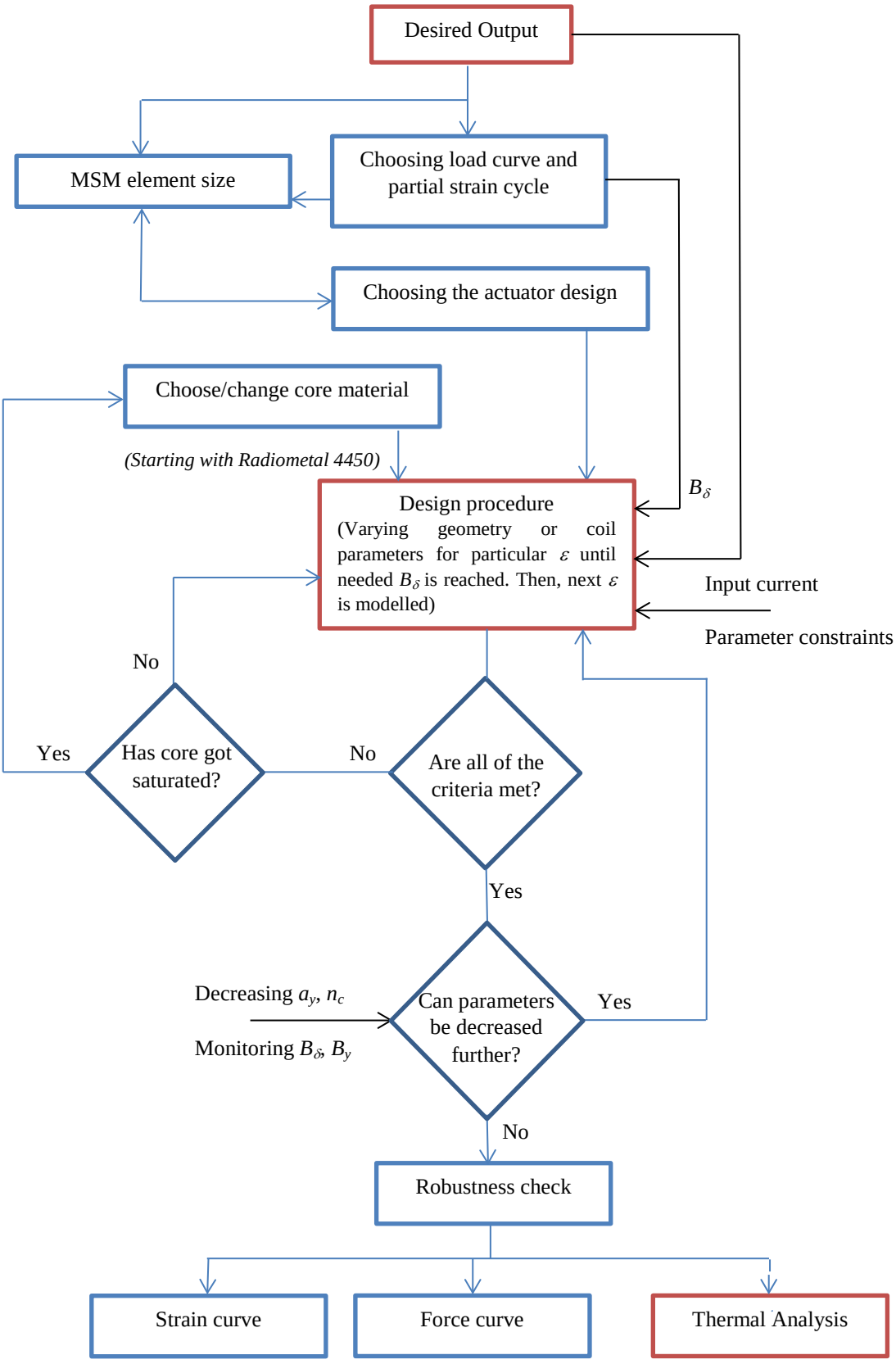

Figure 5.1-3. Actuator design procedure

No particular optimisation algorithm is employed in this study. This is partly due to the lack of well-established mathematical relationship between parameters in the optimisation set. For instance, decreasing yoke width a_y is the most straightforward way to decrease total width of the magnetic circuit. However, this may result in increase of core reluctance due to the shift of B-H curve operating point closer to saturation region. An accepted level of reluctance increase should be compensated by increase in the number of coil turns N_c. However, the number of coil turns affects coil size which can increase the total width. Layers of coil turns can be put one on top of another increasing coil height instead of its width. However, this may lead to unacceptable increase in coil self-inductance. This effect is also hard to take into account analytically and FE analysis should be conducted to evaluate the effects of changes in actuator parameters. Therefore, optimisation is conducted through varying one parameter at a time and tracking changes in order to find the optimal combination. Parameter values are considered optimal when further variation leads to worsening actuator performance or increasing total width of magnetic circuit.

Whereas this procedure was conducted for every designed actuator, it seems redundant to include all the related design characteristics into this Thesis. Figure 5.1-4 illustrates typical trend of change in air gap and yoke flux density with yoke width and number of coil turns. The core steel operating point lies close to the knee of relevant B-H curve. This translates into values of other parameters which lie close to the point where any further change leads to steep decrease in total magnetic flux in the circuit.

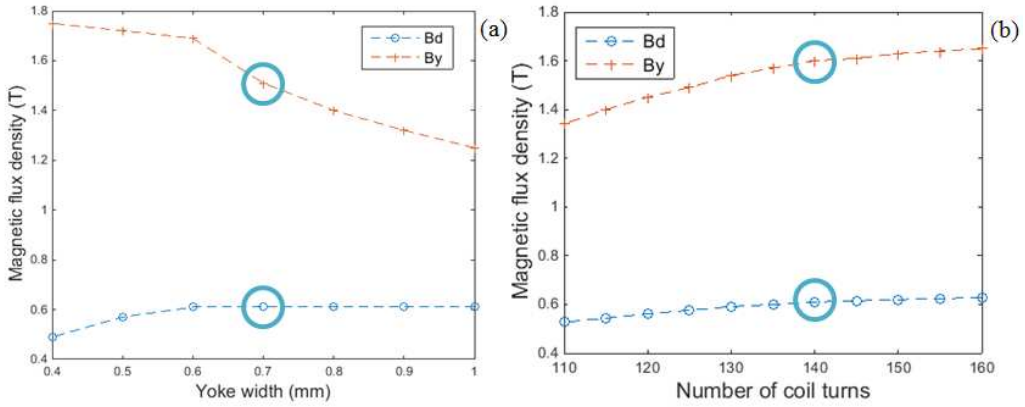

Figure 5.1-4. Change in air gap B_δ and core B_y flux density with (a) core width a_y and (b) number of coil turns N_c

5.1.1 MSM element as part of magnetic circuit

The geometry of MSM element plays major role in determining possible actuator performance. It essentially determines the maximum possible displacement and force output. The most common shape of MSM element used in MSM actuators is shown in Fig. 5.1-5 (left). MSM elements like this produce large strain and small force. However, actuators designed in this study require relatively low strain and large force. Therefore, MSM elements shown in Fig. 5.1-5 (right) are used instead. This geometry comprises shorter MSM elements with large cross-section area on force-output axis due to increased *z*-directional length. MSM elements like one in Fig. 5.1-5 (right) require bigger shape change than the one on the (left) for producing the same displacement. However, they allow producing forces as large as 10N by a very compact MSM actuator.

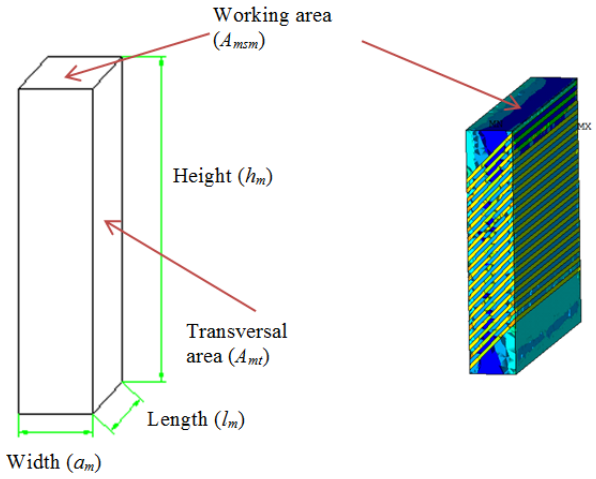

Figure 5.1-5. (Left) Typical MSM element geometry and (right) the one used in this study

A remark about the terminology should be made. Usually the longest of MSM element's faces determines its length and therefore is referred to as "length". Also, it is commonly aligned with the main straining axis determining output strain. As has been briefly discussed above, this face is vertical and, hence straining occurs along *y*-axis. However, due to the necessity to describe MSM element in 3D, the vertical h_m dimension is referred to as *height* in this work (see Fig. 5.1-5). *Z*-axis dimension l_m is referred to as length. It also actually happens to be the longest side in MSM elements optimised for large stress rather than strain output. However, it does not participate in

straining. Finally, *x*-axis dimension a_m is referred to as *width* in order to avoid ambiguity. Figure 5.1-5 also shows that A_{mt} surface of the MSM element is oriented transversely to the applied field, whereas A_{msm} surface is in contact with the push-rod.

The first step in design procedure in Fig. 5.1-3 is choosing an operating stress-strain curve Fig. 5.1-1. It is important to understand the behaviour of these curves. As load increases, the curves tend to move downwards and to the right. The tendency to shift to the right can be explained by the necessity to transduce more energy for overcoming larger loads. What is less obvious is the decrease in available strain. This implies that certain strain-stress combinations become unavailable. For instance, MSM element can elongate only by 1.5% at 3MPa pre-stress level. Thus, a very long MSM element is needed to produce the desired 0.1mm displacement by such a small shape variation, as shown in Table 5.1-1. This is both inefficient and complicated from design point of view. Therefore, a shorter MSM element with more available shape change should be used instead. This also requires switching to a different stress-strain curve. 2.5MPa curve seems a reasonable choice since it fulfils both criteria. However, MSM elements working on a 2MPa curve require almost 25% weaker magnetic field for producing the same strain output. This allows minimising the magnetic core width leading to more compact actuator designs.

Table 5.1-1. MSM element geometry required for producing 0.1mm displacement and 10N force output at different stress-strain curves

Load curve	3MPa		2.5MPa				2MPa	
h_{msm}, mm	20	10	5	4	3.5	3	2.5	2
ε, %	0.5	1	2	2.5	3	3.5	4	5
$A_{msm,\ mm^2}$	4		5				6.7	

Table 5.1-1 shows the overall limit in minimising MSM element height for producing 0.1mm displacement. However, using a very short MSM element which needs to change its shape considerably is not optimal due to the increase in required magnetic energy. For the same reason it is actually much more convenient to use MSM geometry listed for 2.5MPa curve on 2MPa curve. The slight increase in required length of the

MSM element due to the change of load curve is still acceptable. Hence, the final shape of the chosen MSM element is 5mm × 1mm × 6.7mm.

MSM element's width is contributing to the overall reluctance of the magnetic circuit and, hence should be minimised. However, a manufacturing tolerance associated with it currently does not allow decreasing below 1mm. By fixing a_m=1mm, it is possible to calculate l_m required for particular A_{msm} needed for providing the desired force using every strain-stress curve. For instance, l_m =6.7mm for 10N force output on a 2MPa load curve. On the other hand, MSM height is chosen so a desired strain output is achieved in a partial cycle. It also affects saturation conditions of the actuator's core in some designs as discussed below.

5.1.2 Magnetic flux guide design

Magnetic flux guide design is a crucial part of actuator design process. It essentially determines the amount of energy that can be transferred by the magnetic field. In order to do it efficiently, the reluctance of the circuit should be minimised. Equation (3.2-3) shows that it is related to organising the shortest path for magnetic flux also maximising flux guide cross-section area and relative permeability. Whereas the first two are discussed further in Section 5.2, the latter corresponds to choosing the most suitable magnetic materials. Materials most commonly used in EM actuators for flux guide parts are soft magnetic alloys and various types of ferromagnetic steel. Those generally have remarkably high magnetic permeability which depends non-linearly on the applied field. Saturation of magnetic material decreases its incremental permeability to the level of free space making the core essentially non-conductive. Therefore, the capability to optimise the magnetic circuit geometry is closely connected with saturation flux density of the used material.

Three different ferromagnetic alloys were used in actuator designs in this study: Radiometal 4550, Hiperco 50 and Hypermco 50. Radiometal 4550 is a 45% Nickel-Iron alloy with 1.6T saturation flux density. Hiperco 50 is an iron-cobalt-vanadium soft magnetic alloy with 2.4T saturation flux density [130]. Hypermco 50 is an alloy similar to the previous one but with 2.6T saturation flux density. Properties of Radiometal 4550 and Hypermco 50 were found particularly suitable for actuator design in [131]. All three

flux guide materials have very high magnetic permeability. However, saturation flux density differs considerably among them. Therefore, it is interesting to see how actuator designs can vary depending just on the material used for their magnetic circuits. Figure 5.1-6 shows B-H curves of the magnetic materials used in this study.

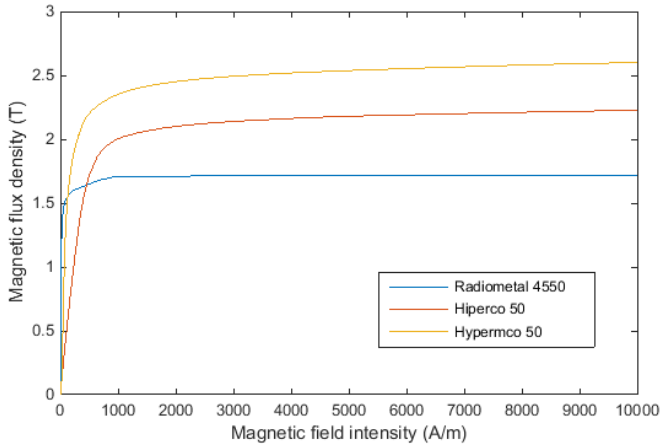

Figure 5.1-6. B-H curves of the used flux guide materials

Ferromagnetic core and MSM element are not the only elements of actuator magnetic circuit. Air regions should also be considered due to their contribution to overall reluctance. Those include air gaps between MSM elements and the core, as well as technological air gaps. The latter correspond to air gaps that can occur in actuators during manufacturing. Whereas their size cannot be accurately predicted, technological air gaps should be taken into account in order to ensure reliable operation of designed actuators. Width of a technological air gap is assumed 0.1mm. Their number varies for different magnetic flux guide designs discussed in Section 5.2. However, it is related to the number of coils used. This is the case since these air gaps mainly occur due to the necessity to allocate a pre-made coil on the core. This can be avoided if coils are wound around the yokes directly, which requires manual work and assumed not feasible.

Air gaps surrounding the MSM element are also 0.1mm wide. Further decrease in air gap width is limited by roughness of ferromagnetic poles and MSM element surfaces, as well as other technological reasons. It is also important that width of both air gaps is kept as accurate as possible for decreasing Maxwell stresses acting on the MSM element, as discussed in Chapter 2.

5.1.3 Coil design for given mmf

Designing a coil essentially means defining its size and the number of turns. It is necessary for a designed coil to provide the mmf needed for the desired actuator output. Coil mmf is the most important parameter since it defines magnetic loads in a FE model. However, geometry of the coil can affect flux leakage and, hence should be carefully considered. In general, the same value of mmf can be obtained through different combinations of input current and number of coil turns. Smaller number of turns makes a coil more compact, though may lead to considerable energy loss and potential overheating. On the other hand, big number of turns leads to a massive coil of high inductance.

3A input current is dictated by a particular design specification in this study. For the known current and required mmf, the corresponding number of turns is calculated by rearranging Eq. (3.2-2) as

$$N_c = \frac{F_c}{I_c} \tag{5.1-3}$$

where F_c is coil mmf, A. The value obtained should be rounded to the bigger integer. Next, a cross-section of the coil wire is calculated. However, current density should be defined first. It should be kept in mind that current density defines thermal loads. For conventional applications, current density J_c exceeding 8 A/mm^2 is not recommended [132]. However, 16 A/mm^2 is chosen here in order to make coils more compact. This is justified by the thermal analysis in Chapter 6 through implementing energy-efficient operating cycle. Effective cross-section of a coil turn can be calculated as

$$A_{N.eff} = \frac{I_c}{J_c} \tag{5.1-4}$$

The diameter of a wire with no insulation is

$$d_N = \sqrt{\frac{4A_{N.eff}}{\pi N_c}} \tag{5.1-5}$$

This diameter should be compared with diameters of available wires. Analysing this is very important for ensuring manufacturing feasibility of designed coils. For instance, most of the actuators designed in this Chapter need very fine wires with diameter about 0.5mm. However, wires of even smaller size are currently available [133]. This allows designing very compact coils which positively contribute to overall compactness of an actuator.

A part of space is taken by insulation and surrounding air in a real coil. Therefore, space required to accommodate a single turn is bigger than that of a pure current-conducting copper. A coefficient which allows taking this into account is coil filling factor. It depends on a wire type, its dimensions and coil configuration. 0.75 filling factor is used in these calculations. Knowing these parameters, total cross-section of a coil is

$$A_c = \frac{A_{N.eff} \cdot N_c}{k_{cf}} \tag{5.1-6}$$

where k_{cf} is coil filling factor. For decreasing width of the magnetic circuit, width of a coil a_c was reasonably minimised. Height of the coil is

$$b_c = \frac{A_c}{a_c} \tag{5.1-7}$$

Equations (5.1-3) – (5.1-7) allow calculating all coil parameters. A designed coil should be included in a final model of actuator magnetic circuit in order to ensure permissible flux leakage. Finally, coil resistance is

$$R_c = \frac{N_c \cdot \rho_{cu} \cdot l_{c.av}}{A_{N.eff}} \tag{5.1-8}$$

where $l_{c.av}$ is average length of a coil turn, m, ρ_{cu} is resistivity of copper, Ohm·m. When coil and core dimensions are known, overall size of an actuator magnetic circuit can be evaluated.

5.1.4 Mechanical spring and supportive mechanical parts

Mechanical parts of the actuator can have significant effects on its performance. Whereas studying those is not part of this research, this Section provides a brief overview of their roles and associated challenges.

The most important and relevant for actuator performance evaluation mechanical part is a spring. Its main role is pre-stressing the MSM element and restoring its initial shape at the end of the cycle. Evaluating actuator dynamics cannot be done without taking spring into account due to its contribution to overall stiffness and energy dissipation [61], [134]. However, it is mainly considered only as a source of compressive stress in this study. The amount of required pre-stress is determined by twinning stress of the MSM element. Two types of twinning stress behaviour have been reported in [77]: decreasing trend with strain and relatively constant and strain-independent trend. This study is conducted assuming the latter behaviour of twinning stress in modelled MSM elements since the former corresponds to crystals with very high (initial) twinning stress. However, compressive force produced by the spring follows Hooke's law

$$F_{comp} = K \cdot x \tag{5.1-9}$$

where K is stiffness of the spring, N/m, and x is displacement, m. Thus, spring force is proportional to the displacement and, hence to strain of the MSM element. This implies larger force produced at the end of the cycle comparing to its beginning. This extra force should be balanced by change in holding current for maintaining the valve closed (see Section 5.3). Therefore, a spring producing relatively constant pre-stress is preferred when twinning stress of MSM element does not change. This can be achieved, for instance, by pre-straining the spring to the extent that MSM shape change would not affect its force much. This is particularly relevant for this study since the displacement produced by the actuator is just 0.1mm.

Another challenge associated with the spring is evaluating its effects on actuator fatigue life. Mechanical spring is arguably the most unreliable element in the actuator. Short fatigue life or deteriorating stiffness of the spring may neutralise the long lifetime potential arising from using MSM crystals' shape change. Therefore, reliable springs maintaining their properties on long time scales are needed. This part should be analysed with extreme care in mechanical and fatigue analysis of the actuator.

There are two different ways of addressing this issue. The first one is related to implementing the operating mode 5 discussed in Section 2.3. However, a rotating magnetic field utilised in that operating mode can by itself be a source of crack growth and actuator malfunction. The other option is use of a magnetic spring instead of the mechanical one. In this case, a permanent magnet can be used as source of the compressive force. It can also be optimised for meeting the above criterion. However, this requires analysing actuator performance including its magnetic spring on every step of the simulation due to its effects on total magnetic field. This can result in considerable increase in complexity of the modelling approach. Redistribution of the magnetic flux due to the presence of an additional mmf source should also be considered. A low-power solenoid actuator can also be used as a "magnetic" spring [77]. However, this significantly increases the complexity of the overall system for obvious reasons.

Another mechanical part also related to the spring is a screw. It was suggested by developers of several MSM actuator prototypes that a degree of freedom in adjusting the spring pre-stress should be included into the design [62], [77]. This is partly related to variation of properties of MSM elements from crystal to crystal. Therefore, compressive pre-stress may need adjusting according to twinning stress of a particular MSM element.

MSM element is connected to the push-rod that translates its shape change into output displacement. Size of the push-rod in the area of connection is subject of mechanical strength analysis. The requirements associated with the push-rod are low weight and high mechanical strength. The former is related to the necessity to ensure high speed of its motion since a heavy push-rod can decrease actuator response speed and even obstacle the shape change of the MSM element. The latter is related to the necessity of

withstanding multibillion cycle interaction between the push-rod and the pneumatic valve walls in a closed state. Possible complications arising from this type of interaction were discussed in [131]. Top of the push-rod can be made of a different material which properties are subject to mechanical analysis.

MSM element is held in air gap by a mechanical holder. This is essentially the only role of this mechanical part. It should be made of non-magnetic material for avoiding increasing flux leakage. Conditions related to minimising the danger of decreasing MSM element fatigue life and the best way to connect it to the holder were discussed in Section 2.2. Figure 5.1-7 illustrates this connection. This ensures that a part of the MSM element is outside the main magnetic circuit. However, this is not shown on actuator design and magnetic field analysis pictures further in this Chapter, where only effective length of the MSM element is modelled. Nevertheless, the mechanically correct connection between the holder and the MSM element is one in Fig. 5.1-7.

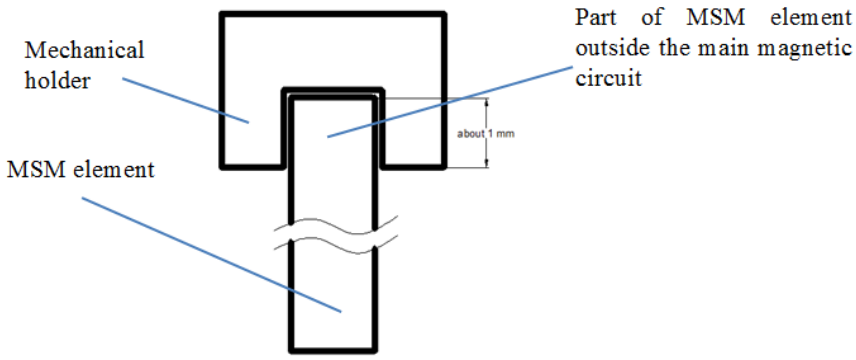

Figure 5.1-7. Connection of the MSM element with the holder

Finally, the complete actuator magnetic circuit and all supporting mechanical parts are enclosed in a housing box. It protects the interior from the undesirable influence of the environment and possible mechanical damages. The box should also be made of non-magnetic mechanically strong material. It is also important that use of this material results in high convective film coefficient with air or water for ensuring low operating temperature of the MSM element, as discussed in Chapter 6. Size of the box should be reasonably minimised due to its contribution to overall width of the device. A box of large width would nullify the effort of minimising the magnetic circuit width discussed further in this Chapter.

5.2 MSM actuator designs

5.2.1 Four designs

A number of possible designs of MSM actuators which are fundamentally different is surprisingly small. This can be partially illustrated by the analysis of operation modes discussed in Section 2.3. The requirement for magnetic field to enter the MSM element transversally pretty much determines how the rest of the magnetic circuit should be organised. Four designs based on Operating mode 2 have been developed and analysed. This number can be increased if permanent magnets and/or magnetic contraction are used. Application of several MSM elements in a single design also broadens the options. However, only four different designs are possible as long as the magnetic circuit is kept as simple as possible.

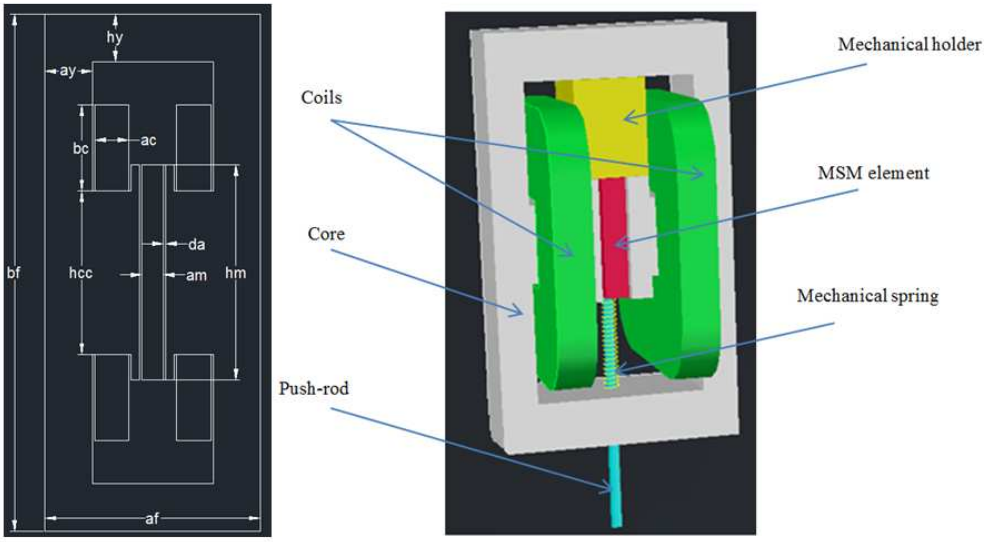

Figure 5.2-1. Geometry of the first actuator design

The first design corresponds to the first MSM actuator design to be ever reported [62]. However, actuators based on this design still appear in more recent papers e.g. [65], [105]. The magnetic field is produced by two coils wound around ferromagnetic poles the MSM element is placed between. The core has two yoke sections which enclose the MSM element and both coils. Therefore, the total flux passing through the MSM element is split in two parts allowing decreasing yoke width a_y. Total width of magnetic circuit is

$$a_f = 2a_c + 2a_y + 2d_a + a_m \tag{5.2-1}$$

Equation (5.2-1) can be rearranged in order to find the space available for allocating a coil for given total width. It should be stressed that this space depends on size of MSM element and air gaps as well as yoke size.

A total z-direction length of magnetic circuit is the same as MSM element's length in this design. It is notable that the total magnetic flux carried by the flux guide is larger for MSM elements with bigger height. For a linear part of core B-H curve and negligible flux leakage, magnetic flux density in yoke is related to MSM flux density as

$$B_y = B_{msm} \cdot \frac{h_m}{2a_y} \tag{5.2-2}$$

Therefore, shorter MSM elements are preferred in this design since a_y is one of parameters to be minimised. Figure 5.2-2 illustrates this.

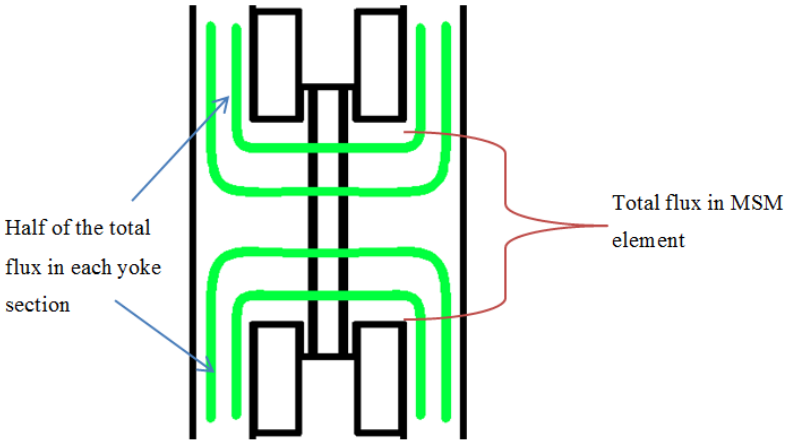

Figure 5.2-2. Flux splitting in yoke regions in the first design

The main disadvantage of this design is its lack of free space above and below the MSM element. As shown in Fig. 5.2-1, a mechanical holder and the push rod are also enclosed by the magnetic circuit. Assembling both these elements is problematic. It is the most complicated in case of rod connection, as it requires drilling a hole in the lower yoke section. This operation will result in significant disturbance of magnetic field distribution decreasing permeability of flux guide. This effect can be addressed by increasing z-direction length of the core. Nevertheless, this operation results in additional complications and non-uniform flux distribution in different yoke sections.

It should be noted that two technical air gaps are likely to occur during assembling the coils. This leads to a larger increase in total reluctance compared to designs where only one technical air gap is to be expected. Another disadvantage of this design is lack of space between coils and MSM element. This can have drastic effects on thermal stability of the MSM element since shielding it from coils' heat is complicated.

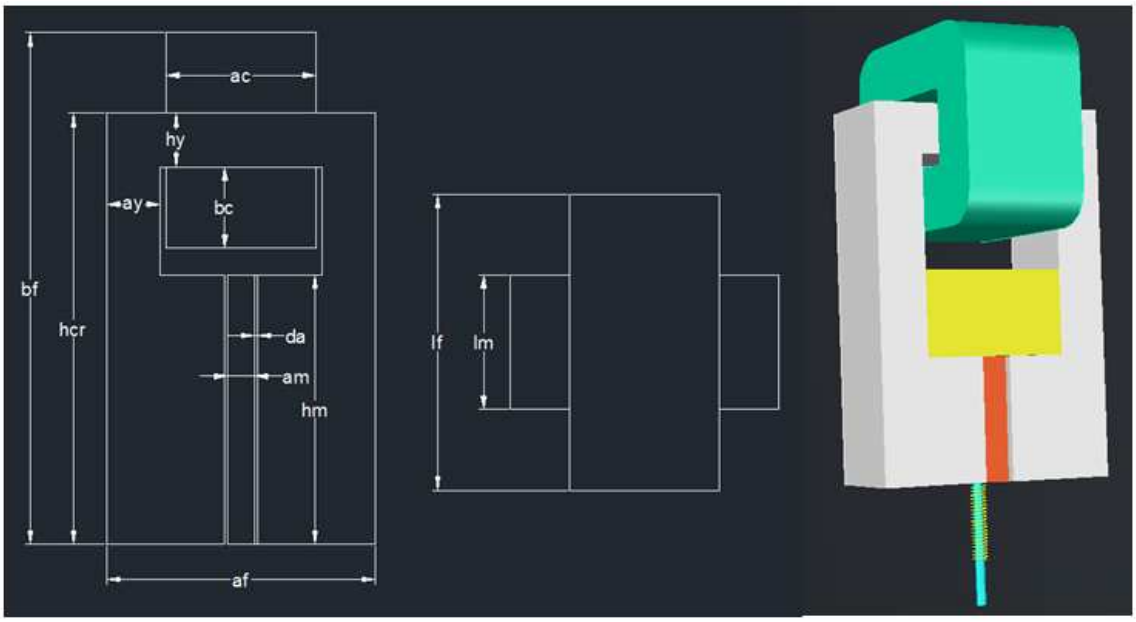

Figure 5.2-3. Geometry of the second actuator design

In order to make the connection of mechanical parts easier, the lower yoke section is removed in the second design. The only coil is wound around the upper yoke section. Here, yoke carries the total magnetic flux conducted to the MSM element, resulting in larger required yoke width comparing to the first design. Magnetic flux density in yoke is related to MSM flux density as

$$B_y = B_{msm} \cdot \frac{h_m}{a_y} \tag{5.2-3}$$

However, more space is available for the coil since it does not depend on MSM element and air gap sizes. The total width of magnetic circuit can be calculated as

$$a_f = a_c + 2a_y \tag{5.2-4}$$

The total length of magnetic circuit equals MSM element's length, and yoke width depends on MSM element's height, similar to the first design. Therefore, this design is more suitable for short MSM elements. The total yoke height h_{cr} can be increased depending on coil size and the space required for allocating a mechanical holder. It also can be increased in order to provide extra space for a cooling window between the coil and the MSM element. It increases the total area of convection surfaces and provides space for water cooling tubes which is advantageous for thermal stabilisation of an actuator (see Chapter 6). Increasing magnetic core's height can be a safe option when ferromagnetic material is not saturated. Otherwise, the increase in height will also result in increasing total reluctance.

Assembling the coil would require only one technological air gap in this design. Therefore, the reluctance added by technical air gaps is smaller comparing to the first design. This design is overall more suitable for manufacturing due to free space below the MSM element for assembling the push-rod and has other important advantages over the first one. However, assembling the mechanical holder is still not easy.

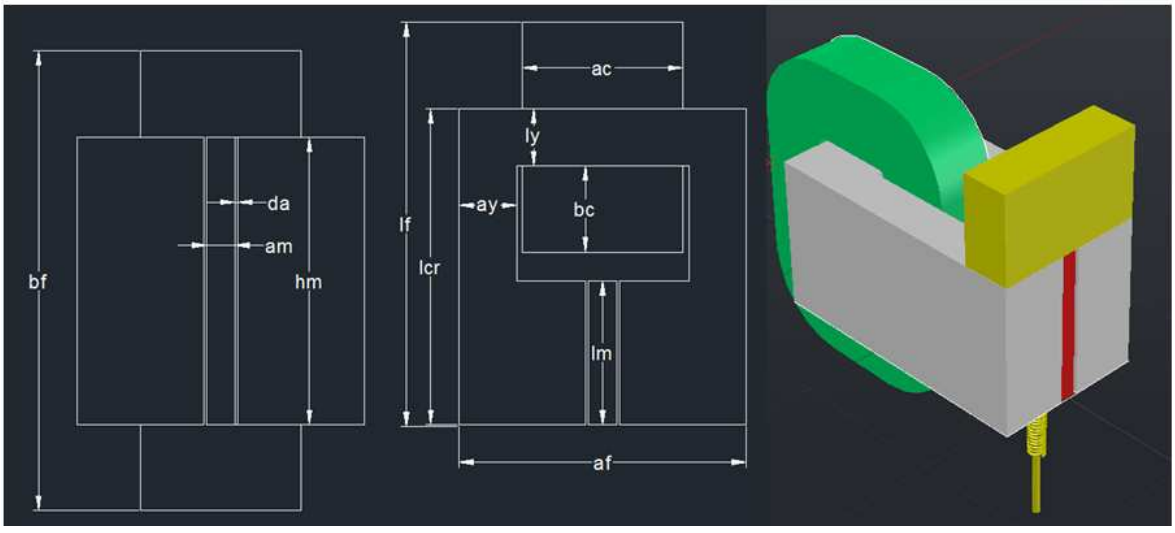

Figure 5.2-4. Geometry of the third actuator design

In the third design, a coil is allocated behind rather than above the MSM element. This allows leaving free space both above and below the MSM element for assembling mechanical parts. Unlike previous designs, yoke width depends on MSM element's length instead of its height. Magnetic flux density in the yoke is related to MSM flux density as

$$B_y = B_{msm} \cdot \frac{l_m}{a_y} \tag{5.2-5}$$

Hence, MSM elements with larger height can easily be used in this design. Therefore, it is more suitable for strain rather than stress production. Equation (5.2-4) can be used for calculating total width of magnetic circuit, as in the previous design.

Overall, this design is very similar to the previous one. However, its specialisation in strain rather than force production makes it much less attractive for the purposes of this research. Also, a cooling window cannot be accommodated in this design.

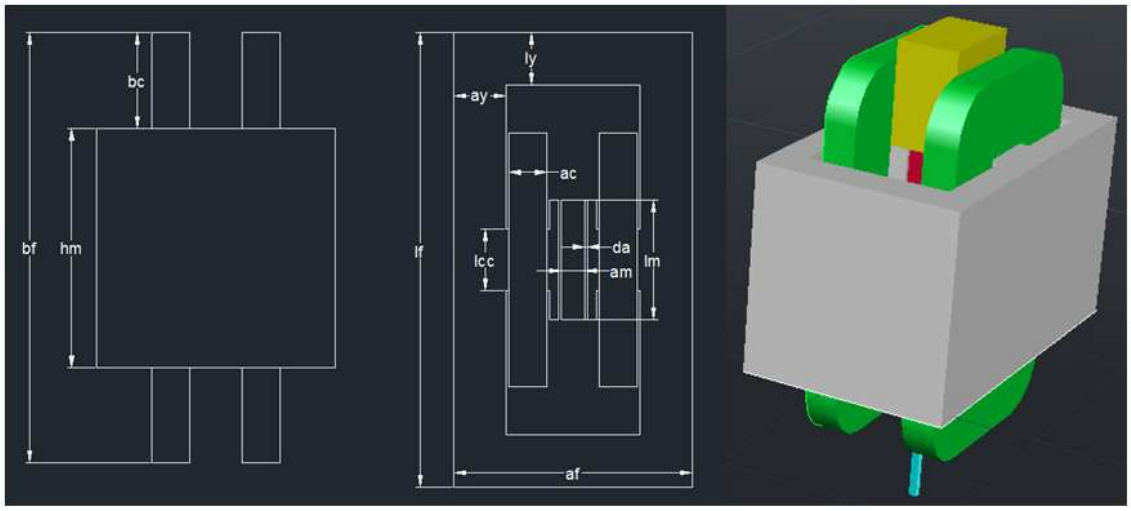

Figure 5.2-5. Geometry of the fourth actuator design

Finally, the idea of changing orientation of the magnetic circuit from vertical to horizontal is applied in fourth design in order to avoid obstructing the space above and below the MSM element, as occurs in the first design. Its magnetic circuit is shown in Fig. 5.2-5. MSM element and two coils are enclosed in the core the same way they are in the first design. This leads to two technical air gaps occurring in the circuit. Equation (5.2-1) can be used to calculate its total width. However, yoke width depends on MSM length here. Moreover, halving of magnetic flux also occurs since

$$B_y = B_{msm} \cdot \frac{l_m}{2 \cdot a_y} \tag{5.2-6}$$

Therefore, this design is more suitable for large strain output actuators similarly to the third one. This fact makes this design unattractive for large-force actuators. However, an opportunity to decrease yoke width due to halving the magnetic flux turns out to be a great advantage. This design still has certain disadvantages of the first design such as close proximity of coils to the MSM element, which is bad for thermal stability of the actuator.

Table 5.2-1 summarises important characteristics of the four discussed designs. The designs chosen for further study are the second and the fourth one. The second design is chosen because of the simplicity of its magnetic circuit, the stress-production orientation of the design, ease of assembling the mechanical parts and the opportunity to include a cooling window. The fourth design has none of these advantages. However, the splitting of the total flux allows decreasing the yoke width significantly resulting in much more compact MSM actuators. This single advantage makes this design very promising due to the importance of minimising the total actuator magnetic circuit width in this study. The first design is not studied further due to the issues related to the inevitable interference between the push-rod and the yoke section of the magnetic circuit. The third design is not studied since it is a displacement-oriented version of the second design, and this study aims to design large-force rather than large-displacement MSM actuators.

Table 5.2-1. Characteristics of four actuator designs

Design	First	Second	Third	Fourth
Preferable MSM element	Short	Short	Long	Long
Preferred output	Stress	Stress	Strain	Strain
Yoke Flux	Half	Full	Full	Half
Number of Tech. air gaps	2	1	1	2
Ease of assembling mechanical parts	Very hard	Average	Easy	Hard
MSM element's thermal conditions	Bad	Good	Average	Bad

5.2.2 MSM actuators based on second design

Table 5.2-2 shows parameters of actuators designed based on second design. Each design is marked depending on core material: “R” for Radiometal 4550, “Hi” for Hiperco 50 and “H” for Hypermco 50. All these actuators produce 0.1mm/10N output at 3A input current. They are optimised for minimising total width of the magnetic circuit. However, only H design meets the a_f<10mm requirement. It should be stressed that further minimisation of total width is not possible due to saturation of the core. Therefore, only an actuator which uses expensive steel with high saturation flux density can satisfy the requirements. Figure 5.2-6 shows the typical magnetic field distribution in magnetic circuit of an actuator designed based on second design.

Table 5.2-2. Parameters of second design MSM actuators

	N_c	a_f, mm	a_y, mm	b_f, mm	l_f, mm	a_c, mm	b_c, mm	B_δ, T	B_y, T
R	140	11.9	3.7	31	23	4.5	7.8	0.61	1.57
Hi	158	10.6	2.8	31	23	5	7.9	0.613	2.0
H	154	9.8	2.4	31	23	5	7.9	0.606	2.28

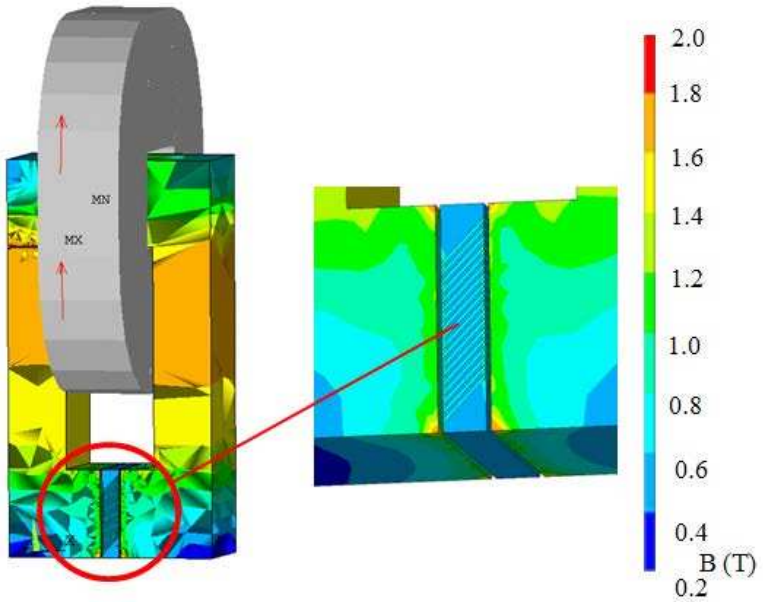

Figure 5.2-6. Magnetic field distribution in R actuator magnetic circuit

5.2.2.1 Core extension in second design

Core saturation prevents further decrease in yoke width in second design. However, it is possible to decrease core reluctance and increase its cross-section by increasing its size on axes other than *x* (horizontal). In case of second design, *z*-direction length of the core can be increased so *x*-direction width can be decreased further resulting in a long but narrow magnetic circuit. Parameters of designed actuators with extended core are summarised in Table 5.2-3. Designs are marked consistently with the discussion above adding "U" as indication of core extension.

Table 5.2-3. Parameters of second design MSM actuators with extended core

	N_c	a_f, mm	a_y, mm	b_f, mm	l_f, mm	a_c, mm	b_c, mm	B_δ, T	B_y, T
RU	114	6.6	1.3	31	64	4	7.1	0.614	1.6
HiU	124	5.8	0.9	31	75	4	7.5	0.61	1.98
HU	120	5.6	0.8	31	75	4	7.5	0.606	2.32

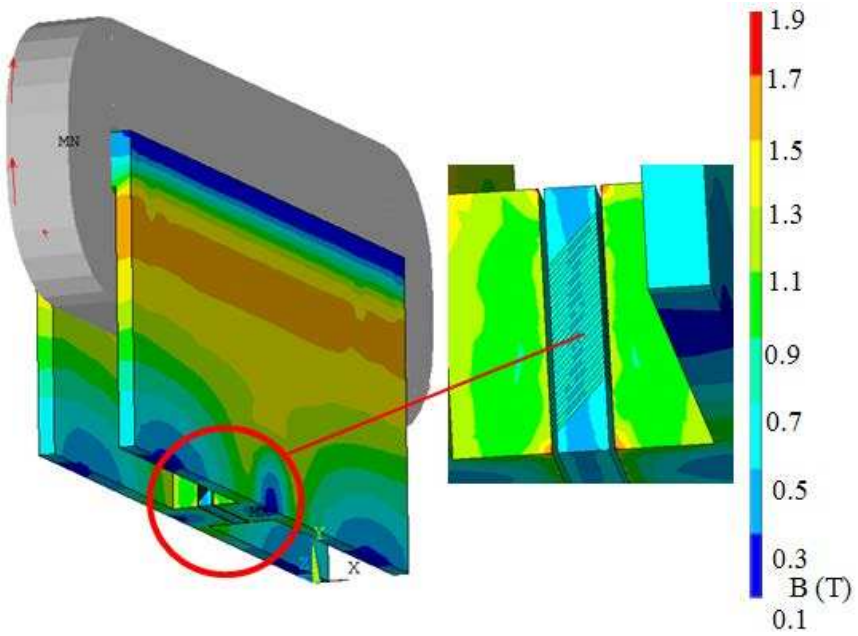

Figure 5.2-7. Magnetic field distribution in RU actuator magnetic circuit

Figure 5.2-7 shows typical magnetic field distribution in magnetic circuit of an actuator designed using second design with extended core. It should be noted that the contribution of the mentioned increase in length decreases with total length. This allows finding the optimal core length after which further increase leads to negligible decrease in yoke flux density. This tendency can be explained by increase in length of flux lines and, hence the path that flux is traveling through the core. It is easy to see from Eq. (3.2-3) that reluctance along the path increases with its length, and the two effects cancel each other out at a certain point.

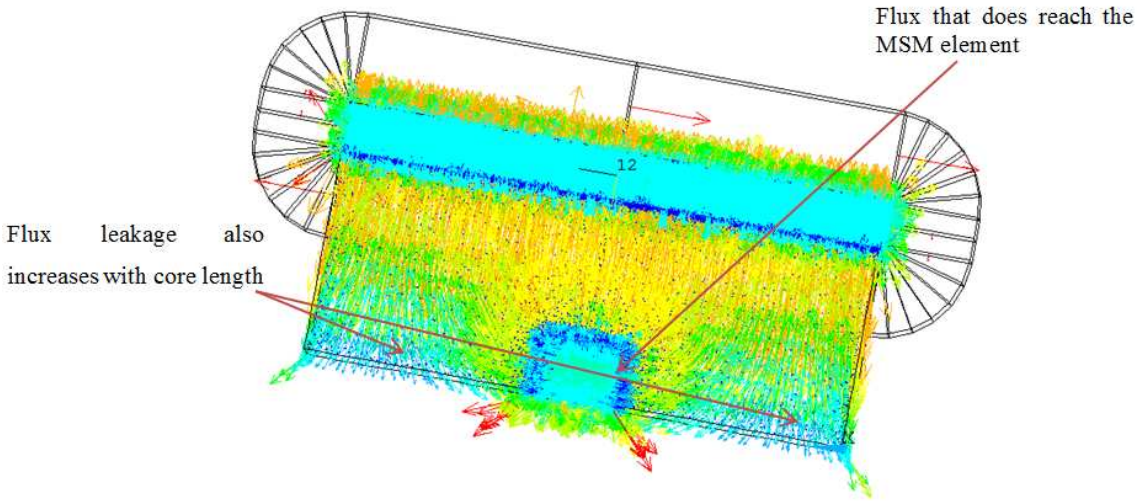

Figure 5.2-8. RU actuator magnetic flux density vector plot

It also should be mentioned that core of such actuators cannot be laminated due to the 3D nature of magnetic field distribution. Therefore, eddy-current losses are larger in these actuators comparing to those with laminated core. It is also clear that coil resistance is huge since coil length depends on core length. An experiment with a coil of length below core length has been conducted. Unfortunately, it resulted in increasing core reluctance cancelling the initial effects of core extension. Large resistance also results in large Joule losses and overall decrease in efficiency. Nevertheless, Table 5.2-3 shows that a remarkable decrease in total width is achieved through increasing core length. Even actuators with core made of Radiometal 4550 meet the a_f<10mm requirement.

5.2.3 Actuator designs based on fourth design

Since none of the abovementioned actuators meet all of the design criteria perfectly, a closer look has been taken at the potential of actuators based on fourth design. Table 5.2-4 summarises parameters of the MSM actuators based on fourth design. New actuators are marked with "2" at the beginning acknowledging two coils. Comparison of Tables 5.2-2 and 5.2-4 shows that fourth design does allow designing smaller actuators. This is unexpected due to doubling of number of technical air gaps as well as the dependence of yoke width on MSM element's length. Despite all this, these actuators do meet the width constraint without having the necessity to accommodate long coils with large resistance. This means that actuators based on fourth design do not require expensive core material simultaneously allowing core lamination. Overall, these actuators possess multiple advantages over previous ones meeting all of the design requirements. The only drawback of these actuators is close proximity of coils to the MSM element.

Table 5.2-4. Parameters of fourth design MSM actuators

	N_c	a_f, mm	a_y, mm	b_f, mm	l_f, mm	a_c, mm	b_c, mm	B_δ, T	B_y, T
2R	126	9.0	1.9	32	21	2	8.1	0.616	1.61
2Hi	134	8.0	1.4	32	21	2	8.2	0.61	2.09
2H	130	7.6	1.2	32	21	2	8.1	0.613	2.38

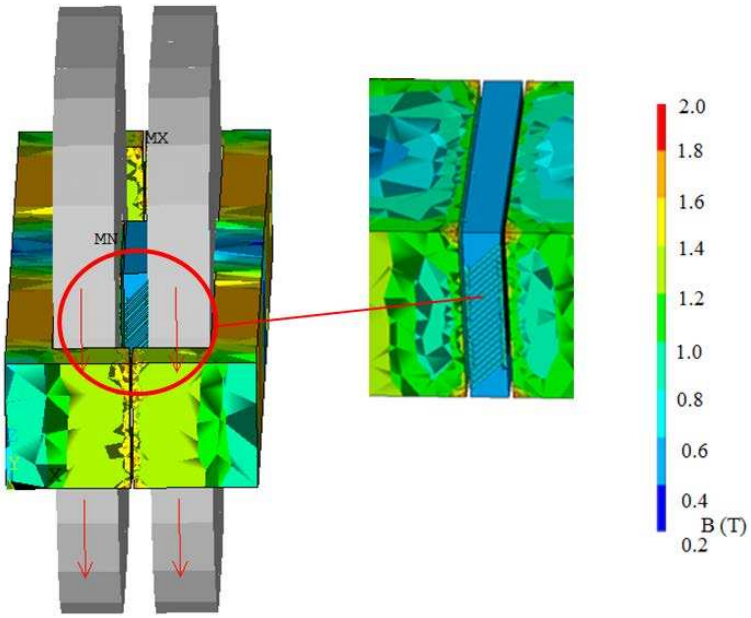

Figure 5.2-9. Magnetic field distribution in RU actuator magnetic circuit

However, one can see that allocating a mechanical holder and connecting the push-rod is still challenging. The space between the coils is approximately 1.5mm. Hence, the holder should be connected front to the back unlike the previous designs where its connection directly to the poles is possible. This illustrates the trade-off between size and magnetic circuit simplicity among second and fourth designs.

5.2.3.1 Core extension in fourth design

The same principle of extending the core has been applied to designed actuators. Height of magnetic circuit has been increased for ensuring a large cross-section for passing magnetic flux even with smaller yoke width. Parameters of designed actuators are summarised in Table 5.2-5. Similar to the results in Section 2.3.2.1, decrease in yoke width resulting in a corresponding decrease in total width has been achieved. However, the core extension does not contribute to coil size in this design. Therefore, extending the core allows decreasing total width without increasing Joule losses. Nevertheless, the 3D nature of magnetic field distribution does not allow core lamination leading to larger eddy-current loss.

Table 5.2-5. Parameters of fourth design MSM actuators with extended core

	N_c	a_f, mm	a_y, mm	b_f, mm	l_f, mm	a_c, mm	b_c, mm	B_δ, T	B_y, T
2RU	104	6.6	0.7	18	25	2	6.6	0.613	1.5
2HiU	108	6.2	0.5	19	25	2	6.8	0.614	2.06

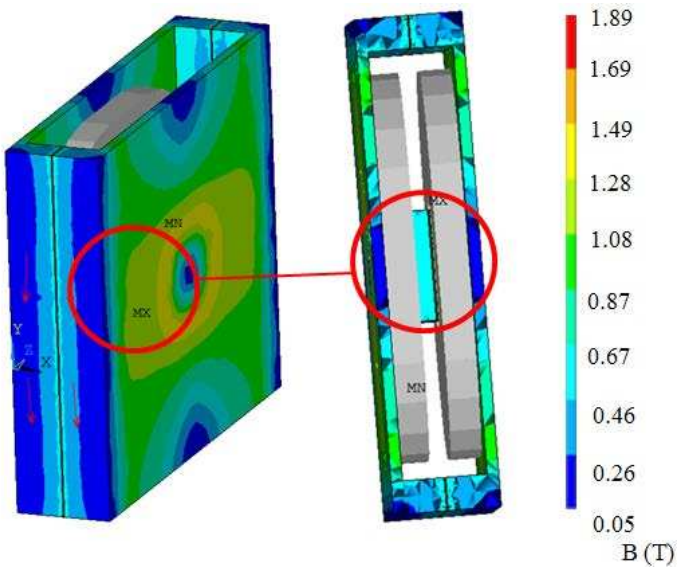

Figure 5.2-10. Magnetic field distribution in 2RU actuator magnetic circuit

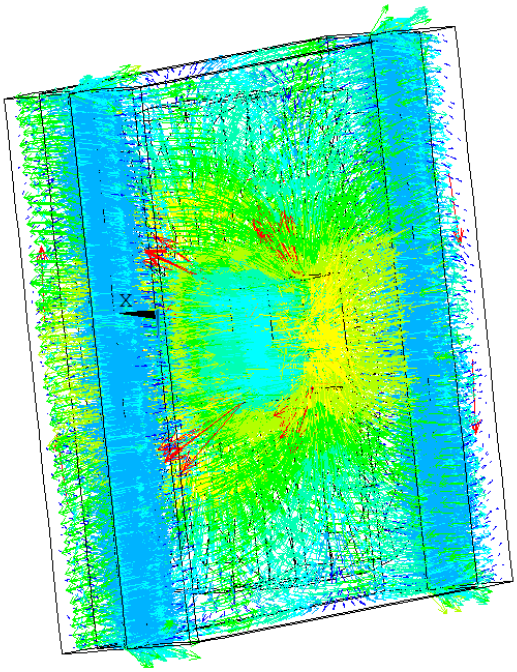

Figure 5.2-11. 2RU actuator magnetic flux density vector plot

It once again becomes obvious that it is actually extremely hard to allocate the mechanical holder in this design. Probably the best suggestion is to use a very long holder which can be connected to the top of the housing box allowing descending the MSM element to its position. This analysis shows that many challenges not related to MSM actuator EM analysis should be solved for ensuring feasibility of the proposed designs.

5.2.4 Output characteristics and robustness

The analysis above results in eleven actuators designed using three different core materials, two initial designs and two variations on those designs. Whereas advantages and drawback of every design have been partially addressed before, the complete comparison of all actuators is summarised in Section 5.4. However, it is still important to evaluate how the actuators perform in conditions other than their nominal regimes. Those changes can be due to change in excitation, load, or manufacturing tolerances related to magnetic circuit geometry.

Output characteristics of EM actuator include output displacement and force dependence on input current. As discussed above, it is only possible to plot strain-current relationship for particular stress levels, and change in output force for a given strain using force polynomial Eq. (5.1-1). However, displacement curves of designed actuators are very similar one to another. Plotting all eleven curves together would make reading the results impossible. Hence, the main trends are illustrated through plotting curves related to one design varying core material in Fig. 5.2-12, whereas curves related to different designs which use the same core material are shown in Fig. 5.2-13. These curves show only slight difference between displacement output produced by actuators, which does not have much influence on on/off operating regime these actuators are designed for. All curves illustrate a slightly non-linear proportional dependence of displacement on input current. MSM element elongation starts from a very small non-zero pre-strained state. It should be noted that these curves correspond only to increasing current during elongation and do not take magneto-mechanical hysteresis into account. The complete cycle is discussed in Section 5.3. The final point of all curves is the same since all actuators are designed for providing the nominal output under 3A input current.

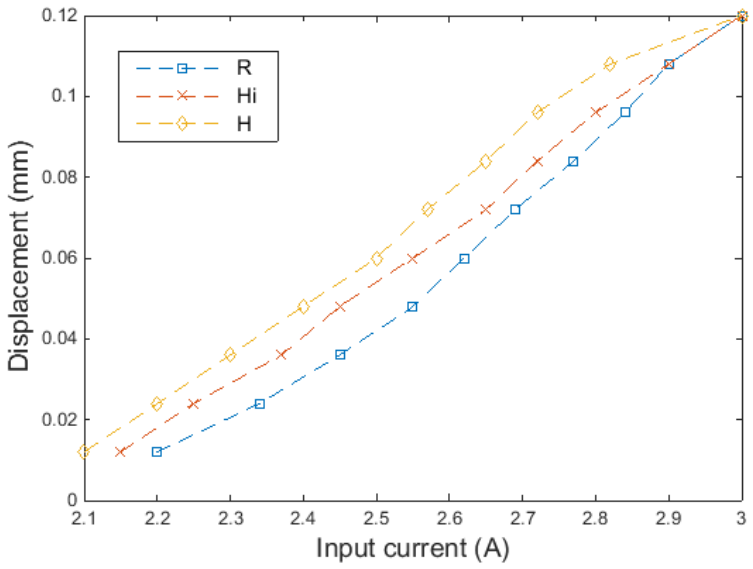

Figure 5.2-12. Displacement output of R, Hi and H actuators

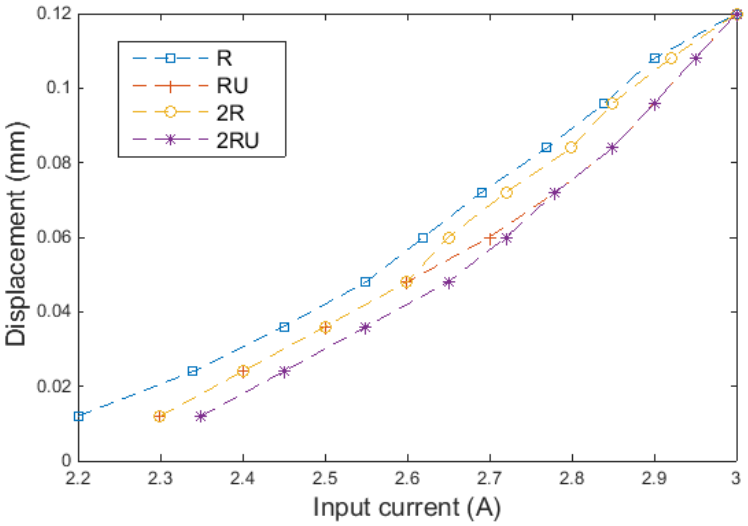

Figure 5.2-13. Displacement output of R, RU, 2R and 2RU actuators

Figures 5.2-14 and 5.2-15 show change in actuators' output force with input current at final strain corresponding to 0.1mm displacement. The output force increases with input current after exceeding a certain threshold. The flattening of the curves at large currents is due to saturation of actuator core. Similar to output displacement, the difference between curves Fig. 5.2-14 is negligible. However, there is some variation in force produced by 4A current in different actuators Fig. 5.2-15.

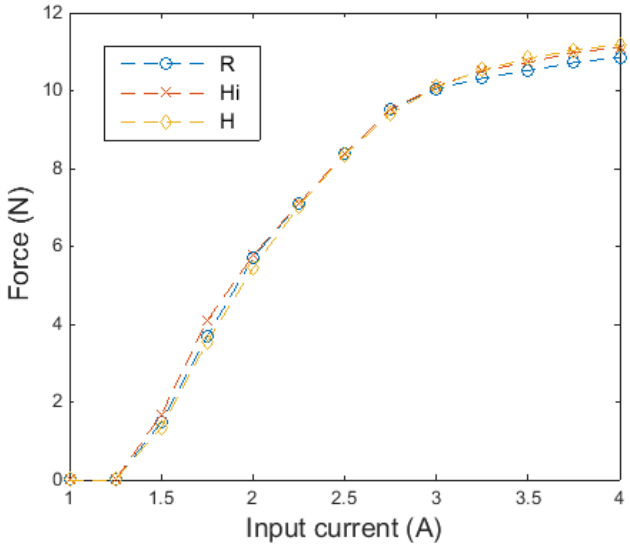

Figure 5.2-14. Output force of R, Hi and H actuators at final strain

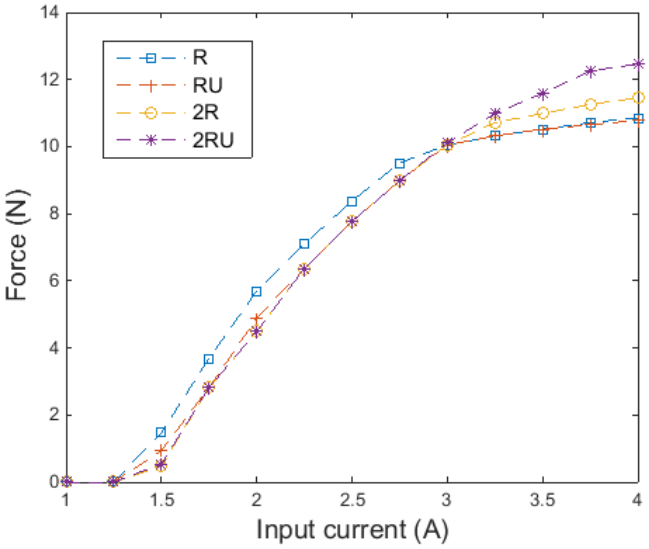

Figure 5.2-15. Output force of R, RU, 2R and 2RU actuators at final strain

It should be stressed that characteristics in Fig. 5.2-12 and 5.2-13 assume that no further elongation is possible after 0.1mm displacement is produced and the valve is closed. However, actuators are capable of producing extra strain output above nominal if additional energy is provided. This is partly evident from the difference between forces produced by 4A current in different actuators in Fig. 5.2-15. The amount of available strain depends on core saturation of a particular design. Since core width has been minimised for minimising total actuator width, core of designed actuators works very

close to saturation. On the other hand, this capability to convert additional energy can be illustrated by the ratio of actuator output forces produced by 4A and 3A (nominal) input currents. This ratio k_{fr} also illustrates the robustness of a particular actuator design with respect to change in actuator load. This parameter is related to the amount of additional available strain due to Eq. (2.1-2).

Table 5.2-6. Ratio of maximum to nominal output forces in designed actuators

	R	Hi	H	RU	HiU	HU	2R	2Hi	2H	2RU	2HiU
k_{fr}	1.08	1.11	1.12	1.08	1.12	1.12	1.14	1.16	1.23	1.25	1.22

Table 5.2-6 shows that force robustness varies slightly among actuators based on second design averaging at about 10%, and increases rapidly for actuators based on fourth design reaching as high as 25% for 2RU actuator. This can be explained by the difference in their magnetic core arrangements which delays core saturation in fourth design.

Table 5.2-6 illustrates the first parameter that allows estimating robustness of a particular design. Generally, robustness characterise the ability of actuator to withstand change in different parameters. Another parameter chosen for illustrating actuator robustness is change in its air gap width. Whereas air gap size is well-defined in the model, it can change due to manufacturing tolerances related to magnetic circuit geometry. Therefore, it is important to ensure that actuators can still produce the required output for the allowed 1A increase in input current. k_{dr} is the parameter related to the ration of maximum allowed to the nominal air gaps. However, this experiment can also be viewed in a different way. Change in air gap is related to change in overall actuator magnetic circuit reluctance. Hence, this experiment essentially shows the ability of actuator to withstand a total change in parameters of its magnetic circuit that affect its reluctance by a cumulative amount. This can as well be related to change in magnetic properties of steel. Therefore, this experiment is more general than it may initially seem. Table 5.2-7 summarises its results.

Table 5.2-7. Maximum allowed increase in air gap in designed actuators

	R	Hi	H	RU	HiU	HU	2R	2Hi	2H	2RU	2HiU
k_{dr}	1.25	1.5	1.45	1.4	1.2	1.2	1.65	1.8	1.75	1.95	1.95

Table 5.2-7 shows that actuators based on fourth design allow much bigger increase in air gap than actuators based on the second design. For instance, 2RU and 2HiU actuators allow almost doubling the air gap whereas HiU ad HU actuators allow just a 20% increase. Comparison of Tables 5.2-6 and 5.2-7 shows that the overall robustness depends on actuator magnetic circuit design as well as chosen core material. It is also important to avoid using flux guide material too close to its saturation point since no increase in total flux is possible. A certain degree of increase should be allowed by the design for ensuring actuator robustness.

5.2.5. Operating actuators at different pre-stress levels

All actuator described previously in this Chapter are designed for working under considerable loads. A part of the theoretically available strain of the MSM element even becomes unavailable due to optimisation of other parameters such as size and input energy. However, it is interesting to see how an actuator designed for working on 2MPa load curve would perform at lower loads. Figure 5.2-16 shows input current-strain curves for R actuator under two different loading conditions. A result is rather remarkable: not only full 6% strain can be utilised under 0.5MPa load, it requires even less current than mere switching under 2MPa load. Hence, much more energy is needed for operating large-force rather than large-strain (displacement) MSM actuators. Thus, actuators presented in this study are at cutting-edge of existing MSM technology since almost all other reported prototypes are displacement-oriented.

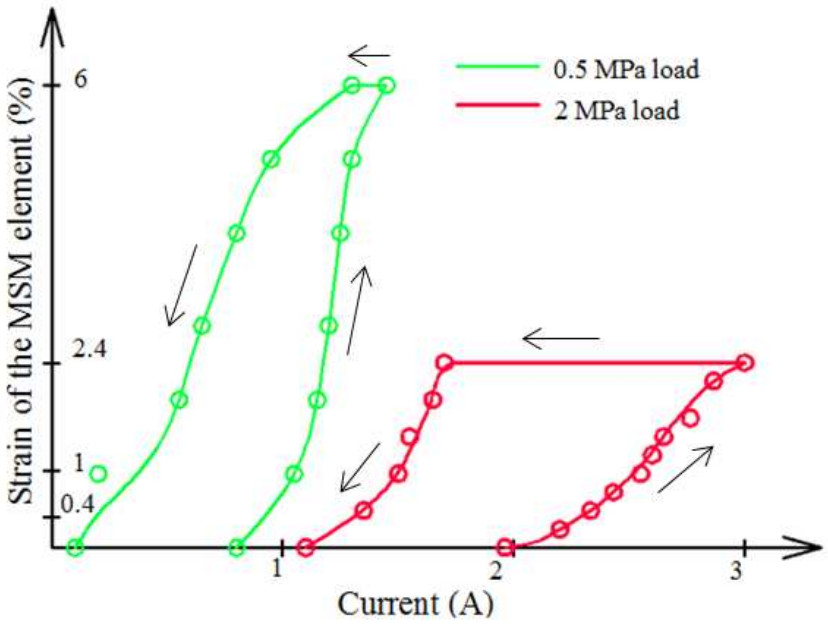

Figure 5.2-16. R actuator performance under two loading conditions

However, it is still interesting to see how small can an actuator be when just 0.5MPa loading is used. One can see that operating large-force actuators for large-strain output at low loads is possible yet not particularly efficient – their magnetic circuits are designed to conduct much larger magnetic flux. An actuator based on third design in Section 5.2.1 was chosen for illustrating the compactness of strain-oriented MSM actuators. Table 5.2-8 summarises its parameters and Fig. 5.2-17 shows the magnetic field distribution in its magnetic circuit. Input current is kept 3A for consistency with the previous analysis. This actuator utilises relatively common 10 x 1 x 2.5 mm MSM element. Hence, full 6% strain translates into 0.6mm displacement produced by the designed actuator. This actuators is marked with “S”.

Table 5.2-8. Parameters of S actuator

	N_c	a_f, mm	a_y, mm	b_f, mm	l_f, mm	a_c, mm	b_c, mm	B_δ, T	B_y, T
S	54	5.4	1.2	20	15	3	5	0.56	1.67

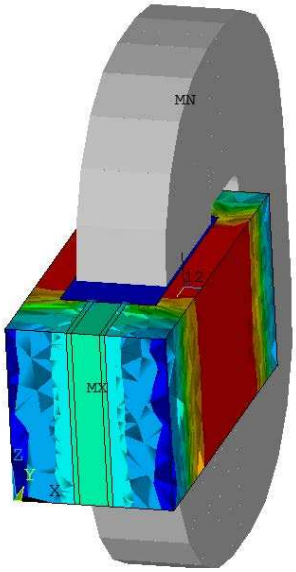

Figure 5.2-17. Magnetic field distribution in magnetic circuit of S actuator

It is notable that width of this actuator's magnetic circuit is smaller than that of the most compact of large-force actuators designed in this study. Moreover, this actuator is designed using Radiometal 4550 core material meaning the possibility of further width decrease through using other core materials. Similar to large-force actuator designs, coil is huge here taking up a lot of space. However, it has just 54 turns corresponding to much lower mmf needed for operating this actuator. It should be noted that third design has been chosen for designing this actuator in order to allow using a long MSM element. Therefore, this result also illustrates how the third design can be successfully applied to large-displacement actuator design.

5.3 Energy-efficient operating cycle

Operating cycle of MSM actuator is closely related to stress-strain curve of its MSM element. Since actuator input current is related to magnetic-field induced stress in the MSM element, both cycles can be analysed simultaneously. There are four main parts in the operating cycle. The initial part corresponds to magnetic fields below switching field resulting in nearly negligible MSM elongation due to magnetostriction (I in Fig. 5.3-1). The second part (II) corresponds to magnetic fields exceeding switching field leading to proportional elongation due to "easy" variants' growth. This part ends when MSM element is fully elongated and further increase in magnetic field does not lead to

shape change. The third part (III) corresponds to decrease in the applied field, whereas full elongation is maintained due to the presence of a holding force. Finally, the fourth part (IV) is related to magnetic fields low enough for compressive pre-stress to overcome the sum of twinning and magnetic stresses contracting the MSM element to its initial state. A partial cycle can be organised by preventing MSM element from reaching full elongation and contraction. As discussed in Section 2.2, operating in a partial cycle is desirable for ensuring very long actuator lifetime. It also allows avoiding the influence of initial twinning stress since twin boundaries neither extinct nor get nucleated.

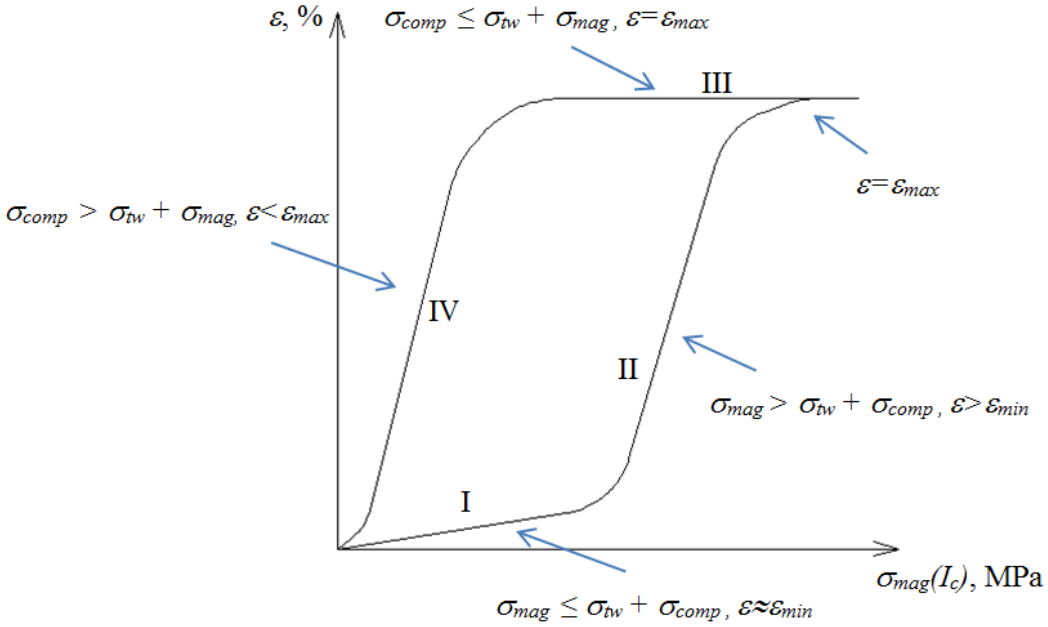

Figure 5.3-1. Operating stress-strain cycle of MSM element

The curve in Fig. 5.3-1 can be converted into current-strain curve Fig. 5.3-2. Only three points on the curve do actually matter for an on/off operating regime: a stand-by current corresponding to initial strain in a cycle (point A), maximum (peak) current corresponding to maximum strain (point B), and minimum (holding) current for which contraction does not occur yet (point C). Switching current is not actually important in on/off regime since partial elongation is not utilised.

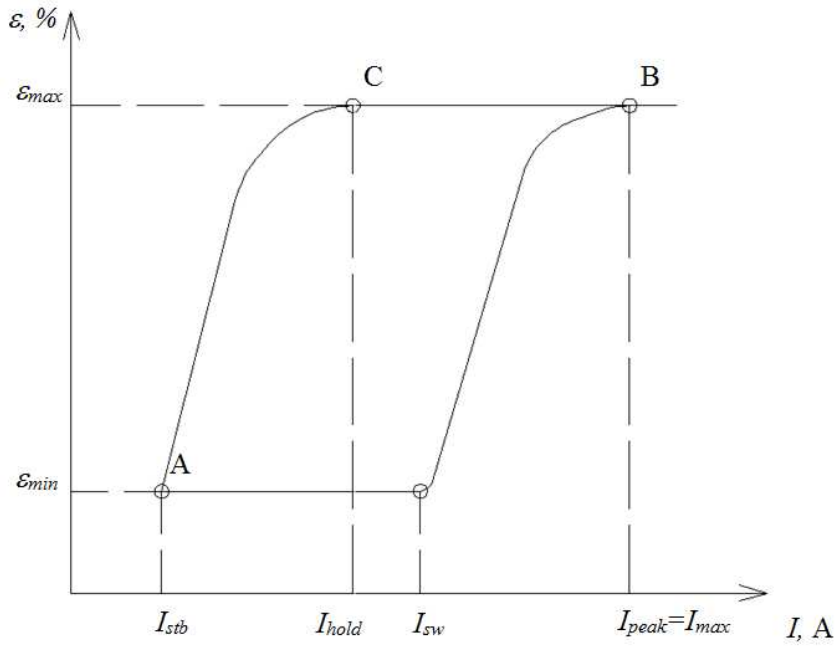

Figure 5.3-2. Input current-strain cycle of MSM actuator

For a transient analysis, operation cycle for an on/off actuator can be divided into four regions with respect to current. The first region corresponds to a steep increase in current for obtaining required strain (A->B in Fig. 5.3-2). This can be done by a short current pulse followed by a much lower current that sustains the position corresponding to the second region (B->C). At the third region, further decrease in current leads to MSM element contraction (C->A). The fourth region corresponds to maintaining stand-by current and initial strain until a new cycle begins (point A).

Distinguishing between peak and holding currents is significantly important since it allows using MSM holding force for decreasing the power required for operating the MSM actuator. Generally, twinning stress (hence, holding force) of MSM element inevitably contributes to hysteresis, heat dissipation and overall decrease in efficiency. However, it is also possible to take advantage of its presence. It has been shown in [135] how energy-efficient operating cycle can be developed for “push-push” MSM actuators operated by pulse excitation. However, the same principle can be applied to electro-pneumatic valves due to pressure change at the end of the cycle. This allows decreasing input current when full displacement is utilised. The complete operating cycle is shown in Fig. 5.3-3.

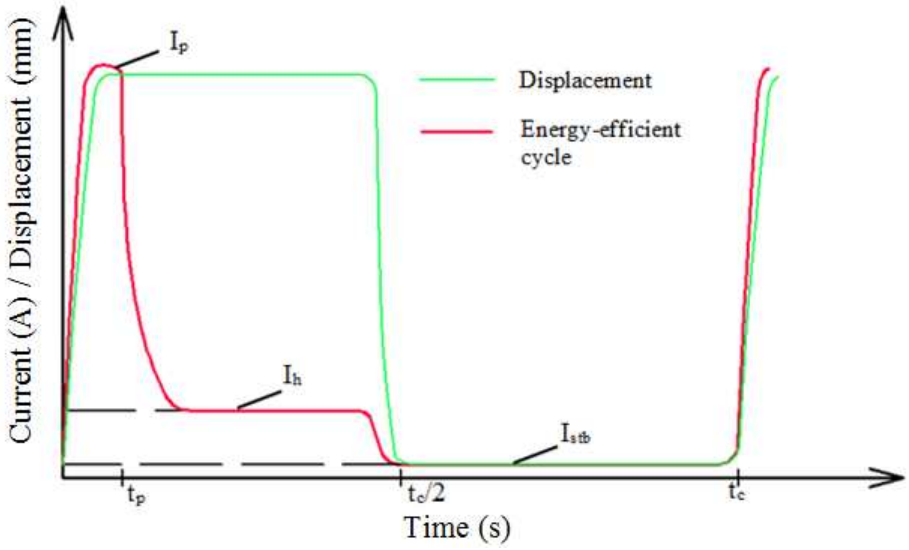

Figure 5.3-3. Change in input current in energy-efficient operating cycle

The difference between pulse and holding currents leads to a significant decrease in power losses. It should be noted that application of such cycle requires use of crystals with considerable twinning stress. Hence, this cycle is more suitable for Twin I rather than Twin II MSM elements.

However, large inductance associated with actuator coil and magnetic circuit complicates application of the proposed approach. Figure 5.3-4 illustrates the EM transient analysis results conducted for R actuator at 2MPa load using pulsed voltage excitation. Operating frequency in the experiment is 300Hz giving t_c=3.3ms. First, a high voltage pulse is applied to the coil at the beginning of the cycle for 0.5ms ramping current to nominal 3A resulting in 0.61T in the air-gap. This is followed by removing current for the rest of the cycle. This should lead to fast decrease in current dissipating electromagnetic energy stored by the coil. However, the analysis shows that current does not naturally fade out fast enough (see Fig. 5.3-4 (b)). Therefore, an additional action is required for initiating MSM element contraction. Here, an additional resistance is added to the coil after current reaches its maximum value. In this particular case it is 4.5 times the coil resistance. This leads to faster current fading allowing reaching 0.18T at the end of the cycle corresponding to initial state of the MSM element (see Fig. 5.3-4 (a)).

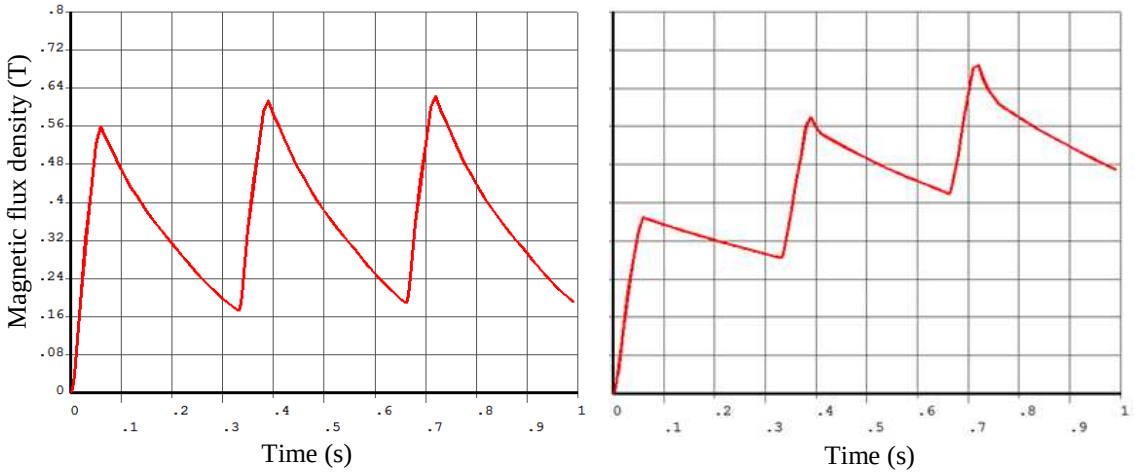

Figure 5.3-4. (a) Forced and (b) natural current fading in pulsed voltage excitation cycle

Fig. 5.3-4 illustrates that MSM actuators respond fast enough for operating at 300Hz when an appropriate control circuitry is provided. It also shows that signals initiating holding and stand-by regimes are not needed in case in Fig. 5.3-4 (b). However, this also implies inapplicability of energy-efficient operating cycle. Therefore, MSM actuators are more prospective for being operated by current sources rather than voltage sources so the cycle in Fig. 5.3-3 can be realised. This argument is also supported by other authors [85], [135]. Operating MSM actuator by voltage source can result in poor efficiency, as shown in [117].

EM devices are usually operated by sinusoidal excitation. However, this type of excitation is very inefficient for MSM alloys due to considerable magneto-mechanical hysteresis. Due to the pressure change in the cycle, actuator load in open and closed valve is different (see Fig. 5.3-5). Hence, no additional input energy is needed after final strain in the cycle is reached. Moreover, less energy is actually required for maintaining the final position. Therefore, actuator power supply should be accordingly adjusted in order to prevent the unnecessary energy dissipation during contraction which may result in considerable increase in actuator temperature. This is the main reason for the energy-efficient cycle implementation. Figure 5.3-6 shows operating cycle of an actuator in electro-valve application. However, it is still impossible to shield the MSM element from heat completely. Some energy loss also originates in the MSM element. However, the discussion in Chapter 2 shows that those losses are much smaller than electromagnetic losses. Thus, minimisation of the latter is the main priority.

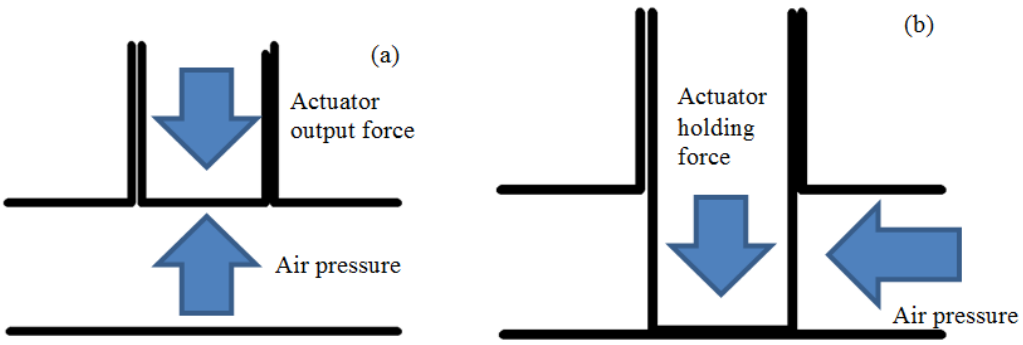

Figure 5.3-5. The direction of air pressure in (a) open and (b) closed states of the valve

Figure 5.3-6 shows two operating regimes of R actuator discussed in Section 5.2.5. However, it is now possible to show that actual cycle is a combination of both, comprising 2MPa elongation and 0.5MPa contraction. This cycle takes into account the pressure change. It also illustrates the significant difference between holding and peak currents.

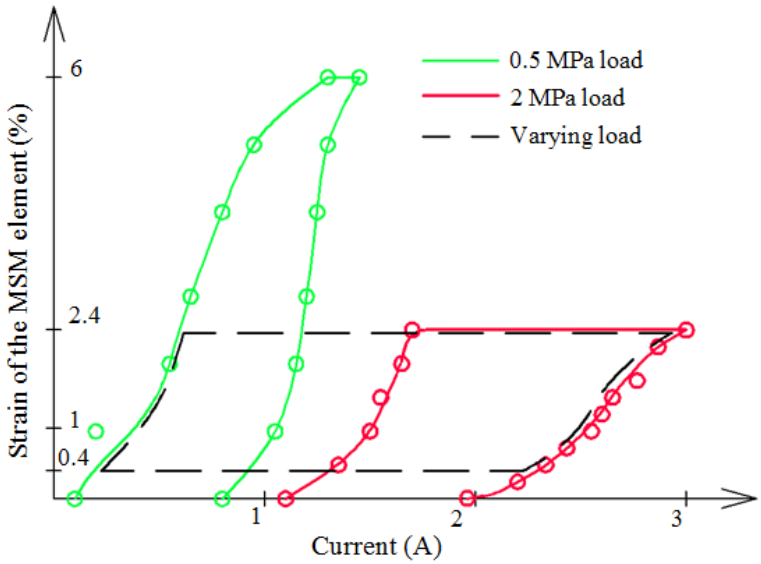

Figure 5.3-6. Output characteristics of R actuator under constant 0.5MPa and 2MPa loads; dashed line shows actual varying load in the cycle due to the pressure change

However, another remark on high-frequency operating of MSM actuators should be made. It is known that increasing frequency signifies effects related to eddy-currents. Those are particularly relevant for electromagnetic devices with magnetic circuits of high-permeable steel, which is exactly the case for materials used in this study. For instance, relative permeability of Radiometal 4550 can reach 40000 [131]. This allows

calculating minimum skin depth of just 0.05 mm using Eq. (3.1-9). However, this result can be somewhat misleading since core permeability changes with input current and varies locally throughout the magnetic circuit. Figure 5.3-7 shows the magnetic field distribution in the MSM actuator magnetic circuit at 300Hz with non-laminated core. It illustrates how the magnetic field gets redistributed due to influence of eddy-currents. Therefore, lamination is essential for using MSM actuators in high-frequency applications. This result supports previously mentioned concerns regarding high-frequency operating of actuator with extended core. Since those designs use 3D nature of magnetic field distribution for decreasing magnetic circuit reluctance, lamination cannot be applied there. Therefore, those actuators are either applicable only at low frequencies or require core material with large electrical resistance for minimising effects of eddy-currents.

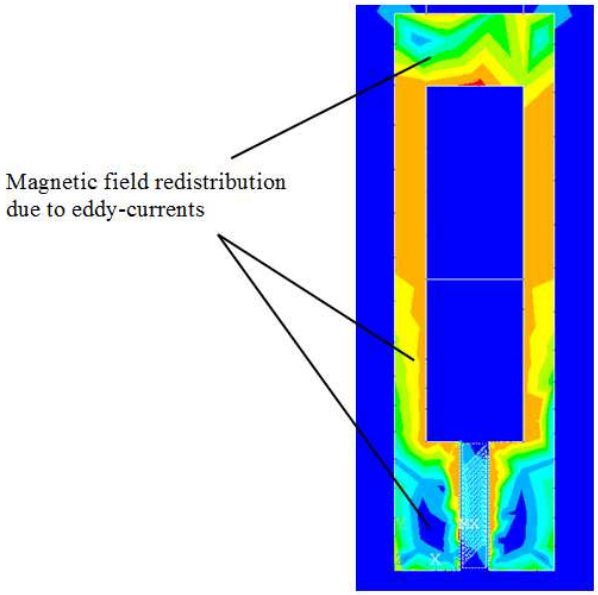

Figure 5.3-7. Magnetic field distribution in non-laminated core of MSM actuator corresponding to peak current at 300Hz excitation frequency

5.4 Summary and comparison of designed MSM actuators

Eleven actuators based on two designs and two additional variations are discussed in this Chapter. Since all actuators are intentionally designed for the same 0.1mm/10N output and have very similar output characteristics, different criteria are used for their comparison. These criteria compare global parameters affecting actuator performance rather than particular design features. In order to compare how compact, efficient, and

robust actuators are, chosen parameters include: total width of magnetic circuit a_f, DC Joule losses at nominal 3A current P_{dc}, number of coil turns N_c, and robustness of actuator designs estimated based on discussion Section 5.2.4.

As discussed in the previous Section, all "U" designs do not allow lamination. This limits their applicability in high-frequency applications considering the discussion in Section 5.3. However, those are preliminary results and further study is required for estimating these effects accurately. Nevertheless, all "U" designs are more susceptible to effects arising from transient phenomena in MSM actuators.

Table 5.4-1 summarises the results of the comparison. It is arranged so reading the Table left to right corresponds to worsening of a particular parameter. The first striking result is that actuators with smallest width are the less efficient and robust. However, this can be expected since those actuators essentially embody the idea of decreasing size at all costs. On the other hand, 2RU and 2HiU actuators are the most robust and efficient also having very low numbers of coil turns, which is an indicative of short response time. a_f in these actuators is also well below the 10mm requirement making them essentially the best of the designed actuators. However, it is interesting to see which actuators with non-extended core also fit the requirements. For instance, 2Hi and 2H are average at all parameters. Their width still allows plenty of space for allocating the surrounding housing. Those actuators are also very robust. 2R and all actuators based on the second design are too close (or overcoming) the 10mm width requirement. Therefore, the final comparison can be summarised as follows.

HU actuator has the smallest 5.6 mm width, but it lacks robustness and efficiency. This is also true for other actuators which are based on second design with extended core. Therefore, those designs can be recommended only for applications where total width of an actuator is the most crucial parameter.

Actuators based on fourth design with extended core are very efficient and robust. They are also very compact complying with the 10mm width requirement. Very low number of coil turns ensures fast response of these actuators. However, they do not allow core lamentation and can be recommended for low-frequency applications.

Actuators based on fourth design with non-extended core have average size and efficiency. However, they do fit all the criteria of this analysis. Hence, these actuators can be recommended for application in pneumatic electro-valves working at frequencies up to 300 Hz. It only should be noted that high saturation flux density steel (like Hiperco 50 or Hypermco 50) is preferable in these actuators.

Finally, actuators based on second design with non-extended core have the width too big for fulfilling the 10mm requirement. Those actuators also have quite a big number of coil turns suggesting a longer response time (which can be compensated by appropriate control circuitry). Nevertheless, those actuators are relatively efficient and reasonably robust. Their design is also the simplest among all actuators.

Analysis of the complexity of assembling mechanical parts reveals considerable challenges, especially in 2R and 2RU design families. The main alternative would be to use third actuator design due to the ease in assembling its parts. However, width of an actuator based on third design cannot be decreased below 13mm. Thus, 10mm width requirement cannot be satisfied. Therefore, it is necessary to find a way to solve mechanical challenges associated with the proposed actuator designs in order to utilise the full potential of conventional MSM actuator technology.

Table 5.4-1. Comparison of global parameters of designed actuators

Parameter	Actuators									
a_f, mm	HU (5.6)	HiU (5.8)	2HiU (6.2)	RU and 2RU (6.6)		2H (7.6)	2Hi (8)	2R (9)	H (9.8)	Hi (10.6)	R (11.9)
N_c	2RU (104)	2HiU (108)	RU (114)	HU (120)	HiU (124)	2R and 2H (126)		2Hi (134)	R (140)	H (154)	Hi (158)
P_{dc}, W	2RU (4)	2HiU (4.1)	2R and 2H (5.2)		2Hi (5.5)	R (5.8)	Hi (5.9)	H (6.5)	RU (12.1)	HiU and HU (15.2)	
Robustness	2RU	2HiU	2H	2Hi	2R	H	Hi	RU	HiU, HU, R		

Chapter 6. Thermal analysis of MSM actuators

6.1 Heat transfer in MSM actuators

Thermal analysis of electromagnetic devices is a very important part of design process. High temperatures resulting from extensive energy loss can considerably decrease actuator lifetime or even result in its malfunction. Electrical insulation is commonly the most thermally unstable element in electromagnetic actuator [136]. Its operating temperature limit is usually much lower than that of other actuator parts. However, this is not correct for conventional MSM actuators. As discussed in Chapter 2, MSM crystals which are currently available lose the MSM effect above 60-80°C. Moreover, the latter corresponds to experimental alloys with larger twinning stress [53]. The 60°C operating temperature limit yields an acceptable increase in temperature of just 37°C. Ensuring such a small temperature rise is a real challenge given considerable power loss and poor cooling conditions of compact MSM actuators used in electro-valves. However, careful analysis of thermal regimes and effects of particular operating cycles and cooling conditions allows obtaining crucial information leading to minimising temperature rise and ensuring stable actuator operation.

Actuators used in electro-valves are usually arranged in rows. A very compact arrangement of a large number of such valves within a given narrow space practically insulates a number of their surfaces, namely their left, right and bottom areas. This complicates convective heat transfer leading to bigger temperature rise. Hence, application of advanced cooling using forced air or even water as cooling fluid is needed. However, an operating cycle discussed in the previous Chapter has an interesting effect on thermal stability of an actuator allowing decreasing temperature rise, simultaneously increasing the overall efficiency.

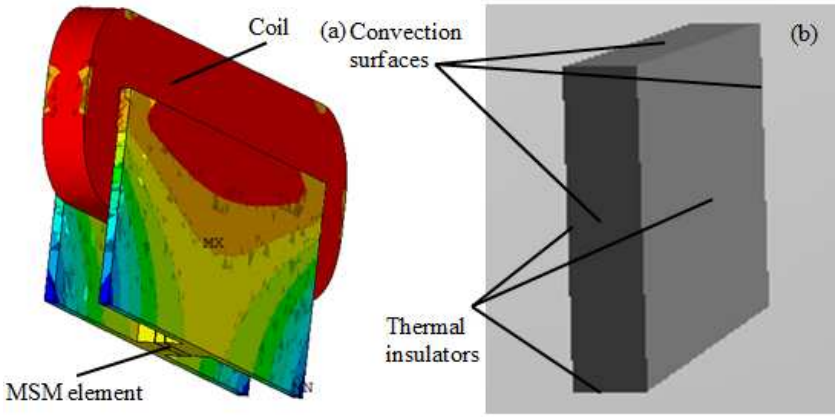

Figure 6.1-1. (a) Temperature distribution and (b) convection conditions in 3D thermal model of RU actuator with no cooling windows

Power losses produced due to electromagnetic and mechanical processes in MSM actuator act as sources of heat in thermal analysis. A comprehensive analysis should involve taking into account each of those contributions. However, calculation of magnetic losses in actuator magnetic circuit and mechanical hysteresis losses in the MSM element are not part of this study. Mechanical losses associated with twinning stress can be neglected since their contribution to temperature rise is rather small even for old specimen with large twinning stress. It is a safe assumption that for new crystals with low twinning stress this source of heating will be getting more and more negligible. On the other hand, magnetic losses due to eddy currents can contribute significantly to heat generation. Their accurate estimation requires careful analysis of transient electromagnetic processes in actuators considering realistic shapes of excitation signals, which is part of future work. Calculations in this Chapter are done assuming that electromagnetic losses are the dominant heat source.

Average power losses can be calculated in order to avoid running time consuming transient thermal analysis. This is possible since thermal processes evolve slower than electromagnetic ones, resulting in essentially no change in thermal fields throughout one electromagnetic cycle [137]. For the operating cycle Fig. 5.3-3, average losses can be expressed with reasonable accuracy as

$$P_{av} = \frac{1}{t_c} \cdot \left(I_p^2 \cdot t_p + I_h^2 \cdot t_h + I_{stb}^2 \cdot t_{stb} \right) \cdot R_c \qquad (6.1\text{-}1)$$

where I_p is pulse (maximum) current, A, I_h is holding current, A, I_{stb} is stand-by current, A, t_p is pulse time, s, t_h is holding time, s, t_{stb} is stand-by time, s, t_c is time length of one cycle, s. Calculation are done for 300Hz frequency yielding t_c=3.3ms. Equation (6.1-1) allows representing power losses of an inherently transient operating cycle with average power losses which produce the same temperature rise in steady-state thermal analysis.

Actuator thermal model consists of a coil, core, a mechanical holder, and the MSM element. All of those elements are enclosed by a housing box. Their thermal properties are summarised in Table 6.1-1. Those are characterised with thermal conductivity k_c. Convection surfaces discussed above include front, back, and upper areas of the box. Film coefficient k_f associated with convection is 20 for forced air cooling. An additional option of using water cooling is considered due to considerable anticipated temperature rise. This option is only applicable to designs that allow incorporating a cooling window (see Chapter 5). Its cross-section can be increased by increasing actuator height. However, height of magnetic circuit is related to reluctance of the core. Therefore, excessive increase in cooling window size can lead to worsening the magnetic properties of the magnetic circuit. A height of 5 mm is used in this study as a trade-off between these two parameters. This leads to a cooling window size of approximately 20 mm^2 varying slightly among the designs.

Table 6.1-1. Thermal properties of materials used in thermal analysis

	Core (R designs)	Core (Hi/H)	MSM element	Coil (copper)	Coil (insulation)	Mechanical Parts
k_c, W/m·K	13	29	16	385	0.4	17

The cooling window can be used in forced air cooling system for increasing total convection surface area. Therefore, studied cooling conditions also include forced air convection in actuators with and without the cooling window, and mixed cooling with water tubes in the window and exterior air cooling (see Fig. 6.1-2). A coil water cooling system proposed in [138] is very effective due to proximity of water to the main heat

source – the coil. However, it is not applicable to compact actuator design due to considerable increase in overall size. Therefore, direct water cooling is not considered in this study. Convective film coefficient for water cooling varies considerably in the literature. Its value used in this study is 300, which is among the lowest reported. It can go up to 3000 in carefully arranged cooling systems.

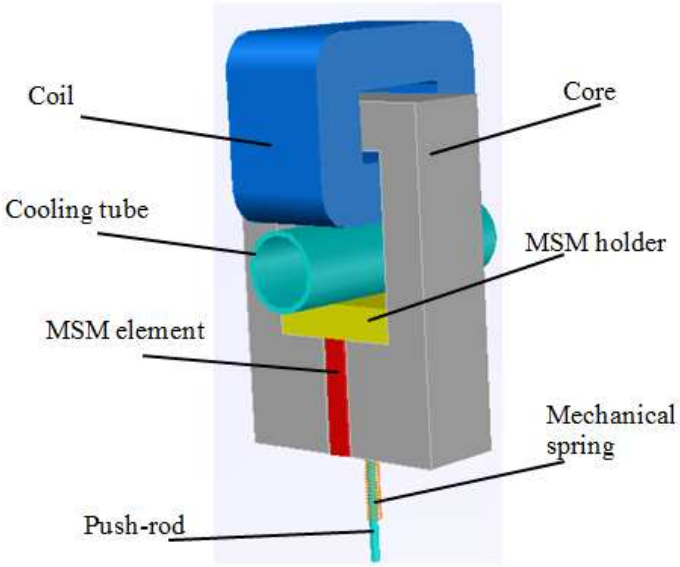

Figure 6.1-2. Second actuator design with a water tube in the cooling window

Energy-efficient operating cycle discussed in Section 5.3 is used for calculating average power losses. However, the pulse length is not a well-defined parameter since it depends on capability of the control circuitry. Nevertheless, it is interesting to see how time length of the current pulse affects thermal regime of an actuator. Three different cases are studied: half-cycle pulse (for which t_h=0), 0.5ms and 0.2ms pulse cycles. Time duration of holding and stand-by sections are calculated based on t_p. Implementation of holding and stand-by currents leads to just 4.7% and 0.4% of "pulse" losses produced in corresponding parts of the cycle. The latter has essentially a negligible effect on thermal regime of an actuator. Each of these contributions is taken into account when average power losses are calculated.

6.2 Steady-state temperature rise in designed actuators

In order to make understanding the information summarised in this Section easier, a particular notation is employed. Cooling conditions are marked with Roman numerals: I correspond to external forced air cooling, II corresponds to exterior and interior forced air cooling (in the cooling window), III corresponds to exterior air and interior water cooling. Regarding the cycles, A corresponds to a half-cycle pulse, whereas B and C correspond to 0.5ms and 0.2ms pulse cycles. For instance, a combination of half-cycle pulse excitation and water cooling can be written as A-III.

Temperatures in the Tables below are related to increase in temperature over the ambient. Green and yellow colours show regimes suitable for MSM crystals with 60 (37) and 80 (57) degrees Celsius operating temperature limit. Since the latter corresponds to novel and experimental crystals, the former represents the temperature rise which is currently acceptable. However, it is interesting to see which regimes become applicable due to 20°C increase in MSM element's transformation temperature.

6.2.1 R/Hi/H designs

Table 6.2-1 shows the dependence of MSM element's temperature in R/Hi/H designs depending on cooling and excitation conditions. Power losses produced in each cycle are also included for reference. It illustrates the expected trend of temperature decrease with better cooling conditions or decreasing power loss. However, neither of the designed actuators can work without implementing one or two of the above conditions. Overall pattern is very similar for all three actuators. They can be operated by long-pulse excitation only if water cooling is implemented and high-temperature MSM crystals are used. Cycle B also allows stable air-cooled operating of two designs. This option is more energy efficient since the advantage is gained through decreasing actuator's losses rather than implementing an additional water cooling system. One can see that application of energy-efficient cycle is usually sufficient for thermal stability if cooling window is present in the design. Shorter pulse length in cycle C allows operating all actuators even with conventional MSM crystals.

Table 6.2-1. MSM element temperature increase in R/Hi/H actuators

	R			Hi			H		
	A	B	C	A	B	C	A	B	C
Losses	2.88	0.97	0.47	2.97	1.0	0.48	3.24	1.1	0.53
I	132	44	21	151	51	24	177	60	29
II	122	41	20	139	47	23	162	54	26
III	47	16	8	50	19	8	56	19	9

General comparison of R/Hi/H actuators was done in the previous Chapter. One of the features of these actuators is increase in power loss along with decrease in overall size as core material changes from Radiometal 4550 to Hypermco 50. This also results in increasing thermal loads along with worsening of convection conditions. This is reflected by gradual increase in temperature among the designs. However, it is rather small since the only notable difference is inability of H actuator to operate in B-I regime. On the other hand, different reasoning applies if only 60°C crystals are considered. Only very short pulses or B-III combination ensures thermal stability. Therefore, it is particularly important to operate R/Hi/H designs using carefully designed control circuitry.

Figure 6.2-1 illustrates the temperature distribution in R actuator. As one can expect, the coil has the highest temperature among actuator elements. Temperature decreases with the distance from the coil. This observation supports the argument made in the previous Chapter that distance between the coil and the MSM element affects thermal state of the latter. However, the overall change in temperature is just 5°C. On the other hand, even such a small steady-state temperature difference can be an advantage if actuators with similar losses and convection conditions based on different designs are compared.

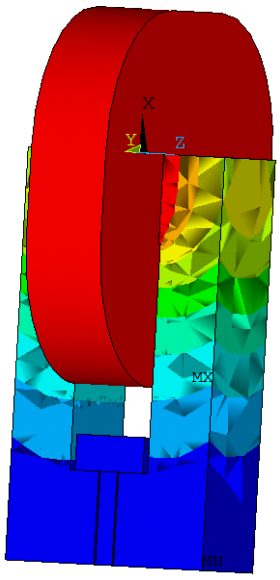

Figure 6.2-1. Temperature distribution in R actuator

6.2.2 RU/HiU/HU designs

Table 6.2-2 shows the MSM element's temperature in RU/HiU/HU designs depending on cooling and excitation conditions. As discussed in the previous Chapter, these designs take advantage of core extension for minimising magnetic core width by increasing actuator length. Whereas this indeed allows decreasing overall actuator width considerably, its effects on thermal stability of the actuator are very negative. MSM element temperature rise is much bigger here than in R/Hi/H actuators due to much larger losses. One may expect that convection conditions of RU/HiU/HU actuators are better since their bigger size results in bigger convective surface area. However, this also increases coil size simultaneously increasing coil resistance and losses. Moreover, side walls which can contribute to the convection substantially are obstructed and do not participate in heat transfer. On the other hand, the effects of implementing a cooling window are the most apparent in these designs. Table 6.2-2 shows that the MSM element temperature can be decreased by half through changing between I and II cooling conditions. Adding water cooling results in more than one order decrease in temperature finally leading to thermal stability. Overall, it is possible to operate RU/HiU/HU actuators by adding cooling windows and using energy-efficient operating cycles. Nevertheless, these actuators are the most inefficient among designed actuators which also makes their thermal regime the most unfavourable for the MSM element.

Table 6.2-2. MSM element temperature increase in RU/HiU/HU actuators

	RU			HiU			HU		
	A	B	C	A	B	C	A	B	C
Losses	6.0	2.0	1.0	7.6	2.5	1.2	7.6	2.5	1.2
I	318	107	52	423	142	69	437	147	71
II	159	53	26	186	62	30	188	63	31
III	19	6	3	20	7	3	20	7	3

Figure 6.2-2 illustrates temperature distribution in RU MSM actuator. The difference between coil and MSM element temperatures is just 2°C. This is due to large distance between the MSM element and convective surfaces. However, addition of a cooling window to the design results in a more effective heat transfer from the coil also shielding the MSM element. A conclusion can be made that second actuator design with extended core benefits significantly from having a cooling window which explicitly justifies its implementation.

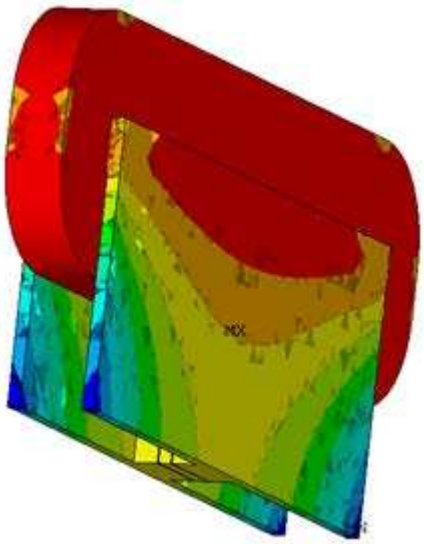

Figure 6.2-2. Temperature distribution in RU actuator

6.2.3 2R/2Hi/2H designs

Table 6.2-3 shows the dependence of MSM element's temperature on excitation conditions in 2R/2Hi/2H actuators. Allocation of a cooling window and, hence implementation of advanced cooling conditions is not possible here due to the structure

of this actuators' design. Therefore, it is important to decrease their losses since neither of the actuators can reach stability in long-pulse cycles. Moreover, very short pulses are needed. However, these actuators are very efficient since electromagnetic losses are very low. The difficulty of achieving thermal stability here is related to bad convection conditions, unlike previously discussed actuators. Therefore, good overall efficiency can be obtained by operating these actuators using appropriate control circuity.

Table 6.2-3. MSM element temperature increase in 2R/2Hi/2H actuators

	2R			2Hi			2H		
	A	B	C	A	B	C	A	B	C
Losses	2.6	0.9	0.4	2.7	0.9	0.4	2.6	0.9	0.4
I	126	42	20	139	47	23	138	46	22

Figure 6.2-3 illustrates temperature distribution in 2R MSM actuator. It shows a similar pattern of decreasing temperature with distance from the coils. However, the MSM element is allocated in close proximity to heat sources in this design. Its temperature is essentially the same as temperature of the coils. Moreover, there are no simple ways of shielding it from the generated heat. This result shows that some aspects of this design which are advantageous in electromagnetic analysis result in considerable complications when the thermal stability is considered. Therefore, it is particularly important to decrease power loss and heat generation rate even further.

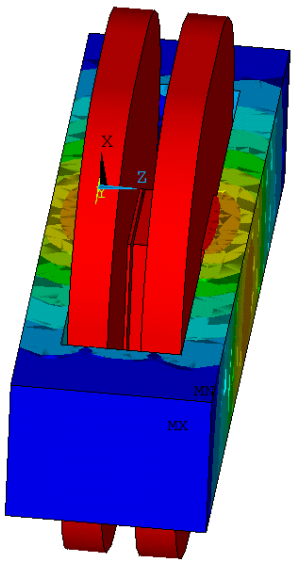

Figure 6.2-3. Temperature distribution in 2R actuator (mechanical holder is hidden)

6.2.4 2RU/2HiU designs

Table 6.2-4 shows the dependence of MSM element's temperature on excitation conditions in 2RU/2HiU actuators. These actuators have the lowest losses among all designed actuators resulting in less complicated thermal regime comparing to the previous design. Table 6.2-4 shows that 2RU can work stably in B-I regime, whereas 2HiU requires a more thermally stable MSM element for this purpose. Otherwise, the same reasoning regarding excitation and convection conditions applies here. However, these actuators require analysing magnetic losses in order to evaluate their thermal regimes correctly. Whereas this is true for each of designed actuators, magnetic losses can be expected to contribute much more dramatically in extended core designs due to bigger volume of iron as well as inapplicability of lamination.

Table 6.2-4. MSM element temperature increase in R/Hi/H actuators

	2RU			2HiU		
	A	B	C	A	B	C
Losses	2.0	0.7	0.3	2.1	0.7	0.3
I	93	31	15	133	45	22

Figure 6.2-4 illustrates temperature distribution in 2RU MSM actuator. Similar to the previous design, the highest temperatures correspond to coils and the MSM element. Temperature also gradually decreases with proximity to convection surfaces. Nevertheless, the position of the MSM element is thermally very unfavourable. Optimisation of energy efficient cycle for the shortest pulse length is the best possible way of ensuring thermal stability of these actuators.

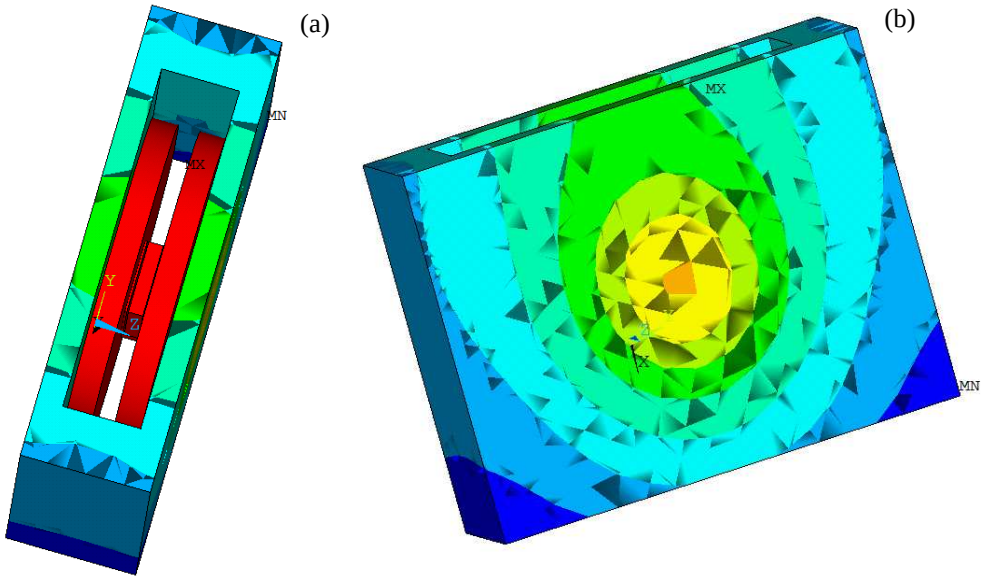

Figure 6.2-4. (a) Upper and (b) side view of temperature distribution in 2RU actuator (mechanical holder is hidden)

6.2.5 Comparison of thermal regimes in designed actuators

Thermal analysis has been conducted for eleven designed actuators. The results are overall consistent among the designs: all of them require either improving cooling conditions or implementing the energy-efficient operating cycles for ensuring thermal stability. Since size of the actuator affects the convection conditions, actuators that are considered less promising based on electromagnetic analysis in Chapter 5 work in better thermal regimes. R/Hi/H actuators illustrate this by having the highest number of available options in Table 6.2-1. However, actuator designs with two coils are still very compact, efficient and can achieve thermal stability when an appropriate control algorithm is employed. On the other hand, very compact RU/HiU/HU actuators are less thermally stable. Whereas convection conditions are relatively good in these actuators, large coil size and considerable electromagnetic losses are the main reasons for complexity of their thermal regimes. These actuators require cooling windows and short current pulse excitation for achieving stability. Water cooling is another suitable option for these actuators.

Application of energy-efficient operating cycle is very beneficial for thermal regimes. Implementation of B and C cycles leads to 3 and 6 times decrease in coil losses, respectively. This has very positive effects on thermal regime in designed actuators. Since application of water cooling system is associated with considerable increase in complexity of the valve, it is worth comparing designed actuators on basis of whether or not they are able to work in B-I or B-II regimes. These regimes do not require water cooling and allow average-length current pulses making the control circuitry simpler. Therefore, these actuators can be considered the best from thermal and control point of view. Table 6.2-5 shows the results of this comparison. Total width of an actuator magnetic circuit increases left to right in the Table. Colours are related to 60 and 80°C MSM crystals, as in previous Sections.

Table 6.2-5. Applicability of B and C cycles in designed actuators

	HU	HiU	2HiU	RU	2H	2Hi	2RU	2R	H	Hi	R
B-I/ B-II	No	No	Yes	Yes	Yes	Yes	Yes	Yes	Yes	Yes	Yes
C-I/ C-II	Yes	Yes	Yes	Yes	Yes	Yes	Yes	Yes	Yes	Yes	Yes

It is interesting that only one design meets this criterion. However, almost all other actuators would operate in this regime if MSM element with higher transformation temperature is used. This once again emphasises the potential benefits of having MSM alloys that work at higher temperatures.

The main results can be summarised as

- It is possible to achieve thermal stability in MSM actuators by implementing carefully designed control circuitry and/or improving cooling conditions. However, even a slight increase in transformation temperature of MSM alloys would lead to availability of a number of additional options.
- Actuator convection conditions are related to its size: the smaller the actuator, the harder it is to manage its thermal state. It is crucial to decrease actuator losses even further for designing thermally stable actuators, especially if implementation of energy-efficient cycle or advanced cooling is not possible.
- Implementation of short-pulse current cycles ensures low temperature rise of the MSM element and increases efficiency of actuators. Current sources are much more promising for operating MSM actuators since decreasing current to holding and stand-by levels is possible.
- Forced air cooling is only sufficient when short-pulse cycles are used. Otherwise, implementation of water cooling is needed.
- Water cooling is a possible solution which improves heat sink significantly. However, it increases the overall complexity of the valve system. It also does not increase actuation efficiency. Hence, combination of air cooling with energy efficient operating cycle is preferable.

Overall, use of the well-designed control is the most reliable and efficient mean of ensuring thermal stability in the designed MSM actuators. Since the MSM element phase transformation temperature is the limiting factor in thermal analysis, its increase will significantly simplify the overall thermal regime of an actuator allowing more stable options. It is also remarkable that the use of the shape memory effect coupled with the analysis of the pressure change in the valve allows decreasing electromagnetic losses significantly, resulting in thermal stability of the designed actuators that could not have been reached otherwise. The analysis of the complete valve system also leads to a significant increase in overall efficiency.

Chapter 7. Conclusions and further work

7.1 Conclusions

Considering the Aim and Objectives in Section 1.2, the work discussed in this Thesis can be summarised as follows.

(a) *To choose the most suitable MSM element for actuation*. The research of the available MSM alloys summarised in Section 2.1 has led to identifying that 5M Ni-Mn-Ga MSM crystals with Type I twin boundaries are currently the most suitable for actuation. Whereas they do not produce maximum strain and stress output among MSM alloys, the combination of very long fatigue life with relatively low twinning stress makes them the most prospective for use in MSM actuators. Crystals with different microstructures produce large displacement at expense of stress production, which is not optimal when implemented in large-force actuators. Whereas 5M crystals with Type II twin boundaries possess very small twinning stress leading to very low switching field and high efficiency of magneto-mechanical energy conversion, they currently are very unstable which makes their use in long lifetime applications unreliable, as shown in Section 2.2.

(b) *To develop a methodology for design and modelling of MSM actuators*. FE analysis discussed in Section 4.1 was used as the main tool for modelling and evaluation of MSM actuator performance. The MSM permeability change with strain which translates into the change in magnetic circuit parameters of the actuator was also studied in Section 4.3. This has led to the development of a modelling approach which allows including the complete MSM actuator magnetic circuit into a single model. Implementation of such approach is crucial for capturing mutual influence between the MSM element and the rest of the magnetic circuit. Moreover, it has been shown in Section 4.3.4 that the change in MSM permeability can be used for actuator design optimisation. This approach has been used for designing very compact and high performance actuators discussed in Chapter 5.

(c) *To study the time-depended processes related to operating the MSM actuator*. Electromagnetic transient analysis has been conducted in order to ensure that designed actuators can be used at frequencies up to 300Hz in Section 5.3. However, additional means of increasing the speed of current fading during MSM element contraction are needed when MSM actuator is driven by voltage-source due to high inductance of its coil(s). On the other hand, implementation of current-source excitation allows avoiding this, also making possible to implement the energy-efficient operation cycle discussed in the same Section. Its implementation is beneficial not only for decreasing energy loss and unnecessary power supply, but also for ensuring thermal stability of the MSM element in actuators.

(d) *To analyse thermal regimes in MSM actuators*. 3D thermal analysis has been conducted for studying thermal regimes and cooling conditions of the designed actuators in Section 6.2. It shows that it is indeed possible to ensure the acceptable temperature rise of the MSM element. The most effective and energy efficient route is implementation of the appropriate control which takes advantage of the MSM element's holding force and pressure change in the valve discussed in Section 5.3. Otherwise, water cooling may be needed leading to increase in complexity of the system. Moreover, water cooling decreases temperature but not the power loss, having no positive effects on the overall efficiency. Therefore, application of a carefully developed operating cycle is much more beneficial for the overall performance.

(e) *To design robust, large-force, long life-time MSM actuators*. Eleven large-force actuators were designed and studied in Section 5.2. These actuators employ different magnetic circuit geometries and core materials leading to a considerable difference between the designs. Advantages and drawbacks of every actuator are discussed in Section 5.4 with an additional emphasis on compactness and efficiency. Most of the designed actuators meet the initial design specifications and can be operated stably in B or C cycles, as discussed in Section 6.2.5. Their long lifetime is ensured by meeting all the important criteria for long fatigue life of the MSM element in actuators discussed in Section 2.2. The main aim of this project is therefore achieved.

7.2 Contribution to the original work

Whereas the modelling approach presented in this study is developed for actuator design, it is applicable to performance evaluation of essentially any other MSM application where permeability or magnetisation change is utilised. This is particularly relevant for MSM sensors. This work is essentially the first one that studies the MSM magnetic field distribution and variation in magnetic properties of the MSM element in such detail. Whereas the effects of MSM permeability change are known for a very long time, their impact on the performance of MSM-based devices is still highly underestimated. This work shows the significance of these effects through very careful and detailed study of the magnetic field distribution in anisotropic MSM twin variants. Moreover, it shows how MSM actuator magnetic circuit can be optimised when these effects are taken into account in the modelling approach. The fundamental nature of this study also leads to better understanding of previously reported experimental results, where non-homogeneity of field distribution and local saturation of MSM twin variants are commonly not considered.

Actuator designs discussed in this study explore all possible magnetic circuit arrangements which do not involve permanent magnets or rotating magnetic fields. Moreover, an idea of extending actuator magnetic core in a particular direction for increasing its permeance is successfully applied in two designs. The analysis also allowed distinguishing between the designs particularly suitable for displacement or force production.

Presented actuators are also cutting edge of the current technology showing how compact and high-performance MSM actuators can be. The conducted thermal analysis also illustrates possible ways to ensuring their thermal stability. Thermal characterisation of MSM-based devices is still addressed poorly in available literature, which acknowledges existence of the considerable challenges yet lacks suggesting ways to dealing with those. This work shows that application of a carefully designed current-driven operating cycle allows decreasing energy loss and heat generation in MSM actuators dramatically. This, combined with the appropriate cooling, allows decreasing MSM element temperature rise to an acceptable level ensuring overall actuator stability.

7.3 Further work

Thermal stabilisation of MSM actuators is one of the main challenges related to implementation of the technology. This issue is addressed in the material study society through researching new ways of manufacturing crystals with higher transformation temperature. However, this should also be addressed by actuator and control design engineers through minimising energy loss and organising the most effective operating cycles. Further work will concentrate on further decreasing of electromagnetic losses in actuators. The question of the most appropriate shape of excitation signal will be studied further in order to, for instance, evaluate the minimum length of the current pulse. Future analysis of MSM actuators will also include calculation of magnetic losses related to eddy-currents inducted in the magnetic circuit. However, it is essential to calculate those using the developed excitation cycles rather than more general relations, which are usually based on the data measured using sinusoidal excitation. This is particularly relevant for actuators which design does not allow core lamination.

A model for actuator dynamics which includes its mechanical parts will also be developed. It will also include variation of different parameters such as change in twinning stress and MSM element's cross-section area with strain. Influence of twinning stress change on actuator performance should be studied further in order to evaluate the effects of its temperature dependence on overall actuator output.

A need for a comprehensive model for evaluating magnetic field-induced stresses has been identified. Development of such a model is essential for avoiding using models which rely strongly on measurement data. This will allows gaining flexibility for designing actuators and other MSM-based devices working in regimes for which experiments have not been conducted yet.

Finally, fatigue life of MSM actuators should be studied further. Whereas the conditions for long lifetime actuation are formulated in this Thesis, the analysis of reliability of other actuator parts such as mechanical spring and coil insulation are needed. Designs with magnetic contraction which do not require mechanical pre-stress will also be studied in order to evaluate possible advantages of using permanent magnets as a mean of increasing actuator lifetime.

References

[1] K. Ullakko, J. K. Huang, V. V Kokorin, and R. C. O'Handley, "Magnetically controlled shape memory effect in NiMnGa intermetallics," *Scr. Mater.*, vol. 38, no. 10, pp. 1133–1138, 1997.

[2] A. A. Likhachev and K. Ullakko, "Magnetic-field-controlled twin boundaries motion and giant magneto-mechanical effects in Ni–Mn–Ga shape memory alloy," *Phys. Lett. A*, vol. 275, pp. 142–151, Oct. 2000.

[3] S. J. Murray, M. Marioni, S. M. Allen, and R. C. O'Handley, "6% magnetic-field-induced strain by twin-boundary motion in ferromagnetic NiMnGa," *Appl. Phys. Lett.*, vol. 77, no. 6, pp. 886–888, 2000.

[4] A. Sozinov, N. Lanska, A. Soroka, and W. Zou, "12% magnetic field-induced strain in Ni-Mn-Ga-based non-modulated martensite," *Appl. Phys. Lett.*, vol. 102, no. 2, p. 021902, Jan. 2013.

[5] A. Sozinov, A. A. Likhachev, and K. Ullakko, "Crystal Structures and Magnetic Anisotropy Properties of Ni – Mn – Ga Martensitic Phases With Giant Magnetic-Field-Induced Strain," *IEEE Trans. Magn.*, vol. 38, no. 5, pp. 2814–2816, 2002.

[6] J. Y. Gauthier, A. Hubert, J. Abadie, and N. Chaillet, "Magnetic Shape Memory Alloy and Actuator Design," *Proc. 5th Int. Work. Microfactories*, pp. 3–6, 2006.

[7] I. Aaltio, Y. Ge, H. Pulkkinen, A. Sjöberg, O. Söderberg, X. W. Liu, and S. P. Hannula, "Crack growth of 10M Ni-Mn-Ga material in cyclic mechanical loading," *Phys. Procedia*, vol. 10, pp. 87–93, Jan. 2010.

[8] O. Heczko, V. Kopecky, L. Fekete, K. Jurek, J. Kopecek, L. Straka, and H. Seiner, "Magnetic Domains and Twin Microstructure of Single Crystal Ni-Mn-Ga Exhibiting Magnetic Shape Memory Effect," *IEEE Trans. Magn.*, vol. 51, no. 11, pp. 15–18, 2015.

[9] S. Barker, E. Rhoads, P. Lindquist, M. Vreugdenhill, and P. Müllner, "Micropump utilizing localized magnetic-field-induced deformation of MSM elements to deliver sub-microliter volumes of drugs to the rat brain," *Proc. Actuator*, pp. 96–97, 2014.

[10] Y. Ge, O. Heczko, O. Söderberg, and S.-P. Hannula, "Magnetic domain evolution with applied field in a Ni–Mn–Ga magnetic shape memory alloy," *Scr. Mater.*, vol. 54, no. 12, pp. 2155–2160, Jun. 2006.

[11] R. Chulist, E. Pagounis, A. Böhm, C. G. Oertel, and W. Skrotzki, "Twin boundaries in trained 10M Ni-Mn-Ga single crystals," *Scr. Mater.*, vol. 67, no. 4, pp. 364–367, Aug. 2012.

[12] H. Seiner, L. Straka, and O. Heczko, “A microstructural model of motion of macro-twin interfaces in Ni–Mn–Ga 10M martensite,” *J. Mech. Phys. Solids*, vol. 64, pp. 198–211, Mar. 2014.

[13] K. Vallal Peruman, M. Mahendran, S. Seenithurai, R. Chokkalingam, R. K. Singh, and V. Chandrasekaran, “Internal stress dependent structural transition in ferromagnetic Ni-Mn-Ga nanoparticles prepared by ball milling,” *J. Phys. Chem. Solids*, vol. 71, no. 11, pp. 1540–1544, Nov. 2010.

[14] T. Krenke, S. Aksoy, E. Duman, M. Acet, X. Moya, L. Mañosa, and A. Planes, “Hysteresis effects in the magnetic-field-induced reverse martensitic transition in magnetic shape-memory alloys,” *J. Appl. Phys.*, vol. 108, no. 4, p. 043914, 2010.

[15] L. Straka and O. Heczko, “Reversible 6% strain of Ni-Mn-Ga martensite using opposing external stress in static and variable magnetic fields,” *J. Magn. Magn. Mater.*, vol. 290–291, pp. 829–831, Apr. 2005.

[16] M. Zeng, S. W. Or, and H. L. W. Chan, “Magnetic field-induced strain and magnetoelectric effects in sandwich composite of ferromagnetic shape memory Ni-Mn-Ga crystal and piezoelectric PVDF polymer.,” *IEEE Trans. Ultrason. Ferroelectr. Freq. Control*, vol. 57, no. 10, pp. 2147–2153, 2010.

[17] R. Chulist, L. Straka, N. Lanska, A. Soroka, A. Sozinov, and W. Skrotzki, “Characterization of mobile type I and type II twin boundaries in 10M modulated Ni-Mn-Ga martensite by electron backscatter diffraction,” *Acta Mater.*, vol. 61, no. 6, pp. 1913–1920, Apr. 2013.

[18] D. Kellis, A. Smith, K. Ullakko, and P. Mullner, “Oriented single crystals of Ni-Mn-Ga with very low switching field,” *J. Cryst. Growth*, vol. 359, pp. 64–68, Nov. 2012.

[19] O. Heczko, “Determination of ordinary magnetostriction in Ni-Mn-Ga magnetic shape memory alloy,” *J. Magn. Magn. Mater.*, vol. 290–291, pp. 846–849, Apr. 2005.

[20] L. Straka, N. Lanska, K. Ullakko, and A. Sozinov, “Twin microstructure dependent mechanical response in Ni–Mn–Ga single crystals,” *Appl. Phys. Lett.*, vol. 96, no. 13, p. 131903, 2010.

[21] C. Bechtold, I. Teliban, C. Thede, S. Chemnitz, and E. Quandt, “Non-contact strain measurements based on inverse magnetostriction,” *Sensors Actuators, A Phys.*, vol. 158, no. 2, pp. 224–230, Mar. 2010.

[22] I. Suorsa, E. Pagounis, and K. Ullakko, “Position dependent inductance based on magnetic shape memory materials,” *Sensors Actuators, A Phys.*, vol. 121, pp. 136–141, May 2005.

[23] H. Schmidt, “Magneto-Mechanical Energy Conversion in Magnetic Shape Memory Alloys,” *J. Phys. Conf. Ser.*, vol. 303, p. 012078, 2011.

[24] “EtoMagnetic: Magnetic Shape Memory Technology (MAGNETOSHAPE).” [Online]. Available: http://etogroup.com/MAGNETOSHAPE_EN.html. [Accessed: 22-Mar-2016].

[25] W. Qu and J. Lu, “Model on Electromagnetic-mechanical Conversion of Magnetically Controlled Shape Memory Alloy,” *2011 Third Int. Conf. Meas. Technol. Mechatronics Autom.*, vol. 2, no. 3, pp. 591–594, Jan. 2011.

[26] A. Sozinov, A. A. Likhachev, and K. Ullakko, “Magnetic and Magnetomechanical Properties of Ni-Mn-Ga Alloys with easy axis and easy plane of magnetization,” *Smart Mater. Struct.*, vol. 4333, pp. 189–196, 2001.

[27] K. Rolfs, A. Mecklenburg, J.-M. Guldbakke, R. C. Wimpory, A. Raatz, J. Hesselbach, and R. Schneider, “Crystal quality boosts responsiveness of magnetic shape memory single crystals,” *J. Magn. Magn. Mater.*, vol. 321, no. 8, pp. 1063–1067, Apr. 2009.

[28] L. Straka, A. Soroka, and A. Sozinov, “Tailored magneto-mechanical response in Ni-Mn-Ga magnetic shape memory single crystals,” in *Proc. Actuator*, 2010, p. 727.

[29] U. Gaitzsch, M. Pötschke, S. Roth, N. Mattern, B. Rellinghaus, and L. Schultz, “Structure formation in martensitic NiMnGa MSM alloy,” *J. Alloys Compd.*, vol. 443, pp. 99–104, Sep. 2007.

[30] B. Reinholz, S. Brinckmann, A. Hartmaier, B. Muntifering, W. B. Knowlton, and P. Müllner, “Influence of the twin microstructure on the mechanical properties in magnetic shape memory alloys,” *Acta Mater.*, vol. 108, pp. 197–206, 2016.

[31] J. Y. G. Authier, C. L. Excellent, A. H. Ubert, J. A. Badie, and N. C. Haillet, “Modelling Rearrangement Process of Martensite Platelets in a Magnetic Shape Memory Alloy NiMnGa Single Crystal under Magnetic Field and (or) Stress Action,” *J. Intell. Mater. Syst. Struct.*, vol. 18, no. 3, pp. 289–299, 2007.

[32] B. Kiefer and D. C. Lagoudas, “Phenomenological modelling of ferromagnetic shape memory alloys,” *Proc. SPIE*, 2004.

[33] A. Sozinov, N. Lanska, A. Soroka, and L. Straka, “Highly mobile type II twin boundary in Ni-Mn-Ga five-layered martensite,” *Appl. Phys. Lett.*, vol. 99, no. 12, p. 124103, 2011.

[34] L. Straka, H. Hänninen, A. Soroka, and A. Sozinov, “Ni-Mn-Ga single crystals with very low twinning stress,” *J. Phys. Conf. Ser.*, vol. 303, p. 012079, Jul. 2011.

[35] I. Aaltio, O. Soderberg, Y. Ge, and S. P. Hannula, “Twin boundary nucleation and motion in Ni-Mn-Ga magnetic shape memory material with a low twinning stress,” *Scr. Mater.*, vol. 62, no. 1, pp. 9–12, Jan. 2010.

[36] L. Straka, O. Heczko, H. Seiner, N. Lanska, J. Drahokoupil, A. Soroka, S. Fähler, H. Hänninen, and A. Sozinov, “Highly mobile twinned interface in 10 M modulated Ni-Mn-Ga martensite: Analysis beyond the tetragonal approximation of lattice,” *Acta Mater.*, vol. 59, no. 20, pp. 7450–7463, Dec. 2011.

[37] E. Pagounis, M. Maier, and M. Laufenberg, “Properties of large Ni-Mn-Ga single crystals with a predominant 5M-martensitic structure,” *3rd Int. Conf. Ferromagn. Shape Mem. Alloy.*, pp. 207–208, 2011.

[38] T. Schiepp, M. Maier, E. Pagounis, and M. Laufenberg, “Modelling of actuators based on magnetic shape memory materials,” *Proc. Actuator*, 2012.

[39] O. Heczko, L. Straka, and H. Seiner, “Different microstructures of mobile twin boundaries in 10 M modulated Ni-Mn-Ga martensite,” *Acta Mater.*, vol. 61, no. 2, pp. 622–631, Jan. 2013.

[40] L. Straka, A. Soroka, H. Seiner, H. Hanninen, and A. Sozinov, “Temperature dependence of twinning stress of Type I and Type II twins in 10M modulated Ni-Mn-Ga martensite,” *Scr. Mater.*, vol. 67, no. 1, pp. 25–28, Jul. 2012.

[41] L. Riccardi, D. Naso, B. Turchiano, and H. Janocha, “Adaptive approximation-based control of hysteretic unconventional actuators,” *IEEE Conf. Decis. Control Eur. Control Conf.*, pp. 958–963, 2011.

[42] M. Ruderman and T. Bertram, “Discrete dynamic Preisach model for robust inverse control of hysteresis systems,” *49th IEEE Conf. Decis. Control*, pp. 3463–3468, 2010.

[43] N. Sarawate and M. Dapino, “Frequency Dependent Strain-Field Hysteresis Model for Ferromagnetic Shape Memory Ni–Mn–Ga,” *IEEE Trans. Magn.*, vol. 44, no. 5, pp. 566–575, 2008.

[44] “AdaptaMat Ltd.” [Online]. Available: www.adaptamat.com [Accessed: 01-Apr-2014].

[45] I. Suorsa and E. Pagounis, “Magnetic field-induced stress in the Ni–Mn–Ga magnetic shape memory alloy,” *J. Appl. Phys.*, vol. 95, no. 9, p. 4958, 2004.

[46] N. N. Sarawate and M. J. Dapino, “Magnetic-field-induced stress and magnetization in mechanically blocked Ni–Mn–Ga,” *J. Appl. Phys.*, vol. 103, no. 8, p. 083902, 2008.

[47] A. A. Likhachev, A. Sozinov, and K. Ullakko, “Modeling the strain response, magneto-mechanical cycling under the external stress, work output and energy losses in Ni-Mn-Ga,” *Mech. Mater.*, vol. 38, no. 5–6, pp. 551–563, May 2006.

[48] L. Straka and O. Heczko, “Superelastic Response of Ni – Mn – Ga Martensite in Magnetic Fields and a Simple Model,” *IEEE Trans. Magn.*, vol. 39, no. 5, pp. 3402–3404, 2003.

[49] V. A. Chernenko, M. Chmielus, and P. Müllner, “Large magnetic-field-induced strains in Ni–Mn–Ga nonmodulated martensite,” *Appl. Phys. Lett.*, vol. 95, p. 103103, 2009.

[50] I. Aaltio, “Role of twin boundary mobility in performance of the NiMnGa single crystals,” Doctorial Dissertation, 2011.

[51] L. Straka, H. Hänninen, and O. Heczko, “Temperature dependence of single twin boundary motion in Ni–Mn–Ga martensite,” *Appl. Phys. Lett.*, vol. 98, no. 14, p. 141902, 2011.

[52] O. Heczko and K. Ullakko, “Effect of Temperature on Magnetic Properties of Ni – Mn – Ga Magnetic Shape Memory (MSM) Alloys,” *IEEE Trans. Magn.*, vol. 37, no. 4, pp. 2672–2674, 2001.

[53] E. Pagounis, R. Chulist, M. J. Szczerba, and M. Laufenberg, “High-temperature magnetic shape memory actuation in a Ni–Mn–Ga single crystal,” *Scr. Mater.*, vol. 83, pp. 29–32, Jul. 2014.

[54] H. Gatzen, M. Hahn, and K. Ullakko, “Characterization of Magnetic Shape Memory (MSM) material and its application in a hybrid microactuator,” *Proc. Actuator*, 2006.

[55] W. J. Feng, L. Zuo, Y. B. Li, Y. D. Wang, M. Gao, and G. L. Fang, “Abnormal e/a-dependence of Tm and large inverse magnetocaloric effect in NiCuMnSb alloys,” *Mater. Sci. Eng. B Solid-State Mater. Adv. Technol.*, vol. 176, no. 8, pp. 621–625, May 2011.

[56] H. Karaca, I. Karaman, B. Basaran, Y. Chumlyakov, and H. Maier, “Magnetic field and stress induced martensite reorientation in NiMnGa ferromagnetic shape memory alloy single crystals,” *Acta Mater.*, vol. 54, no. 1, pp. 233–245, Jan. 2006.

[57] L. Straka, O. Heczko, and S. P. Hannula, “Temperature dependence of reversible field-induced strain in Ni-Mn-Ga single crystal,” *Scr. Mater.*, vol. 54, no. 8, pp. 1497–1500, Apr. 2006.

[58] H. Scmidt and E. Quantd, “Magnetically induced shape-change in solids and its use in actuators,” *Proc. Actuator*, p. 289, 2010.

[59] Y. W. Lai, R. Schafer, L. Schultz, and J. McCord, “Direct observation of AC field-induced twin-boundary dynamics in bulk NiMnGa,” *Acta Mater.*, vol. 56, no. 18, pp. 5130–5137, Oct. 2008.

[60] A. Neudert, Y. W. Lai, R. Schafer, and J. McCord, “Twin boundary motion in NiMnGa upon pulsed field excitation,” *Proc. Actuator*, p. 762, 2010.

[61] R. Techapiesancharoenkij, J. Kostamo, S. M. Allen, and R. C. O'Handley, "The effect of magnetic stress and stiffness modulus on resonant characteristics of NiMnGa ferromagnetic shape memory alloy actuators," *J. Magn. Magn. Mater.*, vol. 323, no. 23, pp. 3109–3116, Dec. 2011.

[62] J. Tellinen, I. Suorsa, I. Aaltio, and K. Ullakko, "Basic Properties Of Magnetic Shape Memory Actuators," in *Proc. Actuator*, 2002, pp. 10–12.

[63] M. Mahendran, R. S. Pandi, R. Chokkalingam, R. Kodipandyan, K. V. Peruman, and S. Seenithurai, "Acoustic Attenuation in Ferromagnetic Shape Memory Alloy Polymer Composites," *MEMS, NANO, Smart Syst. (ICMENS), Fifth Int. Conf.*, pp. 8–11, 2009.

[64] R. Techapiesancharoenkij, J. Kostamo, S. M. Allen, and R. C. O'Handley, "Frequency response of acoustic-assisted Ni–Mn–Ga ferromagnetic-shape-memory-alloy actuator," *J. Appl. Phys.*, vol. 105, no. 9, p. 093923, 2009.

[65] A. Oonishi, K. Hirata, B. Yoo, and N. Niguchi, "Frequency response characteristics for linear actuator made by NiMnGa shape memory alloy," *Int. J. Appl. Electromagn. Mech.*, vol. 39, pp. 913–918, 2012.

[66] M. A. Marioni, R. C. O'Handley, S. M. Allen, S. R. Hall, D. I. Paul, M. L. Richard, J. Feuchtwanger, B. W. Peterson, J. M. Chambers, and R. Techapiesancharoenkij, "The ferromagnetic shape-memory effect in Ni-Mn-Ga," *J. Magn. Magn. Mater.*, vol. 290–291, pp. 35–41, Apr. 2005.

[67] E. Pagounis and E. Quantd, "Recent advances and challenges in magnetic shape memory meterials," *Proc. Actuator*, 2006.

[68] M. A. Marioni, R. C. O'Handley, and S. M. Allen, "Pulsed magnetic field-induced actuation of Ni–Mn–Ga single crystals," *Appl. Phys. Lett.*, vol. 83, no. 19, p. 3966, 2003.

[69] H. E. Karaca, I. Karaman, B. Basaran, D. C. Lagoudas, Y. I. Chumlyakov, and H. J. Maier, "One-way shape memory effect due to stress-assisted magnetic field-induced phase transformation in Ni_2MnGa magnetic shape memory alloys," *Scr. Mater.*, vol. 55, no. 9, pp. 803–806, Nov. 2006.

[70] I. Karaman, H. E. Karaca, B. Basaran, D. C. Lagoudas, Y. I. Chumlyakov, and H. J. Maier, "Stress-assisted reversible magnetic field-induced phase transformation in NiMnGa magnetic shape memory alloys," *Scr. Mater.*, vol. 55, no. 4, pp. 403–406, Aug. 2006.

[71] S. Y. Yang, Y. Liu, C. P. Wang, Z. Shi, and X. J. Liu, "The mechanism clarification of Ni-Mn-Fe-Ga alloys with excellent and stable functional properties," *J. Alloys Compd.*, vol. 560, pp. 84–91, May 2013.

[72] R. F. Hamilton, S. Dilibal, H. Sehitoglu, and H. J. Maier, “Underlying mechanism of dual hysteresis in NiMnGa single crystals,” *Mater. Sci. Eng. A*, vol. 528, no. 3, pp. 1877–1881, Jan. 2011.

[73] I. Aaltio, A. Soroka, Y. Ge, O. Söderberg, and S.-P. Hannula, “High-cycle fatigue of 10M Ni–Mn–Ga magnetic shape memory alloy in reversed mechanical loading,” *Smart Mater. Struct.*, vol. 19, no. 7, p. 075014, Jul. 2010.

[74] T. Lawrence, P. Lindquist, K. Ullakko, and P. Müllner, “Fatigue life and fracture mechanics of unconstrained Ni–Mn–Ga single crystals in a rotating magnetic field,” *Mater. Sci. Eng. A*, vol. 654, pp. 221–227, 2016.

[75] J. Lu, Z. Liang, and W. Qu, “Optimal Design of Rotating Actuators Made by Magnetically Controlled Shape Memory Alloy,” *2009 Ninth Int. Conf. Hybrid Intell. Syst.*, pp. 95–98, 2009.

[76] T. Schiepp, M. Maier, E. Pagounis, and M. Laufenberg, “Controlling Dynamic Behaviour of Magnetic Shape Memory Based Actuators,” *Proc. Actuator*, pp. 116–118, 2014.

[77] T. Schiepp, “A Simulation Method for Design and Development of Magnetic Shape Memory Actuators,” Doctorial dissertation, 2015.

[78] T. Schiepp, M. Maier, E. Pagounis, A. Schlüter, and M. Laufenberg, “FEM-Simulation of Magnetic Shape Memory Actuators,” *IEEE Trans. Magn.*, vol. 50, no. 2, p. 7024504, 2014.

[79] B. Krevet and M. Kohl, “FEM simulation of a Ni-Mn-Ga film bridge actuator,” *Phys. Procedia*, vol. 10, pp. 154–161, Jan. 2010.

[80] B. Holz, H. Janocha, and L. Riccardi, “Compact MSM Actuators – Concept for Highest Force Exploitation,” *Proc. Actuator*, 2012.

[81] B. Holz and H. Janocha, “MSM Actuators – Magnetic circuit concepts and operating modes,” *Proc. Actuator*, p. 307, 2010.

[82] B. Holz, L. Riccardi, H. Janocha, and D. Naso, “MSM Actuators: Design Rules and Control Strategies,” *Adv. Eng. Mater.*, vol. 14, no. 8, pp. 668–681, Aug. 2012.

[83] B. Spasova, M. C. Wurz, C. Ruffert, J. Norpoth, and H. H. Gatzen, “Using Magneto-Optical Measurements for the Evaluation of a Hybrid Magnetic Shape Memory (MSM)-Based Microactuator,” *IEEE Trans. Magn.*, vol. 46, no. 6, pp. 2256–2259, 2010.

[84] K. Wegener, P. Blumenthal, and A. Raatz, “Development of a miniaturized clamping device driven by magnetic shape memory alloys,” *J. Intell. Mater. Syst. Struct.*, vol. 0, no. 0, pp. 1–7, Oct. 2013.

[85] L. Riccardi, D. Naso, B. Turchiano, and H. Janocha, “Robust adaptive control of a magnetic shape memory actuator for precise positioning,” *Proc. Am. Control Conf. O’Farrell Str.*, p. 5400, 2011.

[86] Z. Qingxin, Z. Hongmei, L. Yibo, and Z. Jing, “On a novel self-sensing actuator,” *Proc. 27th Chinese Control Conf.*, pp. 257–260, 2008.

[87] A. Niskanen and A. Soroka, “Proportional Control and Self-Sensing in a Magnetic Shape Memory (MSM) Alloy Actuator,” *Proc. Actuator*, 2012.

[88] C. Lin, Y. Wei, and F. Dong, “Concept Design and Experiment Study of Self-Sensing Actuator Based on Magnetically Controlled Shape Memory Alloy,” *Proc. Meas. Technol. Mechatronics Autom. (ICMTMA), Int. Conf.*, no. 111, pp. 812–815, Mar. 2010.

[89] C. Lin, Y. Wei, H. Zheng, and J. Lu, “Study on self-sensing actuator of magnetically controlled shape memory alloy,” *Proc. 9th Int. Conf. Electron. Meas. Instruments*, pp. 777–780, 2009.

[90] V. A. Chernenko, V. A. L, M. Pasquale, S. Besseghini, C. Sasso, and D. A. Polenur, “Magnetoelastic behavior of Ni-Mn-Ga martensitic alloys,” *Int. J. Appl. Electromagn. Mech.*, vol. 12, pp. 3–8, 2000.

[91] F. Wang, W. Li, Q. Zhang, and X. Wu, “Operation principle and design of a differential magnetic shape memory actuator,” in *Proc. IAS*, 2005, pp. 2114–2118.

[92] Q. Zhang and F. Wang, “A Novel Linear Actuator and Its Controlling System,” *Proc. IEEE Int. Conf. Aut. Logi.*, pp. 979–984, 2007.

[93] E. Gans and G. P. Carman, “Cyclic actuation of Ni–Mn–Ga composites,” *J. Appl. Phys.*, vol. 99, no. 8, p. 084905, 2006.

[94] I. Suorsa, J. Tellinen, K. Ullakko, and E. Pagounis, “Voltage generation induced by mechanical straining in magnetic shape memory materials,” *J. Appl. Phys.*, vol. 95, no. 12, pp. 8054–8058, 2004.

[95] A. Niskanen, “Magnetic Shape Memory (MSM) Alloys for Energy Harvesting and Sensing Applications,” 2012. [Online]. Available: http://wsn.aalto.fi/en/activities/workshops/wowss2012/adaptamat_abstract.pdf.

[96] M. Gueltig, B. Haefner, M. Kohl, and M. Ohtsuka, “Thermal energy harvesting based on ferromagnetic shape memory alloy microactuation,” *Proc. Transducers*, pp. 2803–2806, 2013.

[97] L. Jun and W. Ling, “Inverse Characteristics of Magnetically Controlled Shape Memory Alloy under External Force,” *Proc. Int. Conf. Optoelectron. Image Process.*, pp. 655–658, Nov. 2010.

[98] I. Karaman, B. Basaran, H. E. Karaca, A. I. Karsilayan, and Y. I. Chumlyakov, “Energy harvesting using martensite variant reorientation mechanism in a NiMnGa magnetic shape memory alloy,” *Appl. Phys. Lett.*, vol. 90, no. 17, p. 172505, 2007.

[99] M. Mahendran, J. Feuchtwanger, R. Techapiesancharoenkij, D. Bono, and R. C. O’Handley, “Acoustic energy absorption in NiMnGa/polymer composites,” *J. Magn. Magn. Mater.*, vol. 323, no. 8, pp. 1098–1100, Apr. 2011.

[100] W. H. Wang, G. D. Liu, and G. H. Wu, “Magnetically controlled high damping in ferromagnetic NiMnGa single crystal,” *Appl. Phys. Lett.*, vol. 89, no. 10, p. 101911, 2006.

[101] S.-P. Hannula, I. Aaltio, Y. Ge, M. Lahelin, and O. Söderberg, “Processing and properties of Ni–Mn–Ga magnetic shape memory alloy based hybrid materials,” *Curr. Appl. Phys.*, vol. 12, pp. S63–S67, Sep. 2012.

[102] I. Aaltio, K. P. Mohanchandra, O. Heczko, M. Lahelin, Y. Ge, G. P. Carman, O. Soderberg, B. Lafgren, J. Seppala, and S. P. Hannula, “Temperature dependence of mechanical damping in Ni-Mn-Ga austenite and non-modulated martensite,” *Scr. Mater.*, vol. 59, no. 5, pp. 550–553, Sep. 2008.

[103] J. Van Humbeeck and S. Kustov, “Active and passive damping of noise and vibrations through shape memory alloy,” *Smart Mater. Struct.*, vol. 14, no. 5, pp. S171–S185, 2005.

[104] F. Fiorillo and I. Mayergoyz, *Characterization and Measurement of Magnetic Materials*. Academic Press, 2004.

[105] K. Matsunaga, N. Niguchi, and K. Hirata, “Study on Starting Performance of Ni-Mn-Ga Magnetic Shape Memory Alloy Linear Actuator,” *IEEE Trans. Magn.*, vol. 49, no. 5, pp. 2225–2228, 2013.

[106] J. C. Maxwell, “On Physical Lines of Force,” *Philos. Mag. J. Sci.*, In Fours Parts, 1861.

[107] G. Lancaster, *Introduction to Fields and Circuits*. New: Oxford University Press, 1992.

[108] “ANSYS 14.5 Therory Reference.”

[109] P. P. Silverster and R. L. Ferrari, *Finite elements for electrical engineers*. Cambridge: Press Syndicate of the University of Cambridge, 1983.

[110] J. Pointer, “Understanding Accuracy and Discretization Error in an FEA Model,” *ANSYS Users Conf.*, 2004.

[111] P. Diez and J. P. Webb, “A Rational Approach to B – H Curve Representation,” *IEEE Trans. Magn.*, vol. 52, no. 3, p. 7203604, 2016.

[112] A. A. Likhachev and K. Ullakko, “Quantitative Model of Large Magnetostrain Effect in Ferromagnetic Shape Memory Alloys,” *EPJdirect*, vol. B2, pp. 1–9, 1999.

[113] Y. Zhu and G. Dui, “Model for field-induced reorientation strain in magnetic shape memory alloy with tensile and compressive loads,” *J. Alloys Compd.*, vol. 459, no. 1–2, pp. 55–60, Jul. 2008.

[114] C. M. Landis, “A continuum thermodynamics formulation for micro-magnetomechanics with applications to ferromagnetic shape memory alloys,” *J. Mech. Phys. Solids*, vol. 56, no. 10, pp. 3059–3076, Oct. 2008.

[115] E. Faran and D. Shilo, “The kinetic relation for twin wall motion in NiMnGa,” *J. Mech. Phys. Solids*, vol. 59, pp. 975–987, 2011.

[116] E. Faran and D. Shilo, “The kinetic relation for twin wall motion in NiMnGa - Part 2,” *J. Mech. Phys. Solids*, vol. 61, no. 3, pp. 726–741, May 2013.

[117] J. Y. Gauthier, A. Hubert, J. Abadie, N. Chaillet, and C. Lexcellent, “Nonlinear Hamiltonian modelling of magnetic shape memory alloy based actuators,” *Sensors Actuators, A Phys.*, vol. 141, no. 2, pp. 536–547, Feb. 2008.

[118] A. N. Bogdanov, A. DeSimone, S. Müller, and U. K. Rößler, “Phenomenological theory of magnetic-field-induced strains in ferromagnetic shape-memory materials,” *J. Magn. Magn. Mater.*, vol. 261, no. 1–2, pp. 204–209, Apr. 2003.

[119] J. Ziske, F. Ehle, H. Neubert, A. D. Price, and J. Lienig, “A Simple Phenomenological Model for Magnetic Shape Memory Actuators,” *IEEE Trans. Magn.*, vol. 51, no. 1, p. 4002608, 2015.

[120] K. . Haldar, B. . Kiefer, and D. C. . Lagoudas, “Finite element analysis of the demagnetization effect and stress inhomogeneities in magnetic shape memory alloy samples,” *Philos. Mag.*, vol. 91, no. 32, pp. 4126–4157, Nov. 2011.

[121] K. Haldar, G. Chatzigeorgiou, and D. C. Lagoudas, “Single crystal anisotropy and coupled stability analysis for variant reorientation in Magnetic Shape Memory Alloys,” *Eur. J. Mech. - A/Solids*, vol. 54, pp. 53–73, 2015.

[122] “Finite Element Method Magnetics.” [Online]. Available: http://www.femm.info/wiki/HomePage. [Accessed: 22-Mar-2016].

[123] M. Nayfeh and M. Brussel, *Electricity and Magnetism*. New York: John Wiley & Sons, 1985.

[124] O. Heczko, D. Vokoun, V. Kopecky, and M. Beleggia, “Effect of magnetostatic interactions on twin boundary motion in NiMnGa Magnetic Shape Memory Alloy,” *IEEE Magn. Lett.*, vol. 6, pp. 1–4, 2015.

[125] O. Heczko, L. Straka, and S.-P. Hannula, “Stress dependence of magnetic shape memory effect and its model,” *Mater. Sci. Eng. A*, vol. 438–440, pp. 1003–1006, Nov. 2006.

[126] E. Pagounis and P. Müllner, “Recent Developments in Magnetic Shape Memory Actuation,” in *Proc. Actuator*, 2014, pp. 86–91.

[127] A. Likhachev and K. Ullakko, “The model development and experimental investigation of giant magneto-mechanical effects in Ni-Mn-Ga,” *J. Magn. Magn. Mater.*, vol. 230, pp. 1541–1543, 2001.

[128] S. Flaga, J. Pluta, and B. Sapinski, “Pneumatic Valves Based on Magnetic Shape Memory Alloys : Potential Applications,” in *Proc. 12th ICCC*, 2011, pp. 111–114.

[129] D. Ireneusz and S. Flaga, “Characteristics of the flow control valve with MSMA actuator,” in *Proc. 15th ICCC*, 2014, pp. 192–195.

[130] “MagWeb - your source Magnetic Material Data.” [Online]. Available: http://magweb.us/free-bh-curves/. [Accessed: 04-Jul-2015].

[131] K. Kajan, “Finite Element Modelling and Invesigation of High Speed, Large Force and Long Lifetime Electromagnetic Actuators,” Doctoral Dissertation, 2009.

[132] A. Ivanov-Smolensky, *Electrical Machines*. Moscow: MPEI Publishing (in russian), 2006.

[133] “Goodfellow: Materials for Scientific Research and Manufacturing.” [Online]. Available: www.goodfellow.com. [Accessed: 28-Mar-2016].

[134] N. N. Sarawate and M. J. Dapino, “Stiffness Tuning with Bias Magnetic Fields in Ferromagnetic Shape Memory Ni-Mn-Ga,” *J. Intell. Mater. Syst. Struct.*, vol. 20, no. 13, pp. 1625–1634, Jun. 2009.

[135] L. Riccardi, T. Schiepp, B. Holz, M. Maier, H. Janocha, and M. Laufenberg, “A Modular, Energy Efficient Actuator Based on Magnetic Shape Memory Alloys,” in *Proc. Actuator*, 2014, pp. 112–115.

[136] G. Stone, I. Culbert, E. Boulter, and H. Dhirani, *Electrical Insulation for Rotating Machines: Design, Evaluation, Aging, Testing, and Repair*, 2nd ed. USA: Wiley-IEEE Press, 2014.

[137] Y. Späck-Leigsnering, “Modeling and Simulation of a Station Class Surge Arrester,” Master Thesis, 2014.

[138] L. E. Faidley, M. J. Dapino, G. N. Washington, and T. A. Lograsso, “Modulus Increase with Magnetic Field in Ferromagnetic Shape Memory Ni-Mn-Ga,” *J. Intell. Mater. Syst. Struct.*, vol. 17, no. 2, pp. 123–131, Feb. 2006.

Appendix 1. Evaluation of n-τ components of magnetic field vectors at a twin boundary

For the orientation of fields lines Fig. 4.3-7 and the magnetic field known from the modelling

$$B_{hx} = 0.0335 \cdot T;\ B_{hy} = -0.1585 \cdot T;\ H_{hx} = 13.35 \cdot \frac{kA}{m};\ H_{hy} = -2.53 \cdot \frac{kA}{m}$$

$$B_{ex} = 0.2107 \cdot T;\ B_{ey} = 0.0187 \cdot T;\ H_{ex} = 3.37 \cdot \frac{kA}{m};\ H_{ey} = 7.45 \cdot \frac{kA}{m}$$

Eq. (4.3-5) yields:

$$B_h = 0.1619 \cdot T; H_h = 13.59 \cdot \frac{kA}{m};\ \ B_e = 0.2116 \cdot T;\ H_e = 8.17 \cdot \frac{kA}{m}$$

Eq. (3.1-7) yields:

$$\mu_{hx} = \frac{B_{hx}}{\mu_0 \cdot H_{hx}} = \frac{0.0335 \cdot T}{4\pi \cdot 10^{-7} \cdot 13.35 \cdot \frac{kA}{m}} = 2, similarly\ \mu_{hy} = 50, \mu_{ex} = 50, \mu_{ey} = 2$$

This is consistent with the basic theory due to magnetic anisotropy of twin variants. However, values of permeability of MSM twin variants calculated using total values of magnetic field vectors are

$$\mu_h = \frac{B_h}{\mu_0 \cdot H_h} = \frac{0.1619 \cdot T}{4\pi \cdot 10^{-7} \cdot 13.59 \cdot \frac{kA}{m}} = 9.5$$

$$\mu_e = \frac{B_e}{\mu_0 \cdot H_e} = \frac{0.2116 \cdot T}{4\pi \cdot 10^{-7} \cdot 8.17 \cdot \frac{kA}{m}} = 20.6$$

As discussed in Chapter 4, “total” MSM permeability does not lie on axes B-H curves.

Its general relation to axes permeability values is

$$\mu_m = \sqrt{\frac{(\mu_x\mu_y)^2 \cdot \left(B_x^2 + B_y^2\right)}{(\mu_x B_x)^2 + \left(\mu_y B_y\right)^2}}$$

Such a complicated relation makes it inapplicable in simplistic equivalent circuit models. Normal and tangential components of magnetic field vectors are

$$B_{en} = B_e \cdot cos\left(\frac{\pi}{4} + \text{acos}\frac{B_{ex}}{B_e}\right) = 0.2116 \cdot T \cdot cos\left(\frac{\pi}{4} + \text{acos}\frac{0.2107}{0.2116}\right) = 0.1358 \cdot T$$

$$B_{hn} = B_h \cdot cos\left(\frac{\pi}{4} - \text{acos}\frac{\left|B_{hy}\right|}{B_h}\right) = 0.1619 \cdot T \cdot cos\left(\frac{\pi}{4} - \text{acos}\frac{0.1585}{0.1619}\right) = 0.1358 \cdot T$$

$$H_{e\tau} = H_e \cdot cos\left(\frac{\pi}{4} - \text{acos}\frac{H_{ex}}{H_e}\right) = 8.17\frac{kA}{m} \cdot cos\left(\frac{\pi}{4} - \text{acos}\frac{3.37}{8.17}\right) = 7.65\frac{kA}{m}$$

$$H_{h\tau} = -H_h \cdot cos\left(\frac{\pi}{4} + \text{acos}\frac{\left|H_{hy}\right|}{H_h}\right) = -13.59\frac{kA}{m} \cdot cos\left(\frac{\pi}{4} + \text{acos}\frac{2.53}{13.59}\right) = 7.65\frac{kA}{m}$$

Continuity of normal component of flux density and tangential component of field intensity checks out.

Appendix 2. Average (equivalent) MSM permeability calculation

Illustration of the analysis discussed in Section 4.3.3. Several examples

For all models $F_\delta = 28A$, $a_m = 1mm$, $\delta = 0.2mm$.

For $\varepsilon = 0.014$ (1.4%), $B_\delta = 0.0737\ T$

$$\mu_m = \frac{B_\delta \cdot a_m \cdot (1-\varepsilon)}{F_\delta \cdot \mu_0 - B_\delta \cdot (\delta + a_m \cdot \varepsilon)} = \frac{0.0737 \cdot 1 \cdot (1-0.014)}{28 \cdot 4\pi \cdot 10^{-7} - 0.0737 \cdot (0.2 + 1 \cdot 0.014)} = 3.7$$

For $\varepsilon = 0.029$ (2.9%), $B_\delta = 0.106\ T$

$$\mu_m = \frac{0.106 \cdot 1 \cdot (1-0.029)}{28 \cdot 4\pi \cdot 10^{-7} - 0.106 \cdot (0.2 + 1 \cdot 0.029)} = 9.4$$

For $\varepsilon = 0.053$ (5.3%), $B_\delta = 0.125\ T$

$$\mu_m = \frac{0.125 \cdot 1 \cdot (1-0.053)}{28 \cdot 4\pi \cdot 10^{-7} - 0.125 \cdot (0.2 + 1 \cdot 0.053)} = 33$$

Appendix 3. MSM actuator performance evaluation and optimisation algorithm

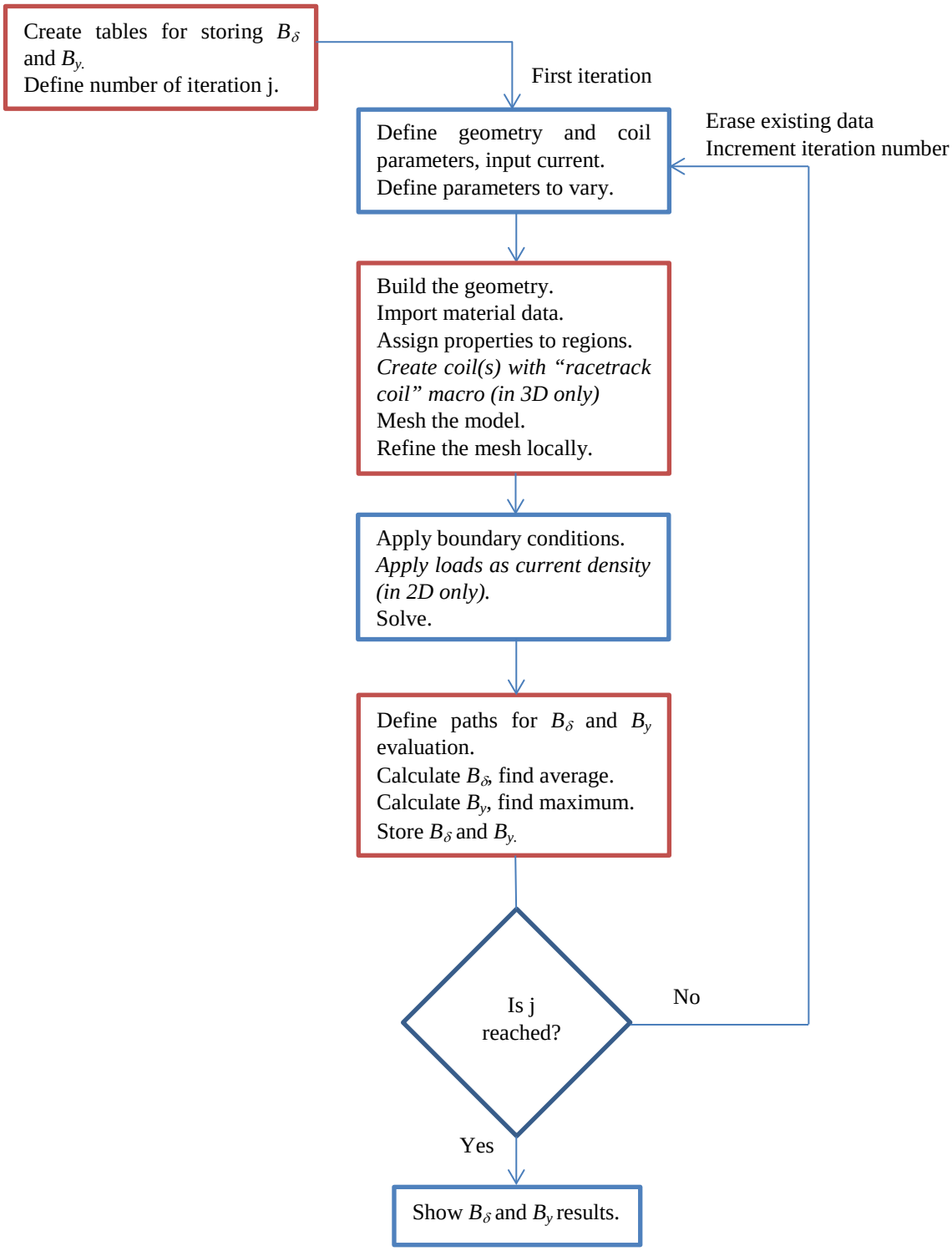

Figure A3-1. ANSYS Multiphysics electromagnetic modelling algorithm

Appendix 4. ANSYS 3D electromagnetic analysis codes

R actuator, final strain

```
/prep7
edd=1 !number of experiments in the cycle
*DIM,Bair[3],,edd, !array for storing average flux density
*DIM,Bcore[4],,edd, !array for storing maximum core flux density
*do,j,1,edd,1
/com, ! Set parameter values for analysis
ic=-3
wc[5]=140
af=11.9
bf=23
ay=3.7
hy=5.0
nt=50 !total number of bands
lme=0.106
ne=18
lmh=0.1
nh=nt-ne
lm=ne*lme+nh*lmh
lz=6.7
e=(ne/nt)*0.06 !relative strain
am=1*(1-e)
da=(1.2-am)/2
ac=4.3
bc=8
murme=50 !to be replaced with BH curves
murmh=2
aa=af-2*ay
adm=(af-2*ay-2*da-am)*0.5
bdm=lm
ach=bf-hy-bdm
jc=1000000*(ic*wc)/(ac*bc)
rad=0.5+bc/2
ex=60
/PNUM,VOLU,1
BLOCK,0,af,0,bf,0,lz
BLOCK,ay,ay+aa,bdm,bdm+ach,0,lz
BLOCK,ay+adm+da,ay+adm+da+am,0,lm+0,0,0+lz
BLOCK,adm+ay,ay+adm+am+2*da,0,lm+2*0,0,lz
VOVLAP,ALL
```

---

[3] This parameter is referred to as B_δ throughout this Thesis
[4] This parameter is referred to as B_y throughout this Thesis
[5] This parameter is referred to as N_c throughout this Thesis

```
NUMCMP,VOLU
VPLOT
K,51,(af-am)/2,0.08,0
K,52,(af-am)/2,0.08+0.1,0
K,53,(af+am)/2,1.08,0
K,54,(af+am)/2,1.08+0.1,0
a,51,53,54,52 !anti-clockwise
VOFFST,1,6.7,
VGEN,20,6,6,0,0,0.1+0.106,0,,,
BLOCK,0,ay,bf-hy,bf-hy-0.1,0,lz
VOVLAP,ALL
NUMCMP,VOLU
VPLOT
VADD,45,42,46,47
NUMCMP,VOLU
VPLOT
ET,1,SOLID96
MP,MURX,1,1
MP,MURX,2,0
MP,MURX,3,murmh
MP,MURX,4,1
MP,MURX,5,murme
MP,MURX,6,1
MAT,2
/UNITS,SI
/MPLIB,READ,DEFAULT
MPREAD,nl-core-R,,,LIB !import steel BH curve
MAT,3
MPREAD,MSMh2axes,,,LIB !import hard variant data
MAT,5
MPREAD,MSMe2axes,,,LIB !import easy variant data
VSEL,S,VOLU,,44
VATT,1,1,1
VSEL,S,VOLU,,42,43
VATT,2,1,1
VSEL,S,VOLU,,21,41
VATT,3,1,1 !hard
VSEL,S,VOLU,,1,20
VATT,5,1,1 !easy
ALLSEL,ALL
BLOCK,-ex,af+ex,-ex,bf+ex,-ex,lz+ex
VOVLAP,ALL
VPLOT
VSEL,S,VOLU,,46
VATT,6,1,1
/PNUM,MAT,1
ALLSEL,ALL
VPLOT
VLSCALE,ALL,,,.001,.001,.001,,,1
MAT,4
local,12,0,af/2000,(2*bf-hy)/2000,lz/2000,0,180,90
wpcsys,-1
race,(lz+2*rad)/2000,(hy+2*rad)/2000,rad/1000,ic*wc,bc/1000,ac/1
000,,,'coil-'
```

```
/psymb,csys,0
ALLSEL,ALL
NUMCMP,ALL
MSHAPE,1,3D
SMRTSIZE,1
VMESH,ALL
eplot
/SOLU
d,1,mag,0
ALLSEL,ALL
magsolv,3,,,,100,1
SOLVE
/post1
CSYS,0
PATH,ag-c,2,30,100
PPATH,1,,0.5*(af-am-0.04)*0.001,(bdm)*0.001,lz/2000,lz/2000
PPATH,2,,0.5*(af-am-0.04)*0.001,(bdm-lm)*0.001,lz/2000,lz/2000
PDEF,Bd,B,X,NOAV
PCALC,INTG,Bdav,Bd,S,1/(lm*0.001),
*get,Bdmm,PATH,0,MAX,Bdav,
*VFILL,Bair(j),DATA,Bdmm,
PATH,ayz,2,30,100
PPATH,1,,0.5*ay*0.001,(bf*0.5)*0.001,0
PPATH,2,,0.5*ay*0.001,(bf*0.5)*0.001,lz/1000
PDEF,Bayz,B,SUM,NOAV
*get,Bfe,PATH,0,MAX,Bayz,
*VFILL,Bcore(j),DATA,Bfe,
FINISH
*IF,j,LT,edd,THEN
/prep7
CSYS,0
ALLSEL,ALL
VCLEAR,ALL
ALLSEL,ALL
EDELE,ALL
ALLSEL,ALL
VDELE,ALL,,,1
wpcsys,-1
*enddo
*else
*enddo
*STATUS,Bair
*STATUS,Bcore
```

Geometry input for RU

(only parameters different from the above are listed)

```
lyz=50 !extended core length
lmz=6.7 !MSM element length
lzo=(lyz-lmz)/2

BLOCK,0,af,0,bf,0,lyz
BLOCK,ay,ay+aa,bdm,bdm+ach,0,lyz
BLOCK,ay+adm+da,ay+adm+da+am,0,lm+0,(lyz-lmz)/2,(lyz+lmz)/2
BLOCK,adm+ay,ay+adm+am+2*da,0,lm+2*0,(lyz-lmz)/2,(lyz+lmz)/2
BLOCK,ay,af-ay,0,lm+0,0,0+lzo
BLOCK,ay,af-ay,0,lm+0,lyz,lyz-lzo
BLOCK,0.05+af/2,-0.05+af/2,bf-hy,bf,0,lyz

VOVLAP,ALL
NUMCMP,VOLU
VPLOT
VADD,5,6,9,2,3,4
NUMCMP,VOLU
VPLOT
K,71,(af-am)/2,0.2,lzo
K,72,(af-am)/2,0.2+0.1,lzo
K,73,(af+am)/2,1.2,lzo
K,74,(af+am)/2,1.2+0.1,lzo
a,71,73,74,72 !anti-clockwise
VOFFST,1,lmz,
VGEN,18,5,5,0,0,0.1+0.106,0,,,
VOVLAP,ALL
VPLOT
```

2HiU actuator, varying N_c cycle

```
/prep7
edd=4 !number of experiments in the cycle
*DIM,Bair,,edd,
*DIM,Bcore,,edd,
*do,j,1,edd,1 !j increments each experiment
/com,
ic=3
wc=112-2*j !depends on j !total in 2 coils
af=6.2
bf=30
ay=0.5
hy=2.0
hcc=0
nt=50
lme=0.106
ne=18
lmh=0.1
nh=nt-ne
```

```
lm=ne*lme+nh*lmh
lz=6.7
lyy=25
e=(ne/nt)*0.06
am=1*(1-e)
da=(1.2-am)/2
ac=1.9
bc=7.9
acc=(af-am-2*da-2*ay)/2
murme=50 !to be replaced with BH curves
murmh=2
aa=af-2*ay
adm=(af-2*ay-2*da-am)*0.5
bdm=lm
ach=bf-hy-bdm
jc=1000000*(ic*wc)/(ac*bc)
rad=0.5+bc/2
ex=50
/PNUM,VOLU,1
BLOCK,0,af,0,bf,0,lm
BLOCK,ay,af-ay,bf-hy,(bf+lz)*0.5,0,lm
BLOCK,ay,af-ay,0+hy,(bf-lz)*0.5,0,lm
BLOCK,-da+(af-am)*0.5,(af-am)*0.5,(bf-lz)*0.5,(bf+lz)*0.5,0,lm
BLOCK,+da+(af+am)*0.5,(af+am)*0.5,(bf-lz)*0.5,(bf+lz)*0.5,0,lm
VOVLAP,ALL
NUMCMP,VOLU
VPLOT
K,51,(af-am)/2,(bf-lz)*0.5,0.08
K,52,(af-am)/2,(bf-lz)*0.5,0.08+0.1
K,53,(af+am)/2,(bf-lz)*0.5,1.08
K,54,(af+am)/2,(bf-lz)*0.5,1.08+0.1
a,51,53,54,52 !anti-clockwise
VOFFST,1,-6.7,
VGEN,20,7,7,0,0,0,0.1+0.106,,,
BLOCK,(af-0.1)*0.5,(af+0.1)*0.5,bf,bf-hy,0,lm
BLOCK,(af-0.1)*0.5,(af+0.1)*0.5,0,hy,0,lm
VOVLAP,ALL
NUMCMP,VOLU
VPLOT
VADD,21,49,48,22,46,47
NUMCMP,VOLU
VPLOT
BLOCK,0,af,0,bf,lm,(lyy+lm)/2
BLOCK,ay,af-ay,hy,bf-hy,lm,(lyy+lm)/2
BLOCK,0,af,0,bf,0,-(lyy-lm)/2
BLOCK,ay,af-ay,hy,bf-hy,0,-(lyy-lm)/2
BLOCK,(af-0.1)*0.5,(af+0.1)*0.5,bf,bf-hy,lm,(lyy+lm)/2
BLOCK,(af-0.1)*0.5,(af+0.1)*0.5,0,hy,lm,(lyy+lm)/2
BLOCK,(af-0.1)*0.5,(af+0.1)*0.5,bf,bf-hy,0,-(lyy-lm)/2
BLOCK,(af-0.1)*0.5,(af+0.1)*0.5,0,hy,0,-(lyy-lm)/2
VOVLAP,ALL
VADD,57,59,61
VADD,58,60,62
VADD,64,56,54,53,55,63,44
```

```
NUMCMP,VOLU
VPLOT
ET,1,SOLID96
MP,MURX,1,1
MP,MURX,2,0
MP,MURX,3,murmh
MP,MURX,4,1
MP,MURX,5,murme
MP,MURX,6,1 !outside air
MAT,2
/UNITS,SI
/MPLIB,READ,DEFAULT
MPREAD,nl-core-Hi,,,LIB
MAT,3
MPREAD,MSMh2axes,,,LIB
MAT,5
MPREAD,MSMe2axes,,,LIB
VSEL,S,VOLU,,44
VATT,1,1,1
VSEL,S,VOLU,,42,43
VATT,2,1,1
VSEL,S,VOLU,,21,41
VATT,3,1,1 !hard
VSEL,S,VOLU,,1,20
VATT,5,1,1 !easy
ALLSEL,ALL
BLOCK,-ex,af+ex,-ex,bf+ex,-ex-(lyy-lm)/2,ex+(lyy+lm)/2
VOVLAP,ALL
VPLOT
VSEL,S,VOLU,,46
VATT,6,1,1
/PNUM,MAT,1
ALLSEL,ALL
VPLOT
VLSCALE,ALL,,,.001,.001,.001,,,1
MAT,4
local,12,0,(af-am-2*da-acc)/2000,bf/2000,lm/2000,0,90,90
wpcsys,-1
race,(lz+2*rad)/2000,(lm+2*rad)/2000,rad/1000,ic*wc/2,bc/1000,ac
/1000,,,
local,14,0,(af+am+2*da+acc)/2000,bf/2000,lm/2000,0,90,90
wpcsys,-1
race,(lz+2*rad)/2000,(lm+2*rad)/2000,rad/1000,ic*wc/2,bc/1000,ac
/1000,,,
/psymb,csys,0
ALLSEL,ALL
NUMCMP,ALL
MSHAPE,1,3D
SMRTSIZE,1
VMESH,ALL
eplot
/SOLU
d,37610,mag,0
ALLSEL,ALL
```

```
magsolv,3,,,,100,1
SOLVE
/post1
CSYS,0
PATH,ag-c,2,30,100 !3001000
PPATH,1,,0.5*(af-am-0.04)*0.001,bf/2000,0,
PPATH,2,,0.5*(af-am-0.04)*0.001,bf/2000,lm/1000,
PDEF,Bd,B,X,NOAV
PCALC,INTG,Bdav,Bd,S,1/(lm*0.001),
*get,Bdm,PATH,0,MAX,Bdav,
*VFILL,Bair(j),DATA,Bdm,
PATH,ayz,2,30,100
PPATH,1,,0.5*ay*0.001,(bf)*0.001,lm/2000
PPATH,2,,0.5*ay*0.001,(0)*0.001,lm/2000
PDEF,Bayz,B,SUM,NOAV
*get,Bfe,PATH,0,MAX,Bayz,
*VFILL,Bcore(j),DATA,Bfe,
FINISH
*IF,j,LT,edd,THEN
/prep7
CSYS,0
ALLSEL,ALL
VCLEAR,ALL
ALLSEL,ALL
EDELE,ALL
ALLSEL,ALL
VDELE,ALL,,,1
wpcsys,-1
*enddo
*else
*enddo
*STATUS,Bair
*STATUS,Bcore
```